NON-SHOCK INDUCED HOT-SPOTS FORMATION IN POLYMER BONDED EXPLOSIVES

by

Akshay Vivek Dandekar

A Dissertation

Submitted to the Faculty of Purdue University

In Partial Fulfillment of the Requirements for the degree of

Doctor of Philosophy

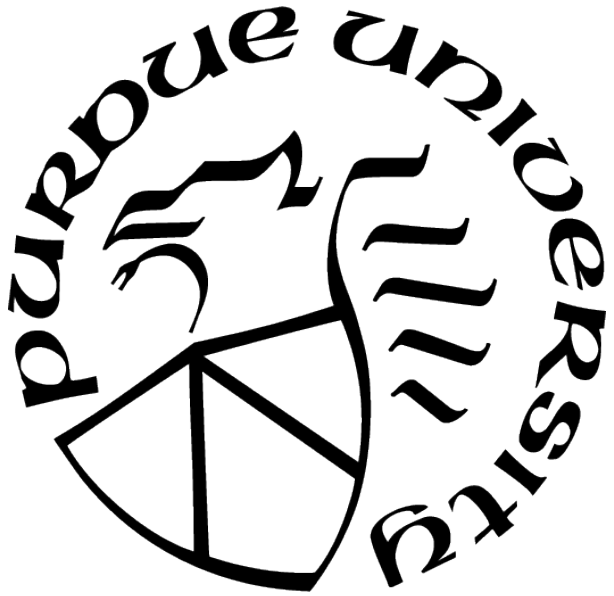

School of Mechanical Engineering

West Lafayette, Indiana

May 2021

THE PURDUE UNIVERSITY GRADUATE SCHOOL
STATEMENT OF COMMITTEE APPROVAL

Dr. Marisol Koslowski, Chair

School of Mechanical Engineering

Dr. Steven Son

School of Mechanical Engineering

Dr. Terrence Meyer

School of Mechanical Engineering

Dr. Weinong Chen

School of Aeronautics and Astronautics

Approved by:

Dr. Nicole Key

To Aai, Baba, Aaji and Aajoba

ACKNOWLEDGMENTS

I would like to thank my advisor Dr. Marisol Koslowski for her valuable guidance and support throughout my time at Purdue University. Her continuous encouragement lead me to learn a lot in mechanics and materials. I am fortunate to have her as mentor for my graduate studies.

I would like to thank my graduate advisory committee members Dr. Steven Son, Dr. Terrence Meyer and Dr. Weinong Chen. I highly appreciate their advice and insights in the projects throughout my time at Purdue University.

I am thankful to my group members Dr. Nicolo Grilli, Dr. Ahmed Hamed, Dr. Yifei Zeng, Dr. Xiaorong Cai, Camilo Duarte, Bogdan Tanasoiu and Rohan Tibrewala for their help. We share wonderful discussions and memories. I am also grateful to collaborators, fellow students, friends and roommates who helped me along the way.

I would like to thank the program manager Dr. Martin Schmidt to support this research through the Air Force Office of Scientific Research, grant no. FA9550-15-1-0102. I would like to thank the program managers Dr. Kenny Lipkowitz and Dr. Chad Stoltz to support this research through the US Department of Defense, Office of Naval Research, MURI contract number N00014-16-1-2557. I would like to thank Dr. Wen Jiang from Idaho National Laboratory for his support with MOOSE.

Finally, I would like to thank my family for their continued support and encouragement during this time.

TABLE OF CONTENTS

LIST OF TABLES

LIST OF FIGURES

LIST OF SYMBOLS

$\boldsymbol{u}$	displacement
$\boldsymbol{v}$, $\dot{\boldsymbol{u}}$	velocity
$\boldsymbol{a}$, $\ddot{\boldsymbol{u}}$	acceleration
t	time
$\boldsymbol{\epsilon}$	strain
$\boldsymbol{\sigma}$	stress
W_f	energy dissipated in fracture
G_c	surface energy
Γ	crack surface
$\gamma(c)$	crack surface density
Ω, V	volume
c	phase field variable
∇	gradient operator
l_0	characteristic length
a	strain energy density
a^+	positive part of strain energy density
a^-	negative part of strain energy density
k_r	residual stiffness
L	Lagrangian
A	strain energy
K	kinetic energy
ρ	density
η	numerical viscosity
Δ	laplacian operator
β, γ	Newmark time integration parameters
λ, μ	Lame's parameters
ϵ^v	volumetric strain
$\boldsymbol{\epsilon}^d$	deviatoric strain

:	matrix inner product operator
$\boldsymbol{I}$	identity matrix
C	specific heat
T	temperature
$\dot{q}$	volumetric heat source
$\boldsymbol{h}$	heat flux
$\boldsymbol{h}^c$	heat flux at crack surface
$\boldsymbol{n}$	unit normal vector
k	thermal conductivity
k^u	thermal conductivity of undamaged material
μ_f	friction coefficient
t_n	normal component of traction
v_s	tangential component of velocity jump across crack surface
$\boldsymbol{r}$	distance perpendicular to crack line
E	young's modulus
ν	Poisson's ratio
G_c^{i}	critical energy release rate at interface

ABBREVIATIONS

PBX	Polymer Bonded Explosive
EM	Energetic Material
HMX	1,3,5,7-tetranitro-1,3,5,7-tetrazocane
HTPB	Hydroxyl-Terminated Poly-Butadiene
EOS	Equation of State
FE	Finite Element
MD	Molecular Dynamics

ABSTRACT

Polymer bonded explosives (PBXs) consist of energetic material (EM) crystals embedded inside a polymeric binder. These are highly heterogeneous structures designed to explode under controlled conditions. However, accidental ignition of PBXs leading to deflagration, or even detonation, may take place due to non-shock stimulus such as low velocity impacts and vibration. Thus, assessing the safety of PBXs under non-shock stimulus is very important.

The ignition in PBXs depends on several microstructural features which include mechanical properties of EM particles and polymeric binder, as well as the adhesive properties of interface between EM particles and binder. It is also sensitive to initial defects in EM particles including cracks or voids. EM particle size distribution, distance between particles and their relative location are also shown to be affecting the ignition behavior of PBXs. This study focuses on PBX composition consisting of HMX as EM and Sylgard or HTPB as polymeric binder. Among several mechanisms of hot-spot formation, this study focuses on frictional heating at cracks or debonded surfaces.

Finite element simulations are performed on a domain containing a single EM particle embedded inside polymer binder under compressive and tensile loading at 10 m/s. The effect of the binder properties and the particle surface properties, on damage evolution and corresponding temperature rise due to frictional heat generation, is investigated. Two binders, Sylgard and HTPB, while two surface qualities for HMX particle, low and high, are compared. The adhesion strength of the particle-polymer interface is varied and damage evolution is qualitatively compared with experimental results to estimate interfacial energy release rate for HMX-Sylgard and HMX-HTPB interfaces. Simulations of two HMX particles inside Sylgard binder, subjected to vibration loading, are performed to analyze the effect of particle-particle distance and relative location of particles on the damage evolution and frictional heating in the particles.

The results of impact simulations show that the low surface quality HMX particle inside HTPB is likely to propagate cracks as compared to high surface quality particle. The HMX particle inside Sylgard shows crack propagation irrespective of particle surface quality. The impact simulations with the lower stiffness binder do not show a significant increase in

temperature after impact. A polymer with higher stiffness induces more particle damage under impact contributing to a larger temperature rise. Furthermore, high quality surface and higher adhesion strength induces larger stresses and increase the temperature rise. The vibration simulations show that a small particle is less likely to damage when it is shielded by a large particle irrespective of its distance, within 40-200μm, from the large particle. However, the small particle is likely to damage when it is in parallel to the large particle with respect to loading. The temperature rise in the small particle is higher than the larger particle only in case of parallel configuration. The adhesion between the particles and the polymer has a direct effect on the formation of hot-spots due to friction and through local increase of compressive stresses that may cause a surge in heat generation.

The energetic materials often show anisotropy in elastic and crystalline properties. Fracture in HMX along the preferred cleavage plane is considered. Anisotropy in the elastic constants is also incorporated in the fracture model. The dependence of pressure on temperature is considered using Mie-Gruneisen equation of state which is shown to be important for damage evolution in HMX at impact velocity of 100 m/s.

1. INTRODUCTION

Polymer bonded explosives (PBX) are synthesized by embedding energetic material crystals in a polymeric binder in order to control the sensitivity of the crystals [1]. In 1952, first ever PBX was developed by Los Alamos National Laboratory, USA which consisted of RDX crystals inside plasticized polystyrene. Since then, various energetic materials and polymers have been used to manufacture different compositions of PBXs. The energetic materials used in PBXs include RDX, HMX, HNS, PETN, TATB and CL-20 while polymers include Sylgard, HTPB, Nylon, Fluoro-polymer, Kel-F800, Estane, Nitrocellulose, Viton-A, BDNPA, Polystyrene. Typically the polymer consists of 5-10% by weight of any PBX composition while the rest is energetic material. The mechanical properties of final PBX composition can be controlled by controlling the properties of individual constituent materials which include chemical composition and mechanical properties. Thus, any change in the composition, constituent material properties and initial condition of constituent material can affect the overall explosive outcome of the composition. Thus, it is important to consider the entirity of the PBX microstructure in order to assess their final outcome and safety.

The design of polymer bonded explosives is aimed to control the initiation, mechanical loading being one of the stimulus to initiate the material. Properties of constituent materials such as binder properties, energetic material properties, crystal size distribution, crystal concentration can be varied in order to control the final explosive outcome of the composition [1]. Non-shock stimulus such as low velocity impacts and vibrations have been estimated to produce hot-spots and initiate the reaction in PBXs [2]. These can lead to accidental ignition followed by deflagration. Therefore, in order to assess the safety in the use of PBXs, it is of primary importance to understand the underlying heat generating mechanisms when loaded with non-shock stimulus and quantify the dependency of the sensitivity of the PBX on the properties such as adhesion at crystal-binder interface, quality of crystals, inter-particle distance, etc. In this work low velocity impacts and vibrations are primarily considered as non-shock stimulus.

Mechanical energy can be transformed to thermal energy by several mechanisms [2], [3]. When the thermal energy is localized, small regions of very high temperature are formed

which are called hot-spots. The mechanisms, leading to hot-spot formation, considered in literature are: (i) adiabatic compression of trapped gas spaces, (ii) void collapse, (iii) plastic deformation, (iv) heating at crack tips, (v) heating at dislocation pile-ups, (vi) friction at crack surfaces, (vii) dissipation due to crack propagation, (viii) particle/polymer debonding, and (ix) viscous heating [3], [4]. Dienes et al. [5], [6] provided a quantitative comparison among the different mechanisms that produce heat over a range of strain rates and pressures. These studies suggest that frictional heat generation at cracks may be the dominating mechanism over a wide range of loading conditions. Thus, properties of PBXs which are important for damage and crack propagation in PBXs are important to study.

Chapter 2 examines the low velocity impact loading on single HMX particle inside Sylgard and HTPB binder. It discusses the effect of mechanical properties of binder and surface quality of HMX crystal on the damage evolution. The effect of different adhesion strength of particle-polymer interface is also discussed. The chapter gives explanation of the phase field damage model used in the simulations, the results of compression & tension experiments, results of simulations and discusses the comparison between the experiment and simulation.

Chapter 3 discusses the response of PBX microstructure under vibration loading. Further investigation with two HMX crystals inside Sylgard binder under vibration is also carried. Different particle surface qualities and the effect of the inter-particle distance on the damage response of the particles are considered. Two configuration of particle location are considered. The chapter explains the model used in simulations, discusses the results of microstructure & two particle simulations and gives a comparison between experiments in literature and current simulations.

Chapter 4 explains the phase field damage model for anisotropic crack propagation and inclusion of equation of state for calculation of pressure. It gives some preliminary results of damage evolution in HMX under impact at 100 m/s. The comparison of results with and without equation of state explains the importance of inclusion of equation of state for high velocity impacts. It also discusses the heat generation due to molecular jetting inside cracks in HMX under shock impact and possibility of incorporating the same in finite element simulations.

2. SINGLE EM PARTICLE PBX UNDER LOW VELOCITY COMPRESSION AND TENSION

Note: A version of this chapter has been published in Computational Materials Science with title 'The effect of the particle surface and binder properties on the response of polymer bonded explosives at low impact velocities' [7]. The experimental results in the article are by courtesy of co-authors Dr. Zane Roberts, Shane Paulson, Dr. Weinong Chen and Dr. Steven Son. DOI: https://doi.org/10.1016/j.commatsci.2019.04.033

2.1 Introduction

Polymer bonded explosives (PBXs) contain energetic particles in a polymeric binder. These composites are designed to detonate under a controlled shock stimulus by optimizing the binder properties, crystal size distribution and concentration [1]. However, when the explosives are subjected to non-shock initiation stimulus, such as low impact loading, high temperature, or vibrations, accidental ignition followed by deflagration may occur [2].

Mechanical energy can be transformed to thermal energy by several mechanisms including, friction, crack propagation, void collapse and plastic dissipation [2], [3], [5], [8]. Dienes et al. [5], [6] provide a quantitative comparison among the different mechanisms that produce heat over a range of strain rates and pressures. These studies suggest that frictional heat generation at cracks may be the dominating mechanism over a wide range of loading conditions.

Due to the importance of fracture as a heat source in PBXs there is extensive numerical and experimental work done. For example, quasi-static compression experiments on PBX-9501 have shown that failure starts at the particle/binder interface, especially near the larger HMX (1,3,5,7-tetranitro-1,3,5,7-tetrazocane) particles [9], [10]. On the other hand, dynamic compression experiments on HMX particles inside HTPB (hydroxyl-terminated polybutadiene) binder at impact velocities around 10 m/s have shown crack propagation inside the crystals [11], [12]. Similar compression tests with Sylgard (polypolydimethylsiloxane) binder have shown crack propagation inside of particles and debonding at the crystal-polymer interface [12].

However, most numerical simulations focus on failure at the particle/binder interface. For example, Arora et al. [13] studied the effect of particle density and geometry on the

failure of PBXs at strain rates below 10^{-1} s^{-1}. Their simulations considered only failure at particle/binder interfaces. The energy release rate used in their model is obtained from atomistic simulations of TATB by Gee et al. [14] and it is G_c=0.27 J/m^2. Tan et al. [15] developed a model to find the cohesive zone parameters of the particle/binder interface of PBX-9501. They found a cohesive strength of 1.66 MPa and an energy release rate G_c=89 J/m^2 for the interface between HMX and the polymeric binder.

Recent experiments and simulations by Walters et al. [16] were performed on HMX-HTPB systems to extract cohesive zone damage parameters using finite elements. The fracture energy, G_c, for the HMX-HTPB interface was estimated to be in the range 3 to 10 J/m^2 for a loading rate of 3.33 μm/s. This value is in the same range as experimental measurements of Sylgard-quartz interfaces [17] that rendered G_c=1-10 J/m^2 and for the interface between Sylgard and glass [18]–[20], G_c=17 J/m^2.

At larger impact velocities fracture and heat transfer simulations have been coupled to calculate the temperature field with heat sources due to friction at crack surfaces. Barua et al. [21] studied the temperature rise in HMX-Estane for impact velocities between 50 - 300 m/s using cohesive zone elements at the particle/polymer interfaces. In the early stage of deformation the temperature rise was dominated by viscoelastic dissipation in the binder, while in the later stage of deformation the friction at particle-binder interfaces dominated the temperature rise. Grilli et al. [22] considered single HMX particles inside Sylgard binder with impact velocity between 100 - 400 m/s using a phase field damage model. The largest temperature increase was found at cracks that intersected the particle/binder interface.

Unfortunately, the experimental data available to inform the numerical models at the particle level remains limited. Therefore, more detailed experiments and simulations are needed to calibrate and validate the thermo-mechanical response of PBX composites at the mesoscale level to understand the relative importance of each of the heat sources proposed in different models. Here, we use a combination of experiments and simulations to study fracture and heating due to friction at crack surfaces.

This work focuses on the response of HMX particles inside HTPB and Sylgard 184 binders upon compressive and tensile loading using finite element simulations and experiments. Different particle surface qualities are studied. The simulations include fracture and

crack propagation and predict the temperature rise due to frictional heating at cracks and debonded surfaces. The effects of the mechanical properties of the binder as well as the adhesive properties of the particle/binder interface are compared.

The paper is organized as follows. In Section 2.2, the mechanical, fracture and thermal models used in the simulations are described. Section 2.3 contains the experimental methods and findings. In Section 2.4, the details of the geometry used in the simulations are presented with reports of the results for compression and tension including fracture and temperature fields. Section 2.5 summarizes the findings and offers conclusions and further prospects.

2.2 Methods

2.2.1 Phase field damage model

The phase field damage model (PFDM) is a numerical approach to describe fracture evolution [23]. The model is based on Griffith's theory of fracture [24] in which the energy dissipated by fracture is:

$$W_f = \int_\Gamma G_c d\Gamma \tag{2.1}$$

where G_c is the surface energy for brittle materials and the critical energy release rate for ductile materials. Micro-indentation experiments show that HMX behaves as a brittle material at low strain rates [25], [26] while at higher strain rates, atomistic simulations show plastic activity [27]–[29]. In the PFDM the crack surface, Γ, is expressed in terms of a diffuse delta function $\gamma(c)$ as [30]–[34]:

$$\int_\Gamma d\Gamma = \int_V \gamma\left(c\right) dV \tag{2.2}$$

with

$$\gamma\left(c\right) = \frac{1}{2l_0}\left(c^2 + l_0^2 \left|\nabla c\right|^2\right) \tag{2.3}$$

where the phase field variable, $c(\boldsymbol{x})$, ranges from 0 to 1, with $c = 0$ being undamaged material while $c = 1$ corresponds to fully damaged material, and l_0 is a characteristic length that determines the width of the transition from damaged to undamaged material [20], [31].

To introduce the loss of stiffness in the damaged regions, the strain energy is divided into two terms:

$$a\left(\boldsymbol{\epsilon}, c\right) = \left[(1-c)^2 + k_r\right] a^+\left(\boldsymbol{\epsilon}\right) + a^-\left(\boldsymbol{\epsilon}\right) \tag{2.4}$$

where k_r is a residual stiffness included for numerical stability [31]. The first term in the strain energy density is the part that degrades with damage and the second term is not affected by damage. Different representations of Equation 2.4 have been presented to take into account the damage response of different materials [34].

To make the model thermodynamically consistent, the rate of work dissipated needs to be positive. Therefore, the next condition needs to be satisfied [30], [32]:

$$\dot{W}_f = \int_\Omega G_c \dot{\gamma}(c, \boldsymbol{\nabla} c) dV = \int_\Omega G_c \delta_c \gamma \cdot \dot{c}\, dV \geq 0\ . \tag{2.5}$$

Equation 2.5 reduces to the conditions: $\delta_c \gamma \geq 0$ and $\dot{c} \geq 0$, where $\delta_c \gamma = \partial_c \gamma - \boldsymbol{\nabla} \cdot \partial_{\boldsymbol{\nabla} c} \gamma$ is the functional derivative of $\gamma(c, \boldsymbol{\nabla} c)$ with respect to c.

The evolution of deformation and damage are coupled using the Lagrangian,

$$L\left(\dot{\boldsymbol{u}}, \boldsymbol{\epsilon}, c\right) = K\left(\dot{\boldsymbol{u}}\right) - A\left(\boldsymbol{\epsilon}, c\right) - W_f\left(c\right) \tag{2.6}$$

where $K\left(\dot{\boldsymbol{u}}\right)$ is the kinetic energy given by

$$K\left(\dot{\boldsymbol{u}}\right) = \int_V \frac{1}{2} \rho \left|\dot{\boldsymbol{u}}\right|^2 dV \tag{2.7}$$

and $A\left(\boldsymbol{\epsilon}, c\right)$ is strain energy given by

$$A\left(\boldsymbol{\epsilon}, c\right) = \int_V a\left(\boldsymbol{\epsilon}, c\right) dV \tag{2.8}$$

Here, $\dot{\boldsymbol{u}}$ is the velocity vector and ρ is the density. The Euler-Lagrange equations result in:

$$\nabla \cdot \boldsymbol{\sigma} = \rho \frac{\partial^2 \boldsymbol{u}}{\partial t^2} \tag{2.9}$$

where ρ is the mass density and the stress tensor is obtained as:

$$\boldsymbol{\sigma} = \frac{\partial a\left(\boldsymbol{\epsilon}, c\right)}{\partial \boldsymbol{\epsilon}} = \left[(1-c)^2 + k_r\right] \frac{\partial a^+\left(\boldsymbol{\epsilon}\right)}{\partial \boldsymbol{\epsilon}} + \frac{\partial a^-\left(\boldsymbol{\epsilon}\right)}{\partial \boldsymbol{\epsilon}} \tag{2.10}$$

The evolution of the damage field is obtained from a time dependent Ginzburg-Landau equation, that results in [33]:

$$\dot{c} = \frac{1}{\eta}\left\langle l_0 \Delta c + 2(1-c)\frac{a^+(\boldsymbol{\epsilon})}{G_c} - \frac{c}{l_0}\right\rangle \ , \tag{2.11}$$

where η plays a role of a viscosity that controls the convergence by adding dissipation. The value of η was chosen to reach a rate independent behavior [33], [35]. The operator $\langle x \rangle$ is defined as,

$$\langle x \rangle = \begin{cases} x & \text{if } x \geq 0 \\ 0 & \text{if } x < 0 \end{cases} \tag{2.12}$$

Equations 2.9, 2.10, and 2.11 are implemented and solved numerically in the finite element software MOOSE (Multiphysics Object Oriented Simulation Environment)[33], [36]. Given that the stresses observed in the simulations are below the yield stress of HMX, 75 MPa, [37], [38], plastic deformation is not considered.

The numerical parameters used in the simulation are chosen as $l_0 = 40$ μm, $\eta = 0.1$ s/m, and $k_r = 1 \cdot 10^{-6}$ [22]. The dynamical response is solved using a Newmark time integration scheme:

$$\ddot{\boldsymbol{u}}^{n+1} = \frac{\boldsymbol{u}^{n+1} - \boldsymbol{u}^n}{\beta \Delta t^2} - \frac{\dot{\boldsymbol{u}}^n}{\beta \Delta t} + \frac{\beta - 0.5}{\beta}\ddot{\boldsymbol{u}}^n \tag{2.13}$$

$$\dot{\boldsymbol{u}}^{n+1} = \dot{\boldsymbol{u}}^n + (1-\gamma)\,\Delta t \ddot{\boldsymbol{u}}^n + \gamma \Delta t \ddot{\boldsymbol{u}}^{n+1} \tag{2.14}$$

where β and γ are Newmark time integration parameters. The values used in the present analysis are, $\beta = 0.3025$, $\gamma = 0.6$ and $\Delta t = 1$ ns.

Damage models

The strain energy density in Equation 2.4 has different forms for the HMX particle and the polymer. For the particles the following division of the strain energy density is used [20], [22]:

$$a^{+}(\boldsymbol{\epsilon}) = \frac{\lambda}{2}\langle \epsilon^{v} \rangle^{2} + \mu\left(\langle \epsilon_1 \rangle^{2} + \langle \epsilon_2 \rangle^{2} + \langle \epsilon_3 \rangle^{2}\right) \tag{2.15}$$

$$a^{-}(\boldsymbol{\epsilon}) = \frac{\lambda}{2}\left(\epsilon^{v} - \langle \epsilon^{v} \rangle\right)^{2} + \mu\left(\left(\epsilon_1 - \langle \epsilon_1 \rangle\right)^{2} + \left(\epsilon_2 - \langle \epsilon_2 \rangle\right)^{2} + \left(\epsilon_3 - \langle \epsilon_3 \rangle\right)^{2}\right) \tag{2.16}$$

where the volumetric strain is $\epsilon^{v} = \epsilon_1 + \epsilon_2 + \epsilon_3$ and ϵ_1, ϵ_2, and ϵ_3 are the principal strains, and $\lambda = \dfrac{E\nu}{(1+\nu)(1-2\nu)}$ and $\mu = \dfrac{E}{2(1+\nu)}$ are the Lame's parameters.

Experimental and numerical results show that polymers damage under shear and volumetric tensile loads [34]. However, due to the low stresses in the matrix no damage is observed in the polymers in the experiments, as described in Section 2.3. Therefore, no damage in the matrix will be considered in the simulations.

Debonding between the particle and the matrix is observed in the experiments. The experiments of Gent et al. [18] suggest that debonding between Sylgard and rigid spherical inclusions occurs due to tensile stress. 3D simulations using our model confirm that including only the positive volumetric stress reproduce the debonding patterns observed in experiments using Sylgard and glass spheres [19]. Thus, the components of strain energy density for the damage model in the interface are approximated as:

$$a^{+}(\boldsymbol{\epsilon}) = \frac{1}{2}\left(\lambda + \frac{2\mu}{3}\right)\langle \epsilon^{v} \rangle^{2} \tag{2.17}$$

$$a^{-}(\boldsymbol{\epsilon}) = \frac{1}{2}\left(\lambda + \frac{2\mu}{3}\right)\left(\epsilon^{v} - \langle \epsilon^{v} \rangle\right)^{2} + \mu\boldsymbol{\epsilon}^{d} : \boldsymbol{\epsilon}^{d} \tag{2.18}$$

where the operator : denotes the double contraction product of two second order tensors and $\boldsymbol{\epsilon}^{d}$ is the deviatoric strain tensor given by,

$$\boldsymbol{\epsilon}^{d} = \boldsymbol{\epsilon} - \frac{\epsilon^{v}}{3}\boldsymbol{I} \tag{2.19}$$

where $\boldsymbol{I}$ is the identity tensor.

2.2.2 Heat generation model

The integral form of the heat equation is given by:

$$\int_{\Omega} \rho C \frac{\partial T}{\partial t} dV = \int_{\Omega} \dot{q} dV - \int_{\partial\Omega} \boldsymbol{h} \cdot \mathbf{n} \; dA \; , \tag{2.20}$$

where C denotes the specific heat, T is the temperature, q is a heat source density, $\boldsymbol{h} = -k\boldsymbol{\nabla} T$ is the heat flux per unit area across the surface $\partial\Omega$ with normal $\boldsymbol{n}$, and k is the thermal conductivity.

The only heat source considered here is friction at crack surfaces. Dissipation due to crack propagation is one order of magnitude smaller than the heat generated due to friction and therefore, is not considered here [39]. The surface term in Equation 2.20 is divided in two contributions representing the domain boundary and the cracks [22], [39]:

$$\int_{\partial\Omega} \boldsymbol{h} \cdot \boldsymbol{n} \; dA = \int_{\partial\Omega - \Gamma} \boldsymbol{h} \cdot \boldsymbol{n} \; dA + \int_{\Gamma} \boldsymbol{h}^c \cdot \boldsymbol{n} \; dA \tag{2.21}$$

where the heat flux at the crack surfaces, $h^c = \boldsymbol{h}^c \cdot \boldsymbol{n}$ is given by [5], [40]:

$$h^c = -\mu_f \left\langle -t_n \right\rangle v_s \tag{2.22}$$

where μ_f is the friction coefficient, t_n is the normal component of the traction at the crack surface, and v_s is the tangential component of the velocity jump across the crack surfaces. The symbol $\langle\rangle$ ensures that heat due to friction operates only when the traction is negative. The velocity jump across the crack surface can be approximated from the velocity gradient as,

$$\boldsymbol{v}^+ - \boldsymbol{v}^- = (\nabla \boldsymbol{v} \cdot \hat{\boldsymbol{n}}) \, l_0 \tag{2.23}$$

where the distance between crack surfaces is approximated by the characteristic length, l_0, and the normal to the crack surface is calculated from the gradient of the phase field variable as [39]:

$$\hat{\boldsymbol{n}} = -\frac{\nabla c}{|\nabla c|} \tag{2.24}$$

2.3 Experimental results

The samples were approximately 2 mm x 2 mm x 1 mm with a 500-800 μm size HMX crystal embedded. Production-grade B class 3 β-HMX particles from BAE Systems with rough, cracked surface and porous interior, without any modification, were encapsulated in the polymer binders. Degassing steps under vacuum were followed prior to curing in order to draw air bubbles away from crystal surfaces and promote good binder adhesion. The sample preparation techniques and the experimental procedures for X-ray phase contrast imaging (PCI) under dynamic compression performed at the Advanced Photon Source, Argonne National Laboratory are described in detail in Parab *et. al* [11].

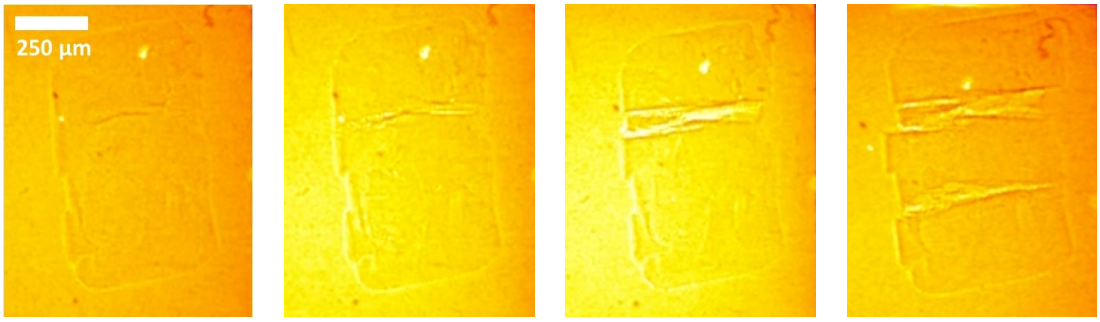

(a) t = 0 μs (b) t = 1 μs (c) t = 3 μs (d) t = 21 μs

Figure 2.1. Experiment showing the fracture evolution in an HMX-HTPB system during compressive loading from the left-hand side with a hard stop on the right of the image. Note the lack of crystal-binder delamination despite significant crystal damage and strain.

Figure 2.1 shows a series of high-speed X-ray phase contrast images that reveal the behavior of a single HMX crystal inside HTPB binder loaded with a compressive velocity of 10 m/s using a modified Split Hopkinson (Kolsky) bar. The sample was confined by two acrylic windows and a hard stop on the right side of the image. As the sample was compressed

from the left, two horizontal cracks developed and propagated across the crystal. The particle broke in approximately 21 μs after the initiation of the crack. Other single crystal HMX-HTPB samples were loaded at the same velocity and a different behavior was observed. For example, the particle translated along the impact direction or rotated with no evidence of interfacial debonding or cracking. Figure 2.2 shows this behavior.

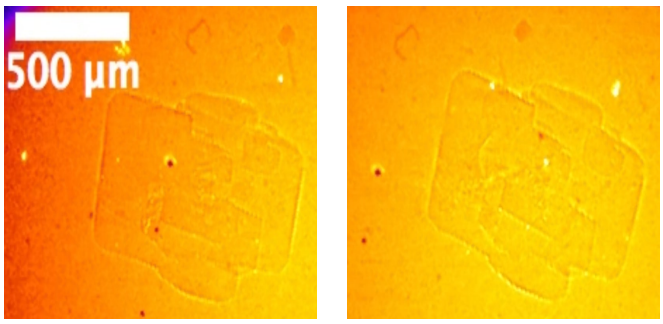

(a) t = 0 μs (b) t = 50 μs

Figure 2.2. Experiment showing no damage evolution in a HMX-HTPB system for compressive loading.

Similar experiments performed using Sylgard 184 (polydimethylsiloxane) as a binder mixed in a 10:1 base to curative ratio and cured at 60^{o}C for over 12 hours after degassing are shown in Figure 2.3. Multiple cracks nucleated and damage spread across the whole crystal. The entire particle shattered within 6 μs after the initiation of very first crack in the particle and debonding was observed in Figure 2.3 (d).

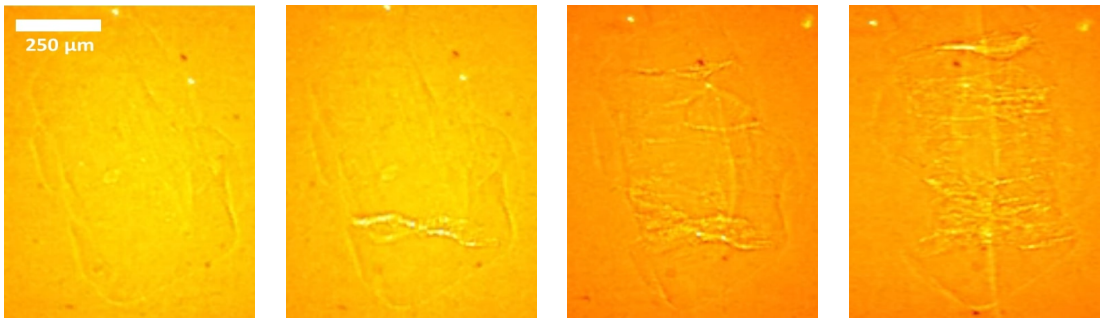

(a) t = 0 μs (b) t = 1 μs (c) t = 3 μs (d) t = 5 μs

Figure 2.3. Experiment showing fracture evolution of a HMX-Sylgard system for compressive loading.

Figure 2.4 shows the behavior of a HMX-HTPB sample loaded with tensile velocity of 10 m/s using a Kolsky tension bar. Despite having initial defects, no crack propagation is observed. Conversely, tensile experiments with Sylgard as a binder showed either debonding at the HMX-Sylgard interface or fracture of the the particle.

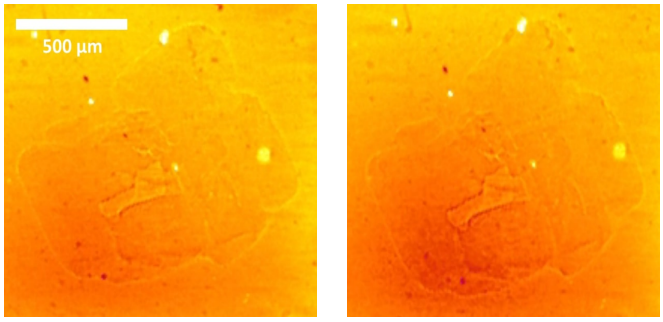

(a) t = 0 μs (b) t = 100 μs

Figure 2.4. Experiment showing no damage evolution in a HMX-HTPB system for tensile loading.

Figure 2.5 shows the behavior of a single HMX crystal inside the Sylgard binder where debonding was observed. Figure 2.6 shows a vertical crack developing inside the particle for the HMX-Sylgard system under the same loading conditions.

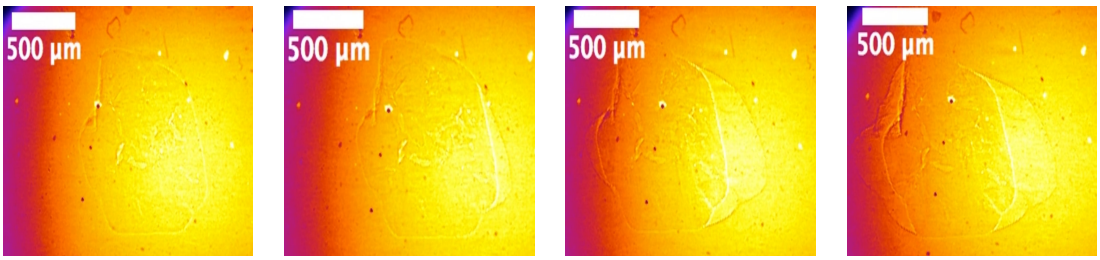

(a) t = 0 μs (b) t = 50 μs (c) t = 60 μs (d) t = 80 μs

Figure 2.5. Experiment showing debonding for a HMX-Sylgard system for tensile loading.

2.4 Simulation results

Finite element simulations are performed using 2D domains with plane strain conditions under tensile and compressive loads. The domains and boundary conditions are selected to duplicate the specimens in Figures 2.1 and 2.5.

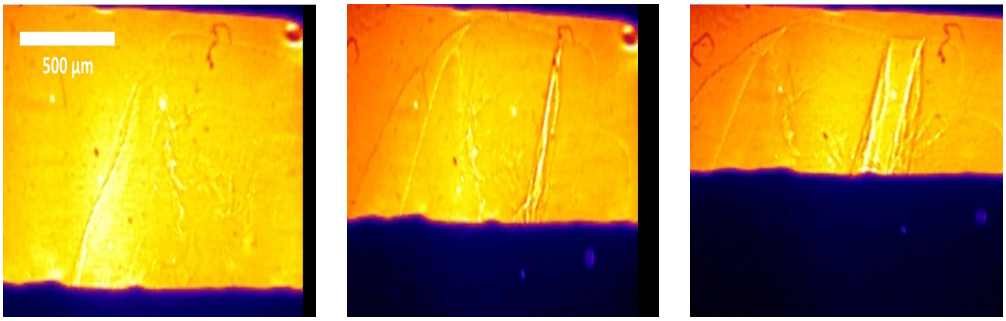

(a) t = 0 μs (b) t = 8 μs (c) t = 10 μs

Figure 2.6. Experiment showing crack development in a HMX-Sylgard system for tensile loading. The black boundary at the bottom of image is the closing shutter of the camera. Note that binder delamination occurs in tandem with crystal cracking in this case.

2.4.1 Geometry and material parameters

The domains used in the compression and tension simulations are shown in Figures 2.7 and 2.8. The particles contain elements with an average size of 10 μm, and increases from 10 μm to 20 μm towards the edge of domains. The boundary conditions are assigned to reproduce the experimental conditions with an applied velocity v_0=10 m/s. The displacement in the right boundary is fixed in the horizontal direction and in the bottom boundary is fixed in the vertical direction. The total number of elements is over 31,000 in Figure 2.7 and 45,000 in Figure 2.8.

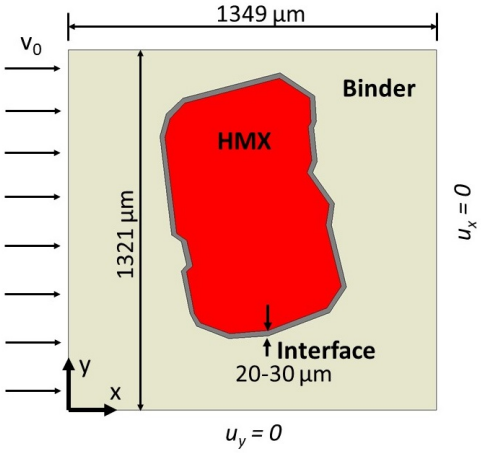

Figure 2.7. Domain used in compressive loading simulations

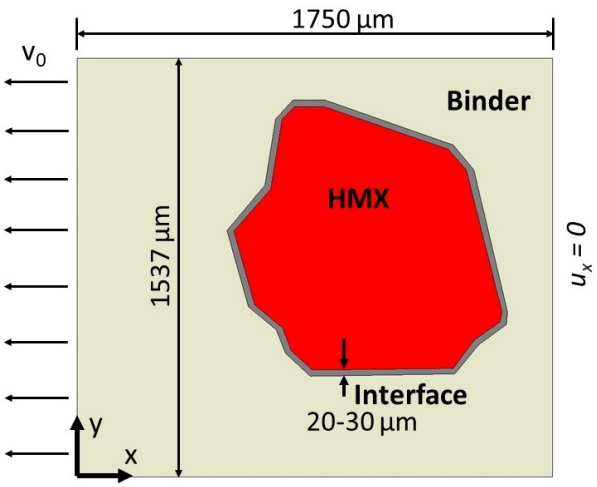

Figure 2.8. Domain used in tensile loading simulations

The material properties used in the simulations are given in Table 2.1. The surface energy of HMX reported in experiments is 0.06 J/m^2 [25]. To account for the inelastic effects at the crack tip, a higher value is chosen following [20], [22], [39]. Studies on amorphous polymers have shown that the fracture energy of polymers is in the range of 200-400 J/m^2 [34], [41], [42]. With a fracture energy in this range and the low stresses obtained in the simulations, no damage will be observed in the the polymer in agreement with the experiments.

To study the effect of the adhesion between the particle and the polymer, an interface region around the particle with thickness 20-30 μm is defined, see Figures 2.7 and 2.8. This interface has the mechanical properties of the binder while the fracture energy of the interface, G_c^{i}, is reduced. The range of the fracture energy of the interface is 10 J/m^2 to 90 J/m^2 in different simulations following previous results [15], [16], [20], see Table 2.1.

Table 2.1. Material properties and numerical parameters used in the simulations [43]–[52]

Property	HMX	Sylgard	HTPB
E [GPa]	15	0.15	0.005
ν	0.35	0.48	0.49
ρ [kg/m^3]	1903	1030	900
G_c^{i} [J/m^2]	2	10-90	10-90
k^u [W/m·K]	0.31	0.18	0.22
C [J/kg·K]	1200	1100	2500

The thermal conductivity of the material is reduced in the damaged regions [35], [39] following:

$$k\left(c\right) = \left(1 - c\right)^2 k^u \tag{2.25}$$

where k^u is the conductivity of the undamaged material reported in Table 2.1.

2.4.2 Particle surface quality and adhesive properties

Different initial crack distributions are selected to study the effect of the surface quality of the particles. The initial cracks are defined using the steady state solution of the 1D damage field which is an exponential function [22]:

$$c\left(\boldsymbol{r}, t = 0\right) = c_{max} \mathrm{e}^{-\frac{|\boldsymbol{r}|}{l_0}} \tag{2.26}$$

where $\boldsymbol{r}$ is the distance perpendicular to crack line. The values of c_{max} are chosen from a uniform distribution in the range $(0.8, 1)$. The initial crack lengths and crack orientation angles follow a Gaussian distribution with mean 100 μm and a standard deviation 35 μm and mean 0° with respect to the horizontal direction and a standard deviation of 45°. The initial crack density is 8.6%.

Figure 2.9 shows the initial crack distributions used in the compressive and tensile simulations. The black line is the boundary of the particle and the cracks are shown in white. Figures 2.9 (a) and (c) do not contain initial cracks close to the particle/binder interface, this configuration will be referred as high quality surface. In contrast, in Figures 2.9 (b) and (d) some of the initial cracks intersect the interface, therefore, this configuration is used to represent a particle with poor quality surface.

2.4.3 Compressive loading

Compressive simulations with an impact velocity of 10 m/s are performed in the domain shown in Figures 2.9 (a) and (b) with HTPB and Sylgard binders. The effects of the initial crack distribution to account for particle surface quality and the surface fracture energy are studied and compared with the experimental results.

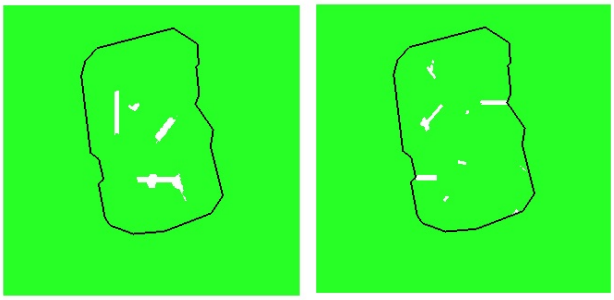

(a) High quality surface.(b) Poor quality surface.

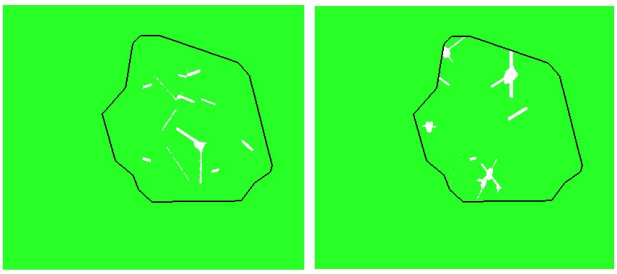

(c) High quality surface.(d) Poor quality surface.

Figure 2.9. Initial crack distributions used in the compressive (a-b) and tensile (c-d) simulations.

HTPB binder

Figure 2.10 shows the time evolution of the damage and the volumetric stress for G_c^{i}= 30 J/m^2. White regions correspond to a damage field $c > 0.9$ and the volumetric stress is shown in the background, stress concentrations at the crack tips are visible in Figures 2.10 (e) and (f). For the high quality surface particle, Figure 2.10 (a)-(c) no debonding or crack growth is observed. In the poor quality surface system, Figures 2.10 (d)-(f), two horizontal cracks that initially intersect the polymer/particle interface propagate through the particle. The time scales and crack patterns in Figures 2.10 (d)-(f) are similar to the ones observed in the experiment shown in Figure 2.1.

Figure 2.11 shows the results for the same geometry, materials, and loading conditions but with an interface fracture energy, G_c^{i}= 10 J/m^2. At $t = 15\mu s$ debonding is observed in the poor quality surface particle. For $G_c^{\mathrm{i}} > 10$ J/m^2 in high quality surface particles, no debonding or crack propagation is predicted with our model.

For low quality surface particles the damage evolution depends on G_c^{i}. For $G_c^{\mathrm{i}} = 10$ J/m^2, debonding is predominant, whereas for $G_c^{\mathrm{i}} \geq 30$ J/m^2, crack propagation inside the particle is always observed. A qualitative comparison with the experiment shown in Figure 2.1 suggests that in the experiment the value of the fracture energy of the HTPB-HMX interface should be greater than 30 J/m^2.

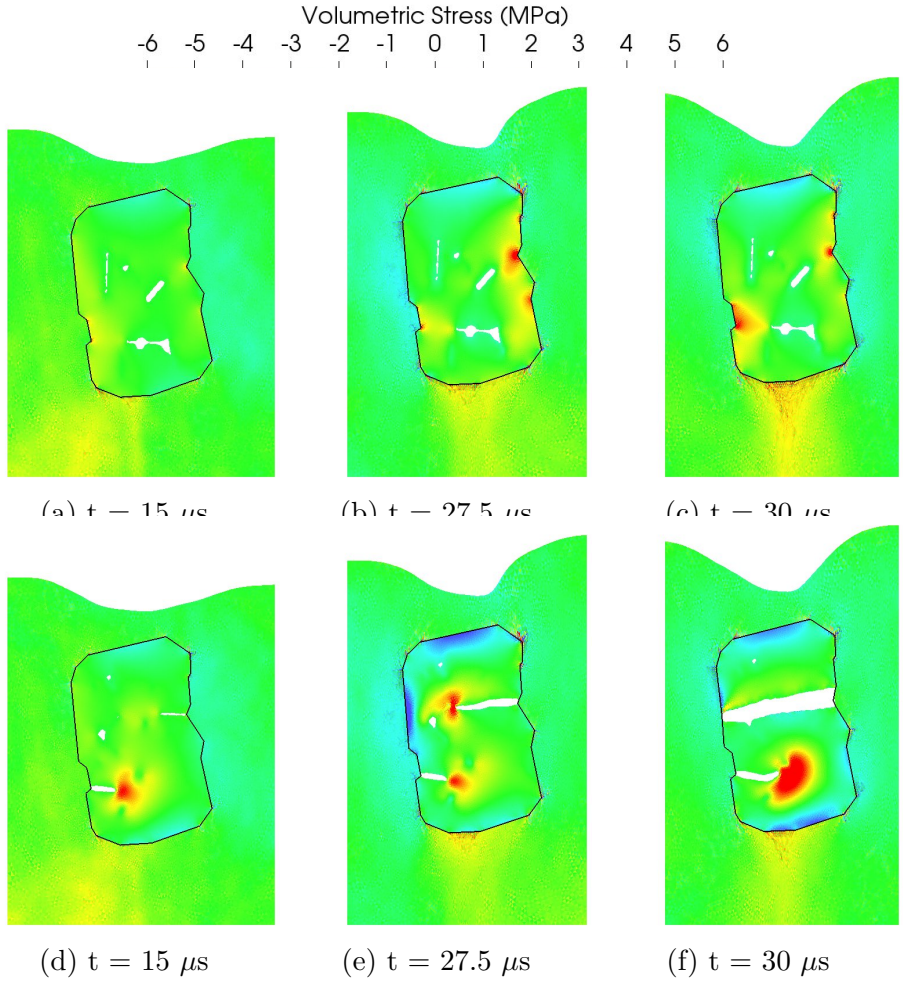

(a) t = 15 μs (b) t = 27.5 μs (c) t = 30 μs

(d) t = 15 μs (e) t = 27.5 μs (f) t = 30 μs

Figure 2.10. Volumetric stress and damage evolution for the compressive loading condition in a HTPB-HMX system with G_c^{i} =30 J/m^2, (a-c) high quality surface (d-f) poor quality surface.

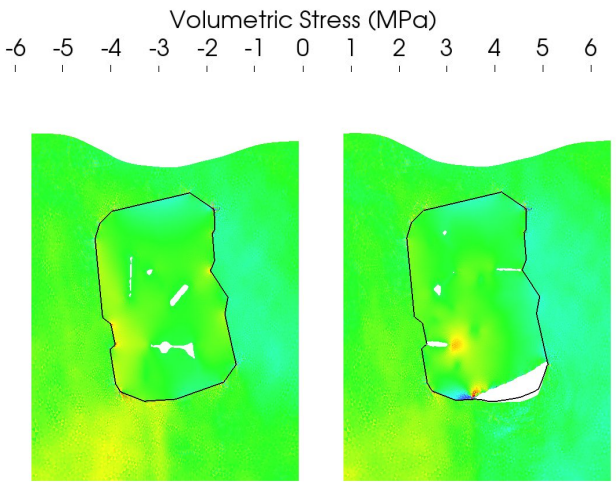

(a) high quality surface (b) poor quality surface

Figure 2.11. Volumetric stress and damage at t = 15 μs for compressive loading in the HTPB-HMX system with G_c^{i} =10 J/m^2, (a) high quality surface (e) poor quality surface.

Sylgard binder

Figure 2.12 shows the time evolution of damage and the volumetric stress for the high and poor quality surface particles in a Sylgard binder with G_c^{i}= 10 J/m^2. The higher stiffness of Sylgard, see Table 2.1, renders higher strain energy for the same applied deformation, thus, more damage is observed in the particle in agreement with the experimental results in Figure 2.3. The time scales are also in good agreement with experimental results shown in Figure 2.3. The path of the cracks is affected by pre-existing cracks in the particle as well as sharp corners at interfaces due to high stress concentrations. Several features of crack propagation are observed inside the particle, such as stress concentrations at the crack tips in Figure 2.12 (d) and crack branching in Figure 2.12 (b). The poor quality surface particle, Figures 2.12 (d)-(f), exhibit debonding on the bottom interface as observed in experiments, see Figure 2.3 (d).

In the simulations where G_c^{i} is increased up to 90 J/m^2, the crack patterns and the stress fields are equivalent to the ones in Figure 2.12. Clearly, the damage pattern and its evolution is dominated by the surface quality, i. e., the presence of cracks intersecting the interface.

Also, the higher stiffness of Sylgard renders higher stresses in the composition while creating more damage.

The higher stiffness of Sylgard is found to be critical for fracture and frictional heating. However, the same stiffness can produce a PBX that is very rigid and will maintain it's shape under stress. This also helps during machining or when stored over longer times. Similarly, while manufacturing the PBX, the curing of Sylgard can be completed at a lower temperatures as compared to HTPB and, thus, producing lower thermal stresses in the final product when it is brought to storage temperature [53].

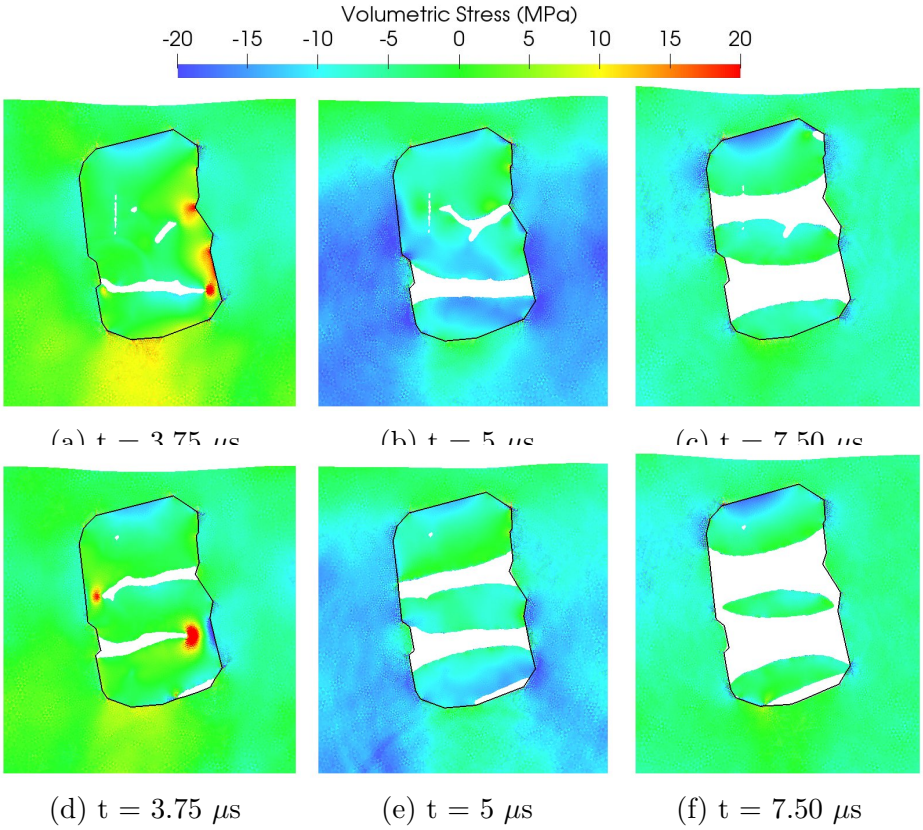

(a) t = 3.75 μs (b) t = 5 μs (c) t = 7.50 μs

(d) t = 3.75 μs (e) t = 5 μs (f) t = 7.50 μs

Figure 2.12. Volumetric stress and damage evolution for the compressive loading condition with a Sylgard-HMX system and G_c^{i} =10 J/m^2, (a-c) high quality surface (d-f) poor quality surface.

Temperature evolution

The temperature field is obtained with the model described in Section 2.2.2 with friction as the only heat source. The temperature change in HTPB-HMX system is negligible. The temperature field for the Sylgard-HMX system at t= 7.5 μs is shown in Figure 2.13. The temperature increase in the cracks and in the surface of the particles can be observed. The temperature and damage fields are similar for all the values of G_c^{i} in the range 10 J/m^2 to 90 J/m^2 simulated in this work.

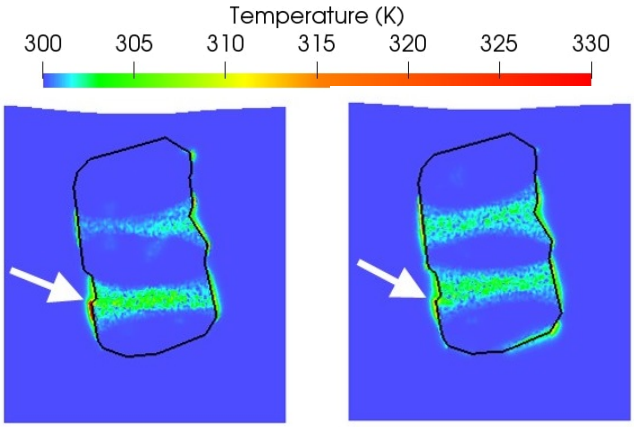

(a) High quality surface (b) Poor quality surface

Figure 2.13. Temperature field at t=7.5μs for compressive loading for HMX-Sylgard system, G_c^{i}=30 J/m^2.

Figure 2.14 shows the evolution of the average temperature calculated in a region of radius $R = 8\mu m$ where the maximum temperature is reached during the compressive loading simulation. In the HTBP-HMX systems the maximum temperature increase is less than 2 K. In the Sylgard-HMX systems, the average increase reaches 20 K. The temperature rises earlier in the poor quality surface particle. However, the stresses are larger in the high quality surface particle increasing the frictional heat rate.

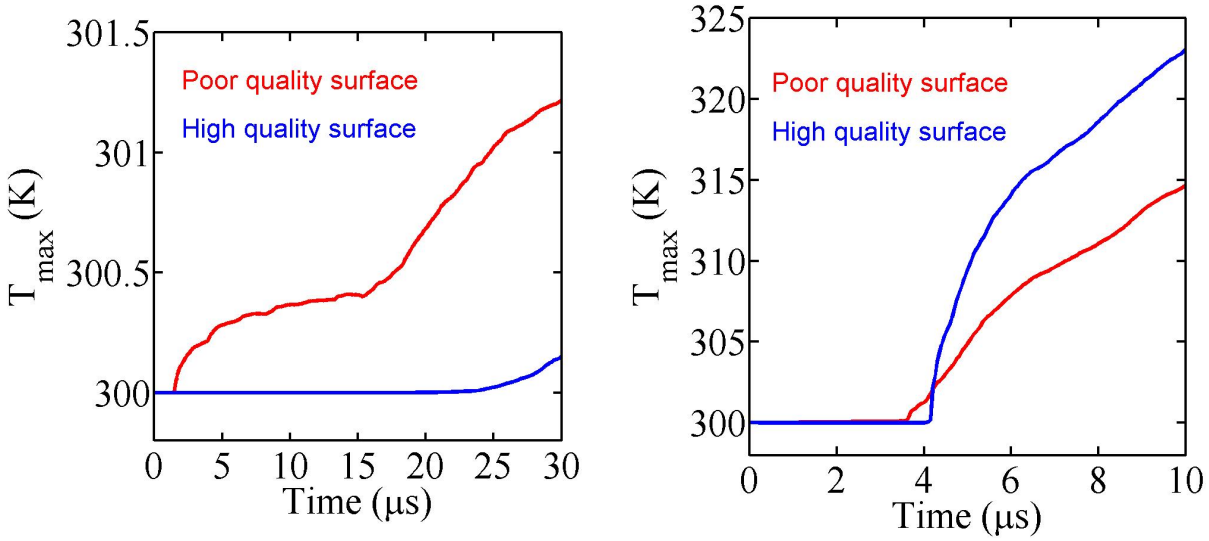

(a) HTPB binder

(b) Sylgard binder

Figure 2.14. Maximum temperature in the domain for compressive loading and $G_c^{\mathrm{i}} \geq$30 J/m^2.

2.4.4 Tensile loading

Finite element simulations with a tensile velocity of 10 m/s are performed using the domain and boundary conditions shown in Figure 2.8 with HTPB and Sylgard binders, and high and poor quality surface particles shown in Figures 2.9 (c) and (d).

HTPB binder

Figure 2.15 shows the time evolution of the damage and the volumetric stress for the high and poor quality surface particles with G_c^{i}= 30 J/m^2 in a HTPB binder. No debonding is observed in the high quality surface particle, Figures 2.15 (a)-(b). Debonding in the poor quality surface particle, Figures 2.15 (c)-(d) starts at 20 μs. When the surface energy of the particle/binder interface is reduced to G_c^{i}= 10 J/m^2 debonding is observed also for the high quality surface particle, see Figure 2.16 at time $t = 30\mu s$. The results in Figures 2.15 (a) and (b) are similar to the experiments in Figure 2.4, this suggest that $G_c \geq$30 J/m^2 in the experiments.

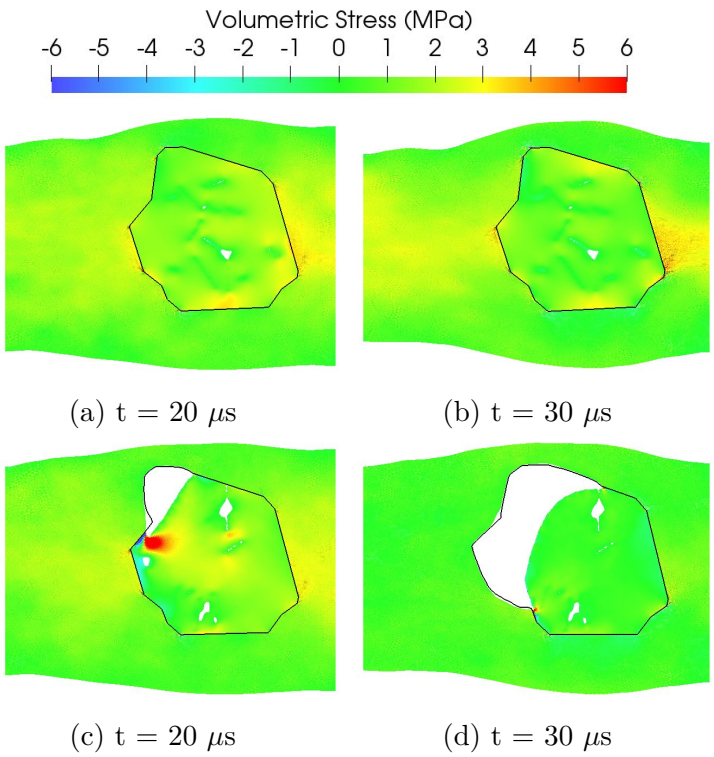

(a) t = 20 μs (b) t = 30 μs

(c) t = 20 μs (d) t = 30 μs

Figure 2.15. Volumetric stress and damage evolution for the tensile loading condition in a HTPB-HMX system and G_c^{i} =30 J/m^2, (a-c) high quality surface, and (d-f) poor quality surface.

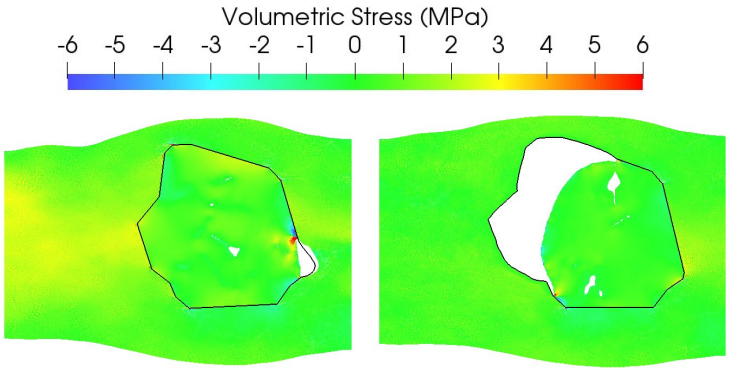

(a) t = 30 μs (b) t = 30 μs

Figure 2.16. Volumetric stress and damage field for the tensile loading condition in a HTPB-HMX system at t=30 μs with G_c^{i}=10 J/m^2, (a) high quality surface, and (b) poor quality surface.

Sylgard binder

Figure 2.17 shows the time evolution of damage for poor and high quality surface particles in a Sylgard binder with G_c^{i}= 10 J/m^2. Similarly to compressive loading in the HMX-Sylgard

system, simulations with G_c^{i} >10 J/m^2 render the same damage field and are is not shown here. However, the particle surface quality affects the results with debonding observed only when the particle surface quality is poor, Figures 2.17 (c) and (d). The experiment in Figure 2.5 shows only debonding, this suggests that G_c^{i} should be lower than 10 J/m^2 in this experiment. On the other hand, cracks developing inside the particle in Figure 2.17 agree with the experiment in Figure 2.6.

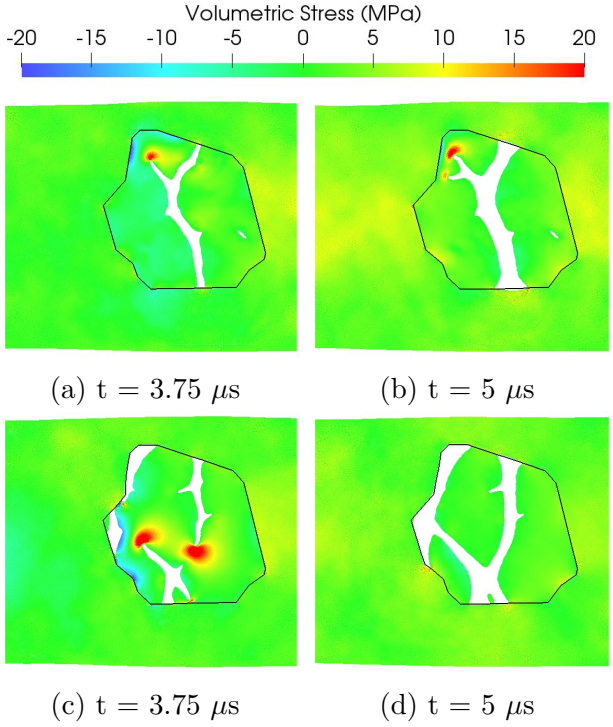

(a) t = 3.75 μs (b) t = 5 μs

(c) t = 3.75 μs (d) t = 5 μs

Figure 2.17. Volumetric stress and damage evolution for the tensile loading condition in a Sylgard-HMX system and G_c^{i}=10 J/m^2, (a-b) high quality surface, and (c-d) poor quality surface.

Temperature evolution

Similar to the tensile simulations, the change in temperature the HTPB-HMX system is negligible. Figure 2.18 shows the temperature field for the Sylgard-HMX system at 7.5 μs. The location of the maximum temperature is in the particle/binder interface in all the cases due to the relative sliding of the polymer and the particle where debonding occurs.

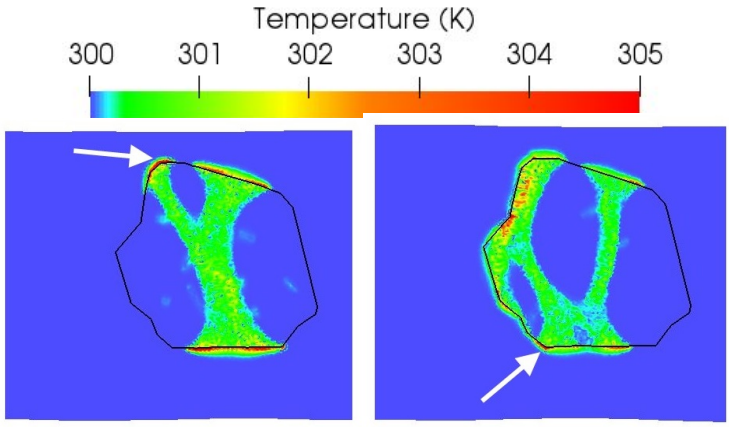

(a) High quality surface. (b) Poor quality surface.

Figure 2.18. Temperature field at t=7.5μs for tensile loading in Sylgard-HMX system with G_c^i= 10 J/m^2.

Figure 2.19 shows the temporal evolution of the average temperature of the region with radius $R = 8\mu m$, where the maximum temperature is achieved. For the HTPB binder a slight increase of temperature is predicted for the poor quality surface particle in the region where debonding occurs. The Sylgard-HMX system shows a larger temperature increase of up to 14 K. In agreement with the compressive simulations, the temperature in the Sylgard-HMX system increases earlier in the poor quality surface. Due to the higher stresses in the high quality surface particle system, the rate of heat generated by friction is larger and therefore a higher temperature is reached.

2.5 Conclusions

The response of single HMX particles inside HTPB and Sylgard binders is studied with combined experiments and simulations to understand the effect of the mechanical properties of the matrix, the adhesive properties, and the surface quality of the particle on fracture and temperature evolution.

The experiments show that crystal-binder interfacial debonding and crystal damage via cracking occurred under both, compressive and tensile, loading conditions with Sylgard binder. However, delamination predominated over cracking in the tensile trials. In the tensile experiments with HTPB, debonding and cracking rarely occurred. HTPB-HMX sys-

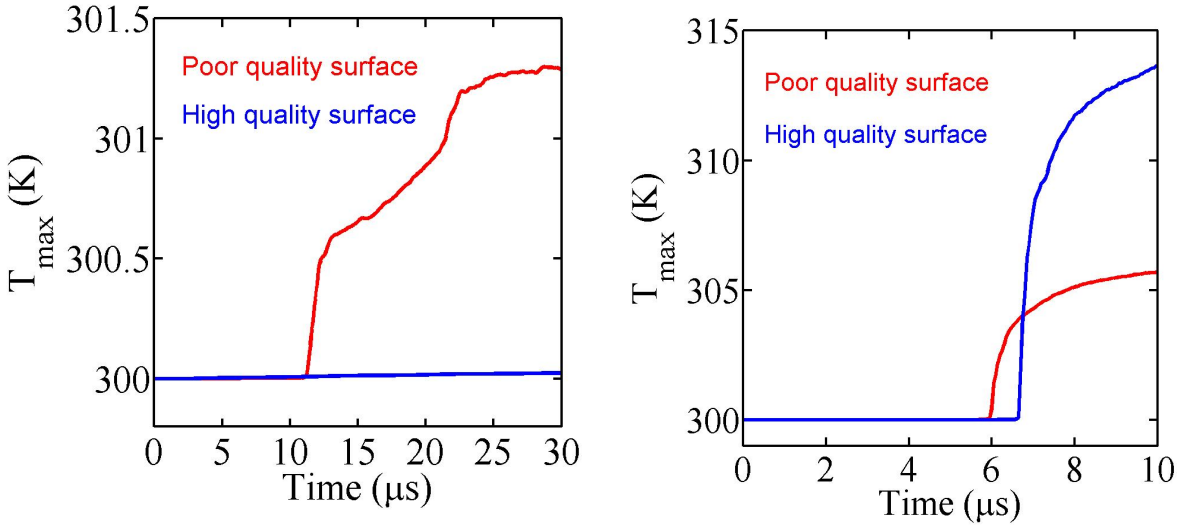

(a) HTPB binder

(b) Sylgard binder

Figure 2.19. Maximum temperature in the domain for tensile loading and $G_c^{\mathrm{i}} \geq$30 J/m^2

tems under compressive loading, in some cases showed cracking in the crystal, as opposed to crystal-binder debonding, while other cases showed neither cracking nor debonding. More tensile experiments would be helpful to gain further insight. Cracks likely initiated at surface defects or from internal voids, and future work should address the initial crystal conditions by μ-CT characterization of the crystals beforehand and through the use of recrystallized, low-defect HMX crystals with better surface morphology and low porosity.

Experiments and simulations show that HMX particles inside Sylgard are more sensitive to damage than in HTPB. A quantitative comparison of the simulations with experiments is difficult due to the complex geometry of the HMX particles. However, a qualitative comparison of the crack patterns and surface debonding in tension and compression indicates that the surface energy of the HTPB-HMX interface may be $G_c^{\mathrm{i}} \geq 30$ J/m^2. At lower strain rates, Walters et al. [16] calculated that $G_c^{\mathrm{i}} \sim$ 3-10 J/m^2

The simulations for the HMX-Sylgard system in tension and compression render similar results for the range of G_c^{i} analyzed here (10 to 90 J/m^2). Extensive damage in the particle and limited amount of debonding is obtained for the compression simulations. While the tensile simulations show debonding and crack growth in the particle interior. Comparison

of the simulations with the experiments in Figure 2.5 where only debonding is observed suggests that $G_c^{\mathrm{i}} \leq 10$ J/m^2. However, the experiment in Figure 2.6 shows vertical cracks and debonding in agreement with Figure 2.17 with G_c^{i} =10 J/m^2. As expected, lower values of surface energy lead to more prominent debonding.

Due to the higher stiffness of Sylgard, crack propagation is more likely in the particles inside the Sylgard binder than in HTPB. In both systems, initial cracks intersecting the particle/binder interface are the precursors for cracks propagating inside the particle. However, lower heat rates are predicted in the poor quality surface particle as a result of smaller stresses due to the extensive damage.

In summary, the combination of experiments and simulations like the one presented here, can be used to guide the choice of binders and surface quality in PBX. Even thought the results are quantitative, it is observed that binders with lower stiffness are less sensitive to crack propagation under non-shock conditions.

3. PBX MICROSTRUCTURE UNDER VIBRATION

Note: A version of this chapter has been accepted as a manuscript in Computational Materials Science with title 'Effect of particle proximity and surface properties on the response of PBX under vibration'

3.1 Introduction

Polymer bonded explosives (PBXs) are composite materials containing energetic particles in a polymeric binder that are designed to react under a controlled stimulus. Accidental ignition followed by initiation may occur when a PBX sample is subjected to mechanical impact or vibration [2]. The microstructure of PBX including binder properties, particle size distributions and volume fraction can be optimized to control the sensitivity of the composite to stimulus and subsequently initiation [1].

Several efforts focused on discrete particles to understand the causes of hot-spots formation during periodic excitation [54]–[59]. These references show that delamination of the particles from the binder, the amplitude of the excitation and the distance among particles play a prominent role in the nucleation of hot-spots. However, it is still not clear why under similar conditions hot-spots form in only some particles. For example, HMX-Sylgard samples were prepared using a production-grade β-HMX particle and a pre-delaminated production-grade-β-HMX crystal inside Sylgard binders [59]. When the samples were subjected to at 210.5 kHz frequency the temperature rise rates observed for the bonded particles were smaller than for the debonded particles.

It is also clear that the amplitude of the vibration is of key importance. A 44 μm amplitude resulted in a temperature rise rate of 22×10^3 K/s in sucrose crystals coated with polyethylene glycol inside PDMS [56]. The same experiments with an amplitude of 27 μm showed a slower temperature rise rate of 1.5×10^3 K/s.

Systems with three particles in contact showed intense heating and a temperature rise of 13 K after 4 seconds [58]. Particles with an average edge-to-edge separation of 380 μm, showed a temperature rise below 4 K after 4 seconds.

Experiments to understand the effect of the debonding of the binder were performed on single particle HMX-Sylgard samples using an ultrasonic transducer at 210.5 kHz frequency

[59]. Samples were prepared using a production-grade β-HMX particle and a pre-delaminated production-grade-β-HMX crystal inside Sylgard binders. The production-grade β-HMX particle showed a β-to-δ phase transition within 2.34 seconds and gas formation within 0.42 seconds. Given that the β to δ transition occurs at 433 K [60] while the decomposition occurs at 573 K [61], the temperature rise rates observed in these experiments are between 68-715 K/s. The pre-delaminated β HMX crystals showed similar behavior, although, in less amount of time. Finite elements simulations on a single HMX crystal inside Sylgard binder under vibration with 2-4 μm amplitude and 190-210 kHz frequency give further evidence of the importance of friction at cracks and delamination sites as heat sources under periodic loading [57]. These simulations showed temperature rise rates as high as 36×10^3 K/s for a bonded HMX crystal while 109×10^3 K/s for a partially debonded HMX crystal.

Another experimental study suggests that the distance among particles plays an important role in the formation of hot spots. Particles in close proximity with each other show a larger temperature increase [58] than particles located at an average distance 400 μm. However, these experiments show that the polymer binder adhesion is more important to reduce heating at frequencies 100-1000 kHz.

Unfortunately, the measurement of temperature in experiments makes difficult to determine the of hot-spots location and its source. Understanding the mechanisms of heath generation is important to improve the design PBXs that remain safe under periodic loading. In this work we focus on the prediction of local temperature in a PBX microstructure and in individual particles during periodic mechanical loading. Finite element simulations that include fracture dynamics and thermal transport are performed. The source of heat is the friction at cracks and particle-polymer debonded surfaces. Section 3.2 contains the mechanical, fracture and thermal transport models used in the simulations. In Section 3.3, the details of the geometry used in the simulations and results of microstructure and two particle simulations are reported. The findings are summarized in Section 3.4.

3.2 Methods

3.2.1 Phase field damage model

The phase field damage model (PFDM) is used to represent crack evolution in the material using a continuous variable, $c(\boldsymbol{x})$, ranging from 0 to 1 [23], [30], [32]. In this case, $c = 0$ is undamaged while $c = 1$ represents a completely damaged material. The crack surface, Γ is described as a diffuse-delta function $\gamma(c)$ [20], [33], [34],

$$\gamma\left(c\right) = \frac{1}{2l_0}\left(c^2 + l_0^2\left|\nabla c\right|^2\right) \tag{3.1}$$

In Equation 3.1, l_0 is a characteristic length that determines the transition from the damaged to undamaged region [31]. The characteristic length l_0 governs the crack thickness and it is represented in Figure 3.1. The dashed lines are the slope of the phase field curve at the intersection with the y axis [32].

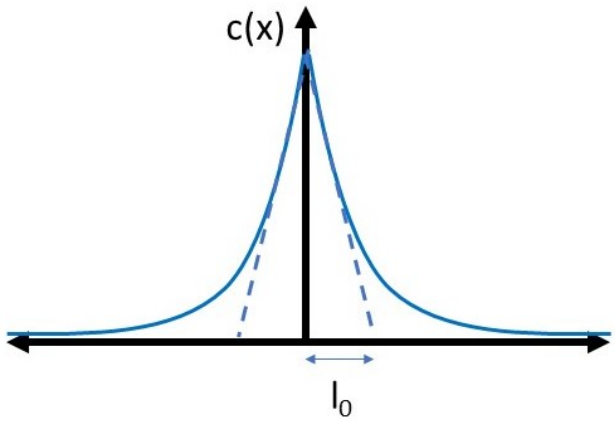

Figure 3.1. 1D representation of phase-field crack

The energy required to create new crack surfaces is calculated using the surface energy G_c following the Griffith's theory of fracture in brittle materials [24].

$$W_f = \int_\Gamma G_c d\Gamma = \int_V G_c \gamma\left(c\right) dV \tag{3.2}$$

where the integral over the crack area is approximated by the integral over the entire domain (V) using the diffuse-delta function.

The rate of fracture work needs to be positive to be thermodynamically consistent. This is achieved by imposing [30], [32],

$$\dot{W}_f = \int_V G_c \dot{\gamma}(c, \boldsymbol{\nabla} c) dV = \int_V G_c \delta_c \gamma \cdot \dot{c} \; dV \geq 0 \tag{3.3}$$

Equation 3.3 is reduced to the conditions: $\delta_c \gamma \geq 0$ and $\dot{c} \geq 0$, where the term, $\delta_c \gamma = \partial_c \gamma - \boldsymbol{\nabla} \cdot \partial_{\boldsymbol{\nabla} c} \gamma$ is the functional derivative of $\gamma(c, \boldsymbol{\nabla} c)$ with respect to c.

The evolution of the phase field is obtained From the Euler-Lagrange equations of the Lagrangian:

$$L\left(\dot{\boldsymbol{u}}, \boldsymbol{\epsilon}, c\right) = K\left(\dot{\boldsymbol{u}}\right) - A\left(\boldsymbol{\epsilon}, c\right) - W_f\left(c\right) \tag{3.4}$$

where K is the kinetic energy and A is the strain energy. The kinetic energy is calculated by integrating the kinetic energy density over the domain,

$$K\left(\dot{\boldsymbol{u}}\right) = \int_V \frac{1}{2} \rho \left|\dot{\boldsymbol{u}}\right|^2 dV \tag{3.5}$$

where ρ is the density and $\dot{\boldsymbol{u}}$ is the velocity. Similarly, the strain energy is given in terms of strain energy density $a\left(\boldsymbol{\epsilon}, c\right)$,

$$A\left(\boldsymbol{\epsilon}, c\right) = \int_V a\left(\boldsymbol{\epsilon}, c\right) dV \tag{3.6}$$

where $\boldsymbol{\epsilon}$ is the strain.

The strain energy density is split in two terms, with one term, a^+, being degraded with the damage:

$$a\left(\boldsymbol{\epsilon}, c\right) = \left[\left(1 - c\right)^2 + k_r\right] a^+\left(\boldsymbol{\epsilon}\right) + a^-\left(\boldsymbol{\epsilon}\right) \tag{3.7}$$

where k_r is a residual stiffness whose value is chosen to make the numerical scheme stable [31], [32]. Different variations of the PFDM are proposed based on how the strain energy is

separated into these two components [30], [32]. For HMX, the strain energy that is associated with the damage includes the positive volumetric and shear components [20]:

$$a^{+}(\boldsymbol{\epsilon}) = \frac{\lambda}{2}\langle \epsilon^{v} \rangle^{2} + \mu\left(\langle \epsilon_1 \rangle^{2} + \langle \epsilon_2 \rangle^{2} + \langle \epsilon_3 \rangle^{2}\right) \tag{3.8}$$

where ϵ_1, ϵ_2, and ϵ_3 are the principal strains, $\lambda = \dfrac{E\nu}{(1+\nu)(1-2\nu)}$ and $\mu = \dfrac{E}{2(1+\nu)}$ are Lame's parameters, and $\epsilon^{v} = \epsilon_1 + \epsilon_2 + \epsilon_3$ is the volumetric strain. The operator $\langle x \rangle$ is defined as,

$$\langle x \rangle = \begin{cases} x & \text{if } x \geq 0 \\ 0 & \text{if } x < 0 \end{cases} \tag{3.9}$$

The second term of the strain energy density is:

$$a^{-}(\boldsymbol{\epsilon}) = \frac{\lambda}{2}\left(\epsilon^{v} - \langle \epsilon^{v} \rangle\right)^{2} + \mu\left(\left(\epsilon_1 - \langle \epsilon_1 \rangle\right)^{2} + \left(\epsilon_2 - \langle \epsilon_2 \rangle\right)^{2} + \left(\epsilon_3 - \langle \epsilon_3 \rangle\right)^{2}\right) \tag{3.10}$$

The strain energy split used for the polymer considers that the damage occurs only under positive volumetric strain [7], [20], then,

$$a^{+}(\boldsymbol{\epsilon}) = \frac{1}{2}\left(\lambda + \frac{2\mu}{3}\right)\langle \epsilon^{v} \rangle^{2} \tag{3.11}$$

and

$$a^{-}(\boldsymbol{\epsilon}) = \frac{1}{2}\left(\lambda + \frac{2\mu}{3}\right)\left(\epsilon^{v} - \langle \epsilon^{v} \rangle\right)^{2} + \mu\boldsymbol{\epsilon}^{d} : \boldsymbol{\epsilon}^{d} \tag{3.12}$$

where $\boldsymbol{\epsilon}^{d}$ is the deviatoric strain tensor given by,

$$\boldsymbol{\epsilon}^{d} = \boldsymbol{\epsilon} - \frac{\epsilon^{v}}{3}\boldsymbol{I} \tag{3.13}$$

Here, $\boldsymbol{I}$ is the identity tensor. The stress is obtained by differentiating the strain energy expression:

$$\boldsymbol{\sigma} = \frac{\partial a(\boldsymbol{\epsilon}, c)}{\partial \boldsymbol{\epsilon}} = \left[(1-c)^{2} + k_r\right]\frac{\partial a^{+}(\boldsymbol{\epsilon})}{\partial \boldsymbol{\epsilon}} + \frac{\partial a^{-}(\boldsymbol{\epsilon})}{\partial \boldsymbol{\epsilon}} \tag{3.14}$$

Equation 3.14 indicates how the stiffness of the damaged material is reduced by the phase field parameter.

The Euler-Lagrange equations are derived from equation 3.4 and result in

$$\nabla \cdot \boldsymbol{\sigma} = \rho \frac{\partial^2 \boldsymbol{u}}{\partial t^2} \tag{3.15}$$

and the rate of change of phase field variable with respect to time is given by [33],

$$\dot{c} = \frac{1}{\eta} \left\langle l_0 \Delta c + 2(1-c) \frac{a^+(\boldsymbol{\epsilon})}{G_c} - \frac{c}{l_0} \right\rangle \ , \tag{3.16}$$

where η is a coefficient that controls the relaxation of the system towards equilibrium. This model represents a rate independent behavior when $\eta \to 0$ [35]. The finite element framework MOOSE (Multiphysics Object Oriented Simulation Environment) [33], [36] is used to solve these equations. The velocity and acceleration terms in the numerical process are calculated using the Newmark time integration scheme [62].

$$\ddot{\boldsymbol{u}}^{n+1} = \frac{\boldsymbol{u}^{n+1} - \boldsymbol{u}^n}{\beta \Delta t^2} - \frac{\dot{\boldsymbol{u}}^n}{\beta \Delta t} + \frac{\beta - 0.5}{\beta} \ddot{\boldsymbol{u}}^n \tag{3.17}$$

$$\dot{\boldsymbol{u}}^{n+1} = \dot{\boldsymbol{u}}^n + (1-\gamma)\, \Delta t \ddot{\boldsymbol{u}}^n + \gamma \Delta t \ddot{\boldsymbol{u}}^{n+1} \tag{3.18}$$

where β and γ are the integration parameters. The parameters chosen are $l_0 = 40$ μm, $\eta = 0.1$ s/m, Δt $= 5$ ns, $\beta = 0.3025$, $\gamma = 0.6$ and $k_r = 1 \times 10^{-6}$ [22].

3.2.2 Heat generation by frictional sliding

Along with the mechanical problem, the integral form of the thermal transport equation is solved in the domain. The only heat source is the frictional heating at cracks, thus, the volumetric heat source density, $\dot{q}$, is considered zero.

$$\int_V \rho C \frac{\partial T}{\partial t} dV = -\int_{\partial S} \boldsymbol{h} \cdot \mathbf{n} dA \tag{3.19}$$

where C is the specific heat, T is the temperature, $\boldsymbol{h} = -k\nabla T$ is the heat flux per unit area across the surface ∂S with normal $\boldsymbol{n}$, and k is the thermal conductivity. The frictional heat flux at the cracks is given by [7], [22]:

$$\boldsymbol{h} \cdot \boldsymbol{n} = -\mu_f \langle -t_n \rangle v_s \tag{3.20}$$

where μ_f is the friction coefficient, t_n is the normal component of the traction at the crack surface, and v_s is the tangential component of the velocity jump across the crack surfaces. Equation 3.20 ensures that heat can only be generated when the traction is negative. The tangential component of the velocity jump across the crack surfaces is given by the gradient of the velocity in the direction normal to the crack.

$$\boldsymbol{v}^+ - \boldsymbol{v}^- = (\nabla \boldsymbol{v} \cdot \hat{\boldsymbol{n}})\, l_0 \tag{3.21}$$

where the approximate distance between the crack surfaces is assumed to be equal to the characteristic length, l_0, and the gradient of the phase field renders the normal to the crack surface [39].

$$\hat{\boldsymbol{n}} = -\frac{\nabla c}{|\nabla c|} \tag{3.22}$$

3.3 Results

In most PBXs the energetic material particles account for 85-95% of the volume composition. The response of the microstructure is dominated by the individual components and their interfaces that cause large heterogeneities in the deformation, stress and temperature fields. To identify the mechanisms of hot-spot formation in these type of microstructures under periodic loading, the response of a complex microstructure as well as simplified configurations are investigated. The simplified configurations consist of two particles with different arrangements to explore the effect of relative particle size, particle-particle distance and relative location.

3.3.1 Material properties

Micro-indentation experiments on HMX have shown the surface energy to be 0.06 J/m^2 [25]. However, the critical energy release rate also includes plastic dissipation at the crack tip. Thus, the value of G$_c$ is increased 2 J/m^2 to incorporate the effect of plasticity at the crack tip [22], [39]. The energy release rates for various amorphous polymers have been shown to be in the range of 200-400 J/m^2 [41], [42], G$_c$= 400 J/m^2 is chosen for Sylgard.

The thermal conductivity is degraded when the material is damaged. The loss in conductivity is incorporated using the damage phase field as [35],

$$k\left(c\right) = \left(1-c\right)^2 k^u \tag{3.23}$$

where k^u is the conductivity of the undamaged material. The material properties used in the simulations are listed in Table 3.1.

Table 3.1. Material properties and numerical parameters used in the simulations [43]–[48]

Property	HMX	Sylgard
E [GPa]	15	0.15
ν	0.35	0.48
ρ [kg/m^3]	1903	1030
G_c [J/m^2]	2	400
k^u [W/m·K]	0.31	0.18
C [J/kg·K]	1200	1100
μ_f	1	1

3.3.2 Initial crack distribution

The particles used in PBXs contain defects that will be included in the simulations as initial cracks. These are represented with an initial distribution of the damage phase field [33]:

$$c\left(\boldsymbol{r}, t=0\right) = c_{max} \mathrm{e}^{-\frac{|\boldsymbol{r}|}{l_0}} \tag{3.24}$$

where $\boldsymbol{r}$ is the distance perpendicular to the crack line and c_{max} is the value of the phase field at the center of the crack. Random initial cracks are created with c_{max} following a uniform distribution with range (0.8,1). The initial crack length and crack orientations are chosen according to Gaussian distributions with a mean 100μm, and a standard deviation 35μm and mean 0° and a standard deviation 45° with respect to the horizontal axis, respectively. The cracks are located only in the particles following a uniform distribution.

3.3.3 PBX simulations

The geometry used in the simulations, shown in Figure 3.2 is adapted from a PBX sample in reference [63]. In Figure 3.2 the HMX covers 78% of the area. The mesh used in the simulations consists of approximately 90,000 triangular elements with an average size of 4μm. The initial cracks are shown in white where the value of the phase field variable is c>0.6. An intermediate level of porosity in HMX-based PBX is considered to be 4-20% [64]. In this study, an initial crack density of 5% is considered in the HMX and there are no cracks in the Sylgard matrix. A periodic loading with an amplitude of 4 μm and a frequency of 210.5 kHz is applied to the bottom boundary while the other three boundaries are free. The initial temperature in the domain is 300 K and the heat flux is zero at the boundaries.

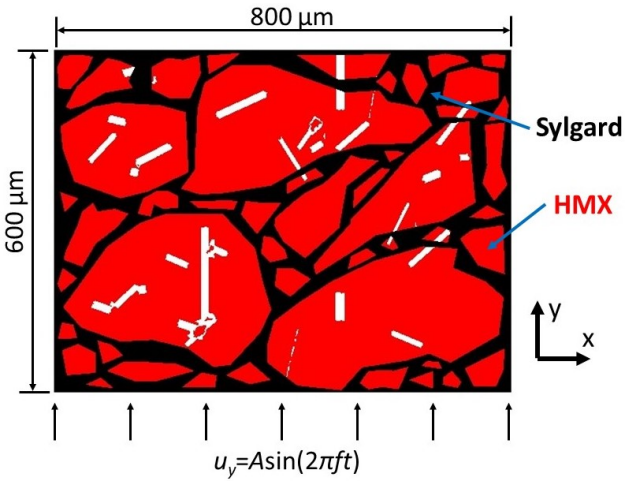

Figure 3.2. Microstructure domain

Figure 3.3 shows the contour plot of the volumetric stress and the damage evolution for approximately 5 loading cycles. Compressive and tensile volumetric stresses of up to 30 MPa

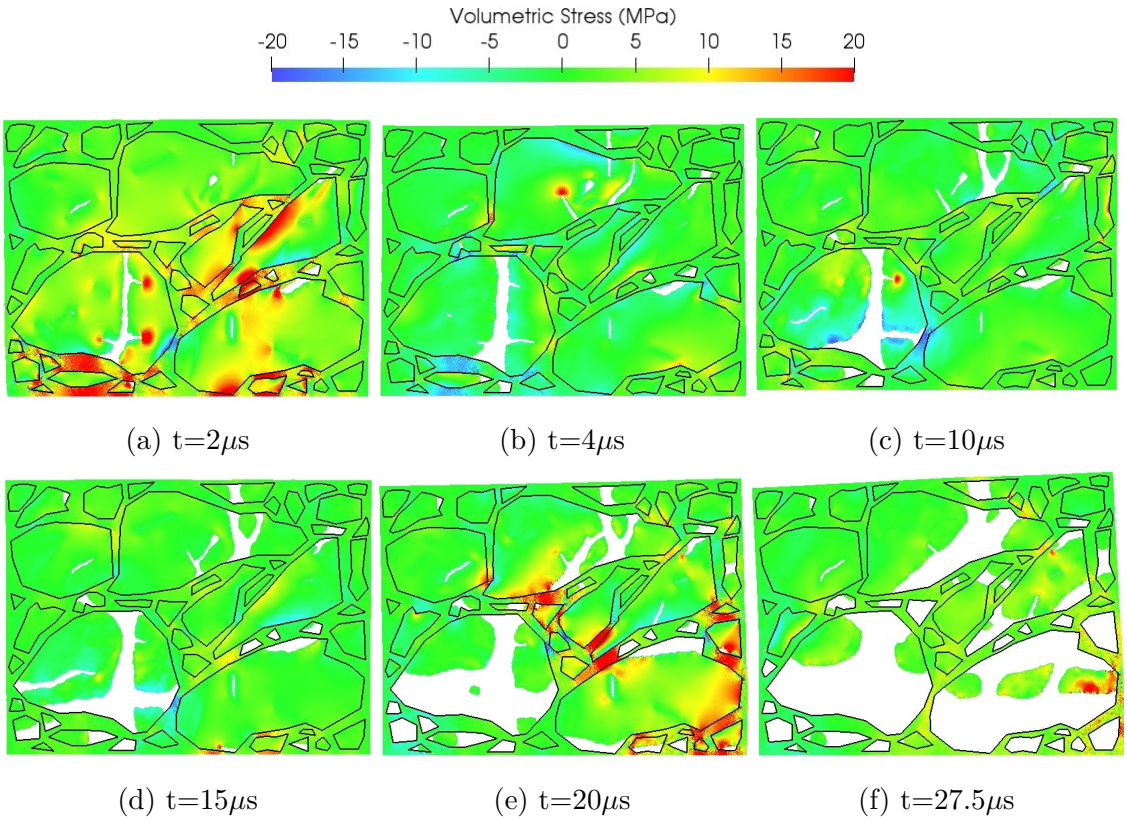

(a) t=2μs (b) t=4μs (c) t=10μs

(d) t=15μs (e) t=20μs (f) t=27.5μs

Figure 3.3. Volumetric stress and damage evolution in a PBX microstructure under vibration with an initial crack density of 5%. The damage is shown in white for values of $c > 0.9$.

are observed in the microstructure. The large particles near the bottom boundary, where the displacement is applied, show damage propagation earlier than any other particles. Most of the small particles close to the loading boundary damage completely.

The distance among the particles in this microstructure varies from 10 μm to 100 μm. Larger volumetric stresses are observed where the particles are closer, where new cracks nucleate and the existing cracks propagate. As expected, more damage is observed in the larger particles. In agreement with previous simulations [7], [22], the initial cracks located near the particle-polymer interface propagate earlier than the cracks in the interior of the particles . Debonding is also observed at particle-polymer interfaces.

The temperature field in the microstructure after t=27.5μs is shown in Figure 3.4. Larger temperatures are observed in the regions near the bottom of the sample where the periodic displacement is applied. The temperature increase in the small particles depends strongly on their location and proximity to the large particles.

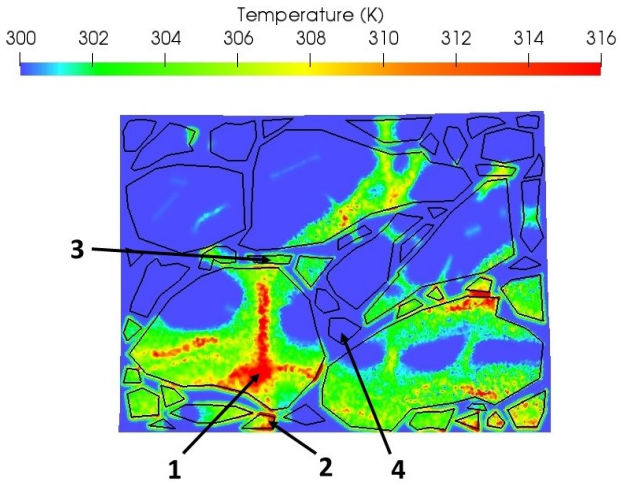

Figure 3.4. Temperature field at t=27.5μm

Four particles are labeled to compare their temperature evolution, the maximum local temperature in each particle is presented in Figure 3.5. This temperature is calculated as an average over a region of radius 8μm where the temperature reaches the largest value. The crack surfaces in particle 1 show the highest temperature. Particle 2 lies between the loading boundary and Particle 1, it is completely damaged and shows a temperature rise of almost 12 K. Particle 3 lies between particle 1 and another large particle on top and shows partial damage and a temperature rise of 3 K. Whereas particle 4 with no initial damage shows no crack development and thus, no temperature increase. The local maximum temperature rise rate is 7.3$\times$ 10^5 K/s in particle 1, while there is no temperature increase in other particles.

The presence of multiple particles makes it difficult to understand the local effects, such as stress concentrations, particle size and distance between two adjacent particles on the damage and temperature evolution. In order to understand these details, simulations with only two particles with different arrangements are presented in the following section.

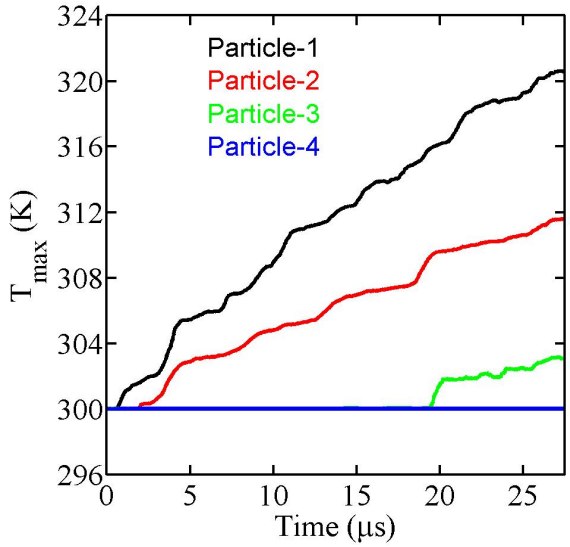

Figure 3.5. Local temperature evolution in the particles

3.3.4 Two particles simulations

The samples in Figure 3.6 are subjected to the same vibration loading used in the previous section. The effect of the relative location of the small particle as well the distance to the large particle are studied. The large particle is approximately 800 μm in height and 500 μm in width whereas the small particle has an approximate diameter of 100 μm. Figure 3.6(a) will be referred as parallel configuration, and Figure 3.6(b) will be called shielded configuration. In both configurations, the distance between the particles is varied, with d = 40, 100 and 200 μm. The domain is discretized using triangular mesh elements with an average size of 10 μm. All the material properties given in Table 3.1 are used in the simulations. A random initial crack distribution is chosen for the large particle with a density of 8.6%. The small particle contains only a crack intersecting its surface.

Figure 3.7 shows the volumetric stress and the damage at t=30μs. Stress concentrations at the crack tips are visible in Figure 3.7 (f). The damage evolution in the large particle is similar in all the figures with crack propagation and debonding from the bottom interface. In the shielded configuration, the small particle does not show any damage evolution for any of the distances considered. The shielding effect of the large particle on the small particle

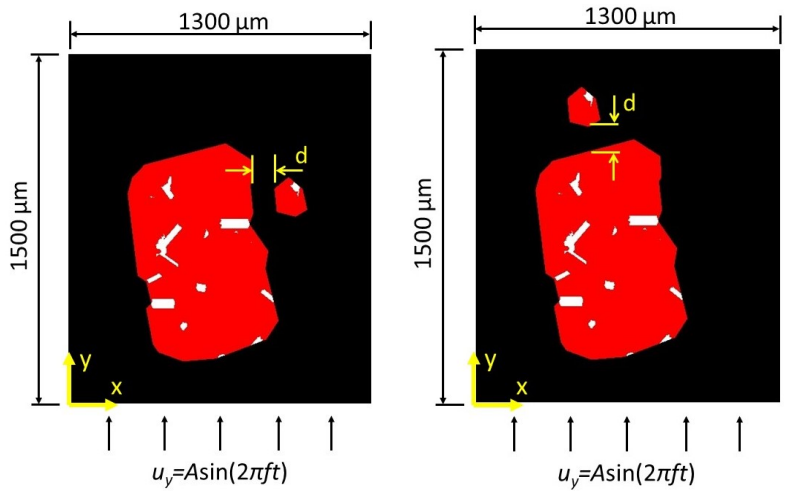

(a) Parallel configuration (b) Shielded configuration

Figure 3.6. Two particle domain used in the simulations

is also observed in the simulations of the microstructure in Figure 3.3. In the parallel configuration, Figure 3.7 (d)-(f), the initial crack in the small particle propagates. When the distance between the particles decreases the damage rate increases and the small particle is damaged earlier.

Initially the maximum temperature occurs in the large particle near the bottom interface facing the incident vibration loading, see Figure 3.8. The large particle damage starts increasing at around 5 μs with crack propagation and debonding from the bottom surface. The crack in the small particle begins to propagate after t=25μs, see Figure 3.9(a). The evolution of the temperature, see Figure 3.9(b), follows the damage evolution. The temperature in the small particle decreases for increasing distances between the two particles. In the shielded configuration the temperature and damage evolution in the large particle are similar to the one in the parallel configuration. On the other hand, the small particle in the shielded configuration does not show any damage and therefore, no temperature increase.

To explain the effect of the particle distance we also look at other factor that affect the heat generation due to friction at the cracks: the traction at the crack surface. Figure 3.10 shows the evolution of the average volumetric stress in the small particle for both configurations at different distances. In the shielded configuration the stress oscillates between -4 and 3 MPa. Initially, the response in the parallel configuration is similar bur after 25 μs

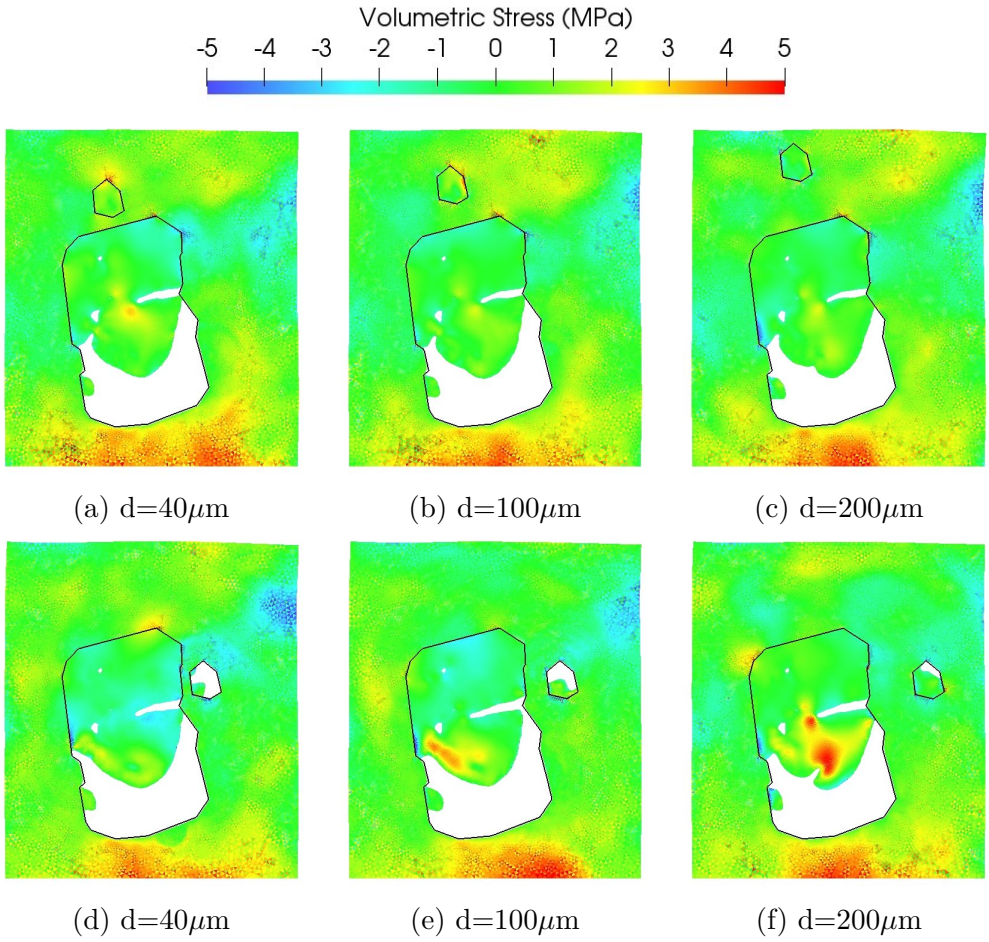

(a) d=40μm (b) d=100μm (c) d=200μm

(d) d=40μm (e) d=100μm (f) d=200μm

Figure 3.7. Volumetric stress and damage in HMX-Sylgard at t=30μs, (a-c) shielded configuration, and (d-f) parallel configuration. The white regions correspond to a damage field c>0.9.

the stresses are only compressive due to the particle damage. When the crack penetrates the whole particle, it only can sustain compressive stresses. The increase in the compressive stress is due to the debonding of the interface between the large particle and the polymer in the region close to the small particle, shown in Figure 3.11.

The periodic loading causes lateral waves in the domain, when a wave passes from the polymer to the large particle, part of wave is reflected. As the debonded region between the large particle and the polymer increases, more of the compressive stress is reflected back in to the polymer and eventually to the small particle increasing the compressive stress [65]–[68]. The compressive stress amplitude increases in the small particle and is expected to reach a

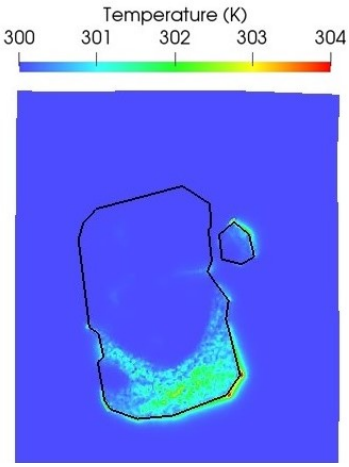

Figure 3.8. Temperature field at t=30 μs .

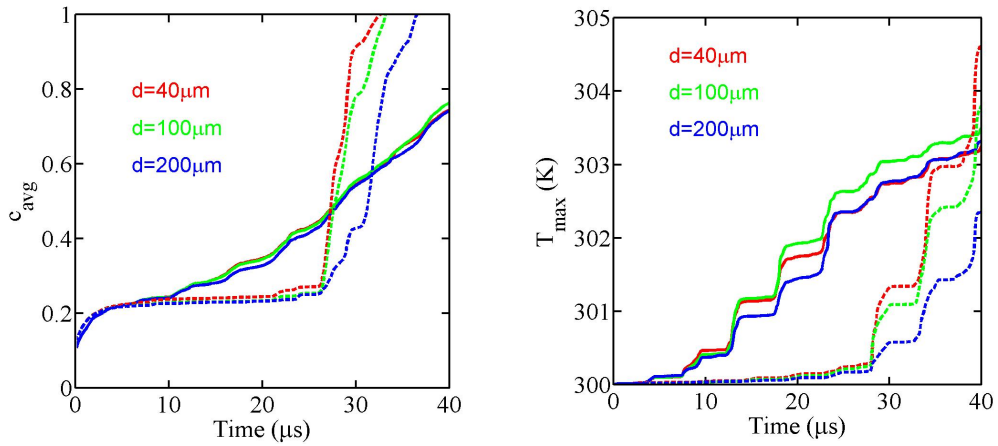

(a) Average damage field. (b) Maximum temperature evolution.

Figure 3.9. (a) Average damage field in the particles in the parallel configuration. (b) Evolution of the maximum temperature. Solid lines represent the large particle and dashed lines the small particle.

constant value after complete debonding of the region of the large particle. The amplitude of the compressive volumetric stress decreases with increasing distance between the particles. Thus, the closer to the large particle the higher the temperature rise.

Viscoelastic dissipation in the polymer is suggested to be another source of heat [4], [54]. Considering that all viscoelastic energy dissipated under cyclic loading is transformed to heat, the maximum temperature rise in the polymer can be estimated as $\Delta T_{max} = \frac{\pi \langle \epsilon \rangle^2 G f \Delta t}{\rho c_v}$

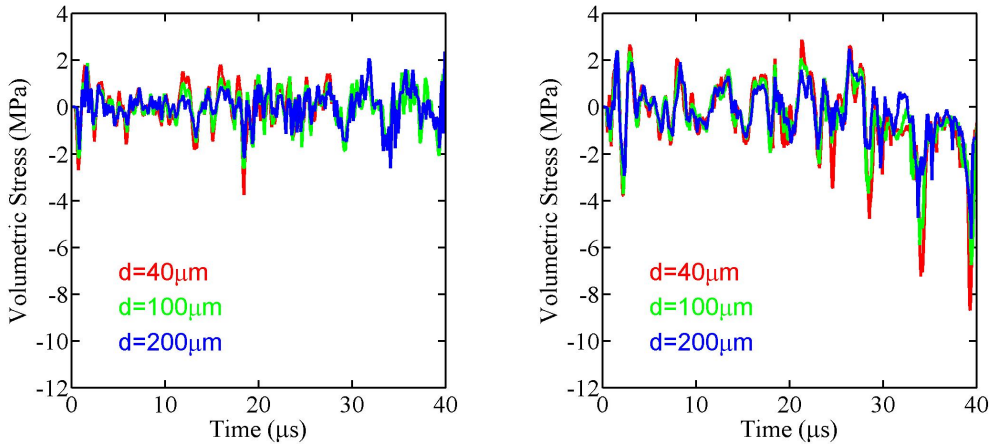

(a) Shielded configuration (b) Parallel configuration

Figure 3.10. Average volumetric stress in small particle with interfacial crack

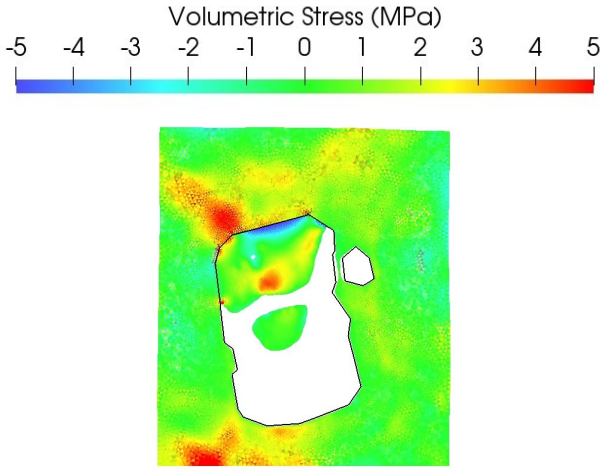

Figure 3.11. Volumetric stress and damage in the parallel configuration with d=40μm at t=40μs. The while region corresponds to a damage field of $c > 0.9$.

[69] where $\langle\epsilon\rangle$ is the shear strain, G is the shear loss modulus, f is the frequency and Δt is the time.

Figure 3.12 shows the average shear strain in the area between the two particles in the parallel configuration. When the distance between the particles is d=40μ, a maximum value of the shear strain, $\langle\epsilon\rangle^2 = 0.0012$ is obtained. Assuming the shear loss modulus to be 1 kPa [70], the maximum temperature rise in the polymer due to viscoelastic heat generation could

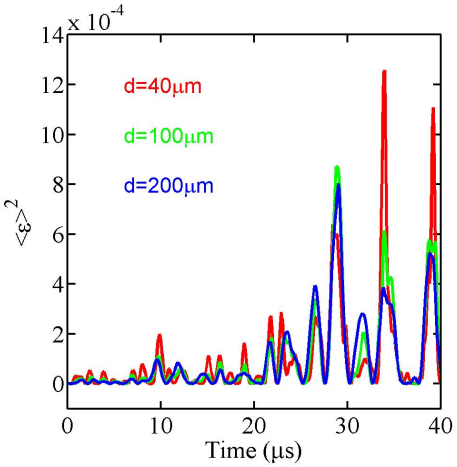

Figure 3.12. Average shear strain in the polymer between the two particles in the parallel configuration.

be estimated to be, ΔT_{max} $\leq 2.8\times10^{-5}$ K after t=40μs which is five orders of magnitude smaller than the temperature increase due to frictional heat generation.

3.4 Conclusions

The response of a PBX microstructure under of a periodic excitation with 210.5 kHz frequency and 4μm amplitude is studied to understand the formation of hot spots. The individual particles of the composite are examined to understand the effect of distance, relative location, and size. Given that the loading boundary is rigid, larger particles closer to the loading boundary damage earlier. This agrees with results that show that higher density of packing decreases the sensitivity of the PBX [71]. A maximum local temperature increase of 21 K after 27.5 μs over an area with radius 8 μm is observed due to frictional heating at crack surfaces. In comparison the average temperature increase over the whole sample is 1.7 K in 27.5 μs.

The response of two HMX particles inside a Sylgard binder is examined to identify the mechanisms of nucleation of hot spots. Two configurations are used, one with the two particles arranged parallel to the incident wave and another with the small particle shielded by the large particle. The small particle fully damages after 25 μs in the parallel configuration and remains undamaged in the shielded configuration at 40 μs. Therefore, there is a negligible

increase of temperature in the shielded configuration compared to the parallel configuration. In agreement with the experiments by Roberts et al. [58] the increase in temperature is larger when the particles are closer. The stress in the binder near the particles increases when the particles are closer to each other. However, the heat generation due to viscoelastic heating is unimportant compared to friction during the initial stages.

In the large particles surface cracks advance to the interior and debonding starts at the bottom and later propagates to the sides in both configurations. Initially, the local temperature increase is higher in the large particle due to the presence of longer cracks and delaminated surfaces that act as heat sources. However, the temperature may increase later in the smaller at a larger rate, see Figure 3.9 (b).

Heating rates as high as 22×10^3 K/s have been observed in the experiments by You et al. [56] with sucrose crystals inside PDMS under periodic vibration with an amplitude 44 μm. The experiments by Roberts et al. [59] have shown temperature rise rates in the range of 68-715 K/s in an HMX particle. The simulations predict the maximum rate of temperature rise in the parallel configuration when the distance between the particles is d=40μm. The average temperature rate obtained is 15×10^3 K/s in the large particle and 33.75×10^3 K/s in the small particle, which is in the same order of magnitude observed in the experiments.

This work gives further evidence that friction at cracks and delamination sites are important sources of heating in these composite materials in agreement with previous results [55]–[59]. Furthermore, delamination also contributes to an increase in compressive stress at neighboring particles supplying a gain in the fictional heating source. This suggest that binder adhesion is key to mitigate heating in PBXs under periodical excitation.

4. ANISOTROPIC FRACTURE IN HMX

4.1 Introduction

Most of the energetic materials are anisotropic in nature. The HMX possess an anisotropic elasticity tensor and several cleavage planes [72], [73]. Weaker bonds between the atoms in the crystal forms the cleavage planes. Crack propagation is preferred along weakest cleavage plane as compared to other cleavage planes as less energy is required to cause the damage. To understand the effect of anisotropy on the damage evolution, and consequent temperature rise, anisotropic fracture model is implemented in MOOSE framework. Simulations are run to verify the implementation and results are discussed.

The temperature dependency of pressure in the material is described by equation of state. So far in this study, only low velocity impact and vibrations with amplitude in the order of few microns were considered as the loading conditions on PBX. Thus, the effect of equation of state was negligible. As the velocity of impact increases, non-linear effects of pressure-temperature relation become important. Mie-Gruneisen equation of state is implemented in MOOSE framework for small strain formulation which is coupled with anisotropic fracture code. Preliminary simulation of HMX-Sylgard at impact velocity of 100 m/s are presented that show the effect of equation of state on damage evolution.

4.2 Methods

4.2.1 Anisotropic damage model

Anisotropy in the damage model is associated with the cleavage planes and elastic properties of the material [37], [73]–[75]. Crack propagation along weak cleavage plane is preferred over other planes when a penalty is introduced on the other planes using an artificial parameter. The model implementation is explained in the following subsection.

Crack propagation along weak cleavage plane

The phase field damage model explained in section 2.2 considers the isotropic crack propagation where the crack surface density $\gamma(c)$ is given as [32],

$$\gamma_{iso}\left(c, \nabla c\right) = \frac{1}{2l_0}\left(c^2 + l_0^2 \left|\nabla c\right|^2\right) = \frac{1}{2l_0}c^2 + \frac{l_0}{2}\boldsymbol{I} : \left(\nabla c \otimes \nabla c\right) \tag{4.1}$$

where the subscript i*so* denotes crack surface density function for isotropic material. The anisotropic damage model is constructed as a modification of the isotropic damage model by using a tensor $\boldsymbol{\omega}$ [74].

$$\gamma_{total}\left(c, \nabla c\right) = \frac{1}{2l_0}c^2 + \frac{l_0}{2}\boldsymbol{\omega} : \left(\nabla c \otimes \nabla c\right) \tag{4.2}$$

where $\boldsymbol{\omega}$ is defined as [74],

$$\boldsymbol{\omega} = \boldsymbol{I} + \beta\left(\boldsymbol{I} - \boldsymbol{n} \otimes \boldsymbol{n}\right) \tag{4.3}$$

Here, $\boldsymbol{n}$ denotes the unit normal of the weakest or preferred cleavage plane whereas β introduces a penalty for cleavage planes that are not normal to $\boldsymbol{n}$. The limit $\beta = 0$ would render isotropic damage.

Implementation

The MOOSE implementation of isotropic damage includes use of isotropic crack surface density function, γ_{iso}. The effect of anisotropy is implemented in MOOSE in a form of derived class from isotropic damage. In this case, the contribution of anisotropic damage is

calculated separately. Thus, the anisotropic term is defined as, $\gamma_{aniso} = \gamma_{total} - \gamma_{iso}$ which is simplified as follows,

$$\begin{aligned}
\gamma_{total}\left(c, \nabla c\right) &= \frac{1}{2l_0}c^2 + \frac{l_0}{2}\left[\boldsymbol{I} + \beta\left(\boldsymbol{I} - \boldsymbol{n}\otimes\boldsymbol{n}\right)\right] : \left(\nabla c \otimes \nabla c\right) \\
&= \frac{1}{2l_0}c^2 + \frac{l_0}{2}\boldsymbol{I} : \left(\nabla c \otimes \nabla c\right) + \frac{\beta l_0}{2}\left(\boldsymbol{I} - \boldsymbol{n}\otimes\boldsymbol{n}\right) : \left(\nabla c \otimes \nabla c\right) \\
&= \gamma_{iso}\left(c, \nabla c\right) + \frac{\beta l_0}{2}\left(\boldsymbol{I} - \boldsymbol{n}\otimes\boldsymbol{n}\right) : \left(\nabla c \otimes \nabla c\right)
\end{aligned} \tag{4.4}$$

Thus the contribution of anisotropy is given as,

$$\gamma_{aniso} = \frac{\beta l_0}{2}\left(\boldsymbol{I} - \boldsymbol{n}\otimes\boldsymbol{n}\right) : \left(\nabla c \otimes \nabla c\right) \tag{4.5}$$

The work dissipated in friction is calculated using equation 2.1 which is then used in energy minimization. MOOSE implementation involves calculation of variational derivative and weak form integral. The weak form integral is solved to find residual of equation which is used as a marker of convergence. The variational derivative is given as,

$$\delta\gamma_{aniso} = -\beta l_0\left(\nabla^2 c - \boldsymbol{n}\otimes\boldsymbol{n} : \nabla\nabla c\right) \tag{4.6}$$

Using ψ as test function, the contribution of γ_{aniso} to the weak form residual $\mathbb{R}_{aniso}$ is derived as follows:

$$\begin{aligned}
\mathbb{R}_{aniso} &= \int_\Omega \left[-\beta l_0\left(\nabla^2 c - \boldsymbol{n}\otimes\boldsymbol{n} : \nabla\nabla c\right)\right]\psi dV \\
&= -\beta l_0 \int_\Omega \left(\nabla^2 c - \boldsymbol{n}\otimes\boldsymbol{n} : \nabla\nabla c\right)\psi dV \\
&= \beta l_0\left[-\int_\Omega \psi\left(\nabla^2 c\right) dV + \int_\Omega \psi\left(\boldsymbol{n}\otimes\boldsymbol{n} : \nabla\nabla c\right) dV\right]
\end{aligned} \tag{4.7}$$

The first integral term in equation 4.7 can be simplified as,

$$
\begin{aligned}
-\int_{\Omega}\psi\left(\nabla^{2}c\right)dV = &= -\int_{\Omega}\Big[\nabla\cdot(\psi\nabla c)-\nabla\psi\cdot\nabla c\Big]dV \\
&= -\int_{\Omega}\nabla\cdot(\psi\nabla c)\,dV+\int_{\Omega}(\nabla\psi\cdot\nabla c)\,dV \\
&= -\cancelto{0}{\int_{\partial\Omega}\psi\nabla c\cdot\boldsymbol{n}dS}+\int_{\Omega}(\nabla\psi\cdot\nabla c)\,dV
\end{aligned}
\tag{4.8}
$$

The first term in the expression 4.8 cancels out as the flux of scalar field going out of domain is zero. The second integral in equation 4.7 can be simplified as,

$$
\begin{aligned}
\int_{\Omega}\psi\left(\boldsymbol{n}\otimes\boldsymbol{n}:\nabla\nabla c\right)dV &= \int_{\Omega}\Big[\nabla\cdot\left(\psi\boldsymbol{n}\left(\boldsymbol{n}\cdot\nabla c\right)\right)-\left(\boldsymbol{n}\cdot\nabla\psi\right)\left(\boldsymbol{n}\cdot\nabla c\right)-\left(\psi\nabla\cdot\boldsymbol{n}\right)\left(\boldsymbol{n}\cdot\nabla c\right)\Big]dV \\
&= \int_{\Omega}\nabla\cdot\left(\psi\boldsymbol{n}\left(\boldsymbol{n}\cdot\nabla c\right)\right)dV-\int_{\Omega}\left(\boldsymbol{n}\cdot\nabla\psi\right)\left(\boldsymbol{n}\cdot\nabla c\right)dV \\
&\qquad -\int_{\Omega}\left(\psi\nabla\cdot\boldsymbol{n}\right)\left(\boldsymbol{n}\cdot\nabla c\right)dV \\
&= \cancelto{0}{\int_{\partial\Omega}\psi\boldsymbol{n}\left(\boldsymbol{n}\cdot\nabla c\right)\cdot\boldsymbol{n}dS}-\int_{\Omega}\left(\boldsymbol{n}\cdot\nabla\psi\right)\left(\boldsymbol{n}\cdot\nabla c\right)dV \\
&\qquad -\int_{\Omega}\cancelto{0}{\left(\psi\nabla\cdot\boldsymbol{n}\right)}\left(\boldsymbol{n}\cdot\nabla c\right)dV
\end{aligned}
\tag{4.9}
$$

The first term in the expression 4.9 cancels out as the flux of phase field going out of domain is zero while the last term cancels out as the divergence of a constant vector field is zero. Thus, the residual term that needs to be implemented into the solver becomes,

$$
\mathbb{R}_{aniso}=\beta l_{0}\left[\int_{\Omega}\left(\nabla\psi\cdot\nabla c\right)dV-\int_{\Omega}\left(\boldsymbol{n}\cdot\nabla\psi\right)\left(\boldsymbol{n}\cdot\nabla c\right)dV\right] \tag{4.10}
$$

The matrix system of equations is solved using Newton-Raphson method [36] where gradient of the residual is used to find more accurate solution in the subsequent iterations. The gradient of residual $\mathbb{J}$ is calculated in MOOSE framework using expression,

$$
\mathbb{J}_{\mathrm{ij}}\left(c_{h}\right)=\frac{\partial\mathbb{R}_{\mathrm{i}}\left(c_{h}\right)}{\partial c_{\mathrm{j}}} \tag{4.11}
$$

where $\mathbb{J}_{\mathrm{ij}}\left(c_h\right)$ denotes $()_{\mathrm{ij}}^{th}$ element of $\mathbb{J}$ matrix at h^{th} nodal point in the mesh. The derivative of phase field and its gradient at h^{th} node with respect to j^{th} node is calculated using trial function ϕ as follows [36]:

$$\frac{\partial c_h}{\partial c_{\mathrm{j}}} = \sum_k \frac{\partial}{\partial c_{\mathrm{j}}}\left(c_k \phi_k\right) = \phi_{\mathrm{j}} \tag{4.12}$$

$$\frac{\partial\left(\nabla c_h\right)}{\partial c_{\mathrm{j}}} = \sum_k \frac{\partial}{\partial c_{\mathrm{j}}}\left(c_k \nabla\phi_k\right) = \nabla\phi_{\mathrm{j}} \tag{4.13}$$

Thus, the gradient of residual corresponding to additional anisotropic term is given in terms of test and trial function as,

$$\mathbb{J}_{aniso} = \beta l_0 \left[\int_\Omega \left(\nabla\psi \cdot \nabla\phi_{\mathrm{j}}\right) dV - \int_\Omega \left(\boldsymbol{n} \cdot \nabla\psi\right)\left(\boldsymbol{n} \cdot \nabla\phi_{\mathrm{j}}\right) dV\right] \tag{4.14}$$

Equations 4.10 and 4.14 are implemented in MOOSE framework. The above implemented code is contributed to MOOSE framework with the name "ACInterfaceCleavageFracture". This code is added in appendix A.

The implemented model is verified using mode-I crack propagation over a rectangular domain, shown in figure 4.1. The cleavage plane normal used is (-0.707,0.707,0) which is at 45^o from X-axis. The effect of penalty parameter β is shown in figure 4.2.

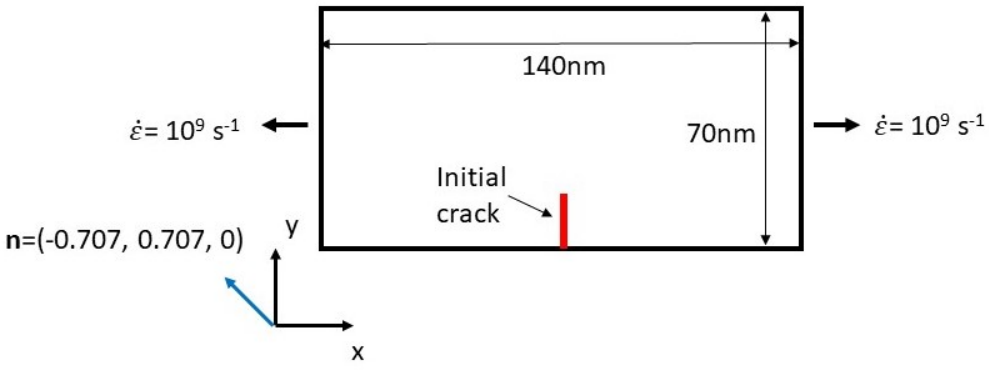

Figure 4.1. Domain for mode-I crack simulation

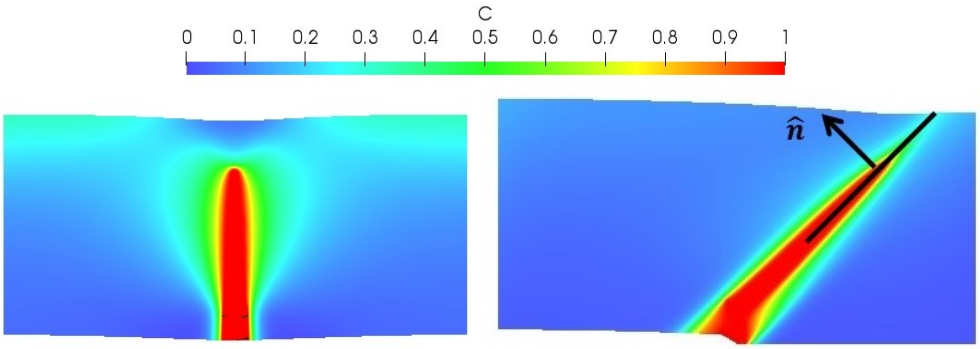

(a) β=0, t=0.45ns (b) β=100, t=0.325ns

Figure 4.2. Effect of penalty parameter β. Crack propagation along 45^o

Anisotropic stiffness tensor

The phase field damage model explained in section 2.2 considers the eigendecomposition of strain to define the strain energy density based on isotropic stiffness tensor. In case of anisotropic stiffness tensor, the eigendecomposition of stress is used to define the strain energy. The positive part of the stress is calculated using positive projection eigendecomposition tensor,

$$\boldsymbol{\sigma}^{+} = \mathbb{P}^{+} : \boldsymbol{\sigma} \tag{4.15}$$

while negative part of stress is given as,

$$\boldsymbol{\sigma}^{-} = \boldsymbol{\sigma} - \boldsymbol{\sigma}^{+} \tag{4.16}$$

where $\mathbb{P}^{+}$ is the positive projection tensor given by [76],

$$\mathbb{P}^{+} = \sum_{a=1}^{3} d_a \cdot (\boldsymbol{M}_a \otimes \boldsymbol{M}_a) + \sum_{a=1}^{3} \sum_{b \neq a}^{3} \theta_{ab} \cdot (\mathbb{G}_{ab} + \mathbb{G}_{ba}) \tag{4.17}$$

The variables used in equation 4.17 are given below as,

$$d_a = \begin{cases} 1 & \text{if } \sigma_a > 0 \\ 0 & \text{if } \sigma_a \leq 0 \end{cases} \tag{4.18}$$

$$\boldsymbol{M}_a = \boldsymbol{n}_a \otimes \boldsymbol{n}_a \tag{4.19}$$

$$\theta_{ab} = \begin{cases} \dfrac{1}{2}\left(\dfrac{\langle\sigma_a\rangle - \langle\sigma_b\rangle}{\sigma_a - \sigma_b}\right) & \text{if } \sigma_a \neq \sigma_b \\ \dfrac{1}{4}\left(d_a + d_b\right) & \text{otherwise} \end{cases} \tag{4.20}$$

$$\begin{aligned} \mathbb{G}_{ab}^{\mathrm{ij}kl} &= M_a^{\mathrm{i}k} M_b^{\mathrm{j}l} + M_a^{\mathrm{i}l} M_b^{\mathrm{j}k} \\ \mathbb{G}_{ba}^{\mathrm{ij}kl} &= M_b^{\mathrm{i}k} M_a^{\mathrm{j}l} + M_b^{\mathrm{i}l} M_a^{\mathrm{j}k} \end{aligned} \tag{4.21}$$

where,

$$\langle\sigma_a\rangle = \begin{cases} \sigma_a & \text{if } \sigma_a > 0 \\ 0 & \text{if } \sigma_a \leq 0 \end{cases} \tag{4.22}$$

The eigendecomposition of stress gives,

$$\boldsymbol{\sigma} = \begin{bmatrix} \boldsymbol{n}_1 & \boldsymbol{n}_2 & \boldsymbol{n}_3 \end{bmatrix} \begin{bmatrix} \sigma_1 & 0 & 0 \\ 0 & \sigma_2 & 0 \\ 0 & 0 & \sigma_3 \end{bmatrix} \begin{bmatrix} \boldsymbol{n}_1^T \\ \boldsymbol{n}_2^T \\ \boldsymbol{n}_3^T \end{bmatrix} \tag{4.23}$$

where σ_1, σ_2 & σ_2 are principle stresses and $\boldsymbol{n}_1$, $\boldsymbol{n}_2$ & $\boldsymbol{n}_3$ are corresponding eigenvectors. By definition the original matrix is constructed from eigenvalue as,

$$\boldsymbol{\sigma} = \sum_{a}^{3} \sigma_a \left(\boldsymbol{n}_a \otimes \boldsymbol{n}_a \right) = \sum_{a}^{3} \sigma_a \boldsymbol{M}_a \tag{4.24}$$

Thus, the first term in equation 4.17 denotes that the positive principle stress entirely contributes to the positive part of the stress calculated using positive projection eigendecomposition tensor. By definition, the partial derivative of eigenvector and its outer product with respect to original matrix is given by [76],

$$2\frac{\partial \boldsymbol{n}_a}{\partial \boldsymbol{\sigma}} = \sum_{b \neq a}^{3} \frac{1}{\sigma_a - \sigma_b} \boldsymbol{n}_b \otimes \left(\boldsymbol{n}_a \otimes \boldsymbol{n}_b + \boldsymbol{n}_b \otimes \boldsymbol{n}_a \right) \tag{4.25}$$

$$2\frac{\partial \boldsymbol{M}_a}{\partial \boldsymbol{\sigma}} = \sum_{b \neq a}^{3} \frac{1}{\sigma_a - \sigma_b} \left(\mathbb{G}_{ab} + \mathbb{G}_{ba} \right) \tag{4.26}$$

Thus, comparing the above equation with equation 4.17, the second term in equation 4.17 denotes the projection of one eigenvector in the direction of another eigenvector. This projection, if positive, also contributes to the positive part of the stress.

Thus, in this way, the anisotropic stress calculation is used to calculate strain energy density using,

$$a^{+}\left(\boldsymbol{\sigma} \right) = \frac{1}{2} \boldsymbol{\sigma}^{+} : \boldsymbol{\varepsilon} \tag{4.27}$$

$$a^{-}\left(\boldsymbol{\sigma} \right) = \frac{1}{2} \boldsymbol{\sigma}^{-} : \boldsymbol{\varepsilon} \tag{4.28}$$

while stress and strain energy is degraded using function,

$$\boldsymbol{\sigma} = \left[\left(1 - c^2 \right) + k_r \right] \boldsymbol{\sigma}^{+} + \boldsymbol{\sigma}^{-} \tag{4.29}$$

$$a = \left[\left(1 - c^2 \right) + k_r \right] a^{+} + a^{-} \tag{4.30}$$

This code is implemented in MOOSE framework to incorporate elastic anisotropy in HMX.

Examples using projection tensor

The fourth order positive projection tensor is constructed using positive eigenvalues of a second order tensor. In this subsection, some examples are given to understand the construction. For a given stress tensor, eigenvalues σ_a, eigenvectors $\boldsymbol{n}_a$ and outerproduct of eigenvector $\boldsymbol{M}_a$ are calculated. The quantities d_a and θ_{ab} are calculated using Equation 4.18 and Equation 4.20 respectively. Using the eigenvectors and corresponding matrix $\boldsymbol{M}_a$, the positive part of stress tensor is calculated as using Equation 4.15. The matlab code used to calculate positive part of stress is attached in appendix B.

Example-1: Pure volumetric

$$\boldsymbol{\sigma} = \begin{bmatrix} 1 & 0 & 0 \\ 0 & 1 & 0 \\ 0 & 0 & 1 \end{bmatrix} \qquad \sigma_a = \begin{bmatrix} 1 \\ 1 \\ 1 \end{bmatrix} \qquad d_a = \begin{bmatrix} 1 \\ 1 \\ 1 \end{bmatrix}$$

$$\boldsymbol{n}_1 = \begin{bmatrix} 1 \\ 0 \\ 0 \end{bmatrix} \qquad \boldsymbol{M}_1 = \begin{bmatrix} 1 & 0 & 0 \\ 0 & 0 & 0 \\ 0 & 0 & 0 \end{bmatrix}$$

$$\boldsymbol{n}_2 = \begin{bmatrix} 0 \\ 1 \\ 0 \end{bmatrix} \qquad \boldsymbol{M}_2 = \begin{bmatrix} 0 & 0 & 0 \\ 0 & 1 & 0 \\ 0 & 0 & 0 \end{bmatrix}$$

$$\boldsymbol{n}_3 = \begin{bmatrix} 0 \\ 0 \\ 1 \end{bmatrix} \qquad \boldsymbol{M}_3 = \begin{bmatrix} 0 & 0 & 0 \\ 0 & 0 & 0 \\ 0 & 0 & 1 \end{bmatrix}$$

$$\theta_{ab} = \begin{bmatrix} 0.5 & 0.5 & 0.5 \\ 0.5 & 0.5 & 0.5 \\ 0.5 & 0.5 & 0.5 \end{bmatrix} \qquad \boldsymbol{\sigma}^{+} = \begin{bmatrix} 1 & 0 & 0 \\ 0 & 1 & 0 \\ 0 & 0 & 1 \end{bmatrix}$$

Example-2: Uniaxial stress

$$\boldsymbol{\sigma} = \begin{bmatrix} 1 & 0 & 0 \\ 0 & 0 & 0 \\ 0 & 0 & 0 \end{bmatrix} \qquad \sigma_a = \begin{bmatrix} 0 \\ 0 \\ 1 \end{bmatrix} \qquad d_a = \begin{bmatrix} 0 \\ 0 \\ 1 \end{bmatrix}$$

$$\boldsymbol{n}_1 = \begin{bmatrix} 0 \\ 1 \\ 0 \end{bmatrix} \qquad \boldsymbol{M}_1 = \begin{bmatrix} 0 & 0 & 0 \\ 0 & 1 & 0 \\ 0 & 0 & 0 \end{bmatrix}$$

$$\boldsymbol{n}_2 = \begin{bmatrix} 0 \\ 0 \\ 1 \end{bmatrix} \qquad \boldsymbol{M}_2 = \begin{bmatrix} 0 & 0 & 0 \\ 0 & 0 & 0 \\ 0 & 0 & 1 \end{bmatrix}$$

$$\boldsymbol{n}_3 = \begin{bmatrix} 1 \\ 0 \\ 0 \end{bmatrix} \qquad \boldsymbol{M}_3 = \begin{bmatrix} 1 & 0 & 0 \\ 0 & 0 & 0 \\ 0 & 0 & 0 \end{bmatrix}$$

$$\theta_{ab} = \begin{bmatrix} 0 & 0 & 0.5 \\ 0 & 0 & 0.5 \\ 0.5 & 0.5 & 0.5 \end{bmatrix} \qquad \boldsymbol{\sigma}^{+} = \begin{bmatrix} 1 & 0 & 0 \\ 0 & 0 & 0 \\ 0 & 0 & 0 \end{bmatrix}$$

Example-3

$$\boldsymbol{\sigma} = \begin{bmatrix} 1 & 0 & 0 \\ 0 & -1 & 0 \\ 0 & 0 & -1 \end{bmatrix} \qquad \sigma_a = \begin{bmatrix} -1 \\ -1 \\ 1 \end{bmatrix} \qquad d_a = \begin{bmatrix} 0 \\ 0 \\ 1 \end{bmatrix}$$

$$\boldsymbol{n}_1 = \begin{bmatrix} 0 \\ 1 \\ 0 \end{bmatrix} \qquad \boldsymbol{M}_1 = \begin{bmatrix} 0 & 0 & 0 \\ 0 & 1 & 0 \\ 0 & 0 & 0 \end{bmatrix}$$

$$\boldsymbol{n}_2 = \begin{bmatrix} 0 \\ 0 \\ 1 \end{bmatrix} \qquad \boldsymbol{M}_2 = \begin{bmatrix} 0 & 0 & 0 \\ 0 & 0 & 0 \\ 0 & 0 & 1 \end{bmatrix}$$

$$\boldsymbol{n}_3 = \begin{bmatrix} 1 \\ 0 \\ 0 \end{bmatrix} \qquad \boldsymbol{M}_3 = \begin{bmatrix} 1 & 0 & 0 \\ 0 & 0 & 0 \\ 0 & 0 & 0 \end{bmatrix}$$

$$\theta_{ab} = \begin{bmatrix} 0 & 0 & 0.25 \\ 0 & 0 & 0.25 \\ 0.25 & 0.25 & 0.5 \end{bmatrix} \qquad \boldsymbol{\sigma}^{+} = \begin{bmatrix} 1 & 0 & 0 \\ 0 & 0 & 0 \\ 0 & 0 & 0 \end{bmatrix}$$

Example-4: Compression in plane

$$\boldsymbol{\sigma} = \begin{bmatrix} -1 & 0 & 0 \\ 0 & -1 & 0 \\ 0 & 0 & 0 \end{bmatrix} \qquad \sigma_a = \begin{bmatrix} -1 \\ -1 \\ 0 \end{bmatrix} \qquad d_a = \begin{bmatrix} 0 \\ 0 \\ 0 \end{bmatrix}$$

$$\boldsymbol{n}_1 = \begin{bmatrix} 1 \\ 0 \\ 0 \end{bmatrix} \qquad \boldsymbol{M}_1 = \begin{bmatrix} 1 & 0 & 0 \\ 0 & 0 & 0 \\ 0 & 0 & 0 \end{bmatrix}$$

$$\boldsymbol{n}_2 = \begin{bmatrix} 0 \\ 1 \\ 0 \end{bmatrix} \qquad \boldsymbol{M}_2 = \begin{bmatrix} 0 & 0 & 0 \\ 0 & 1 & 0 \\ 0 & 0 & 0 \end{bmatrix}$$

$$\boldsymbol{n}_3 = \begin{bmatrix} 0 \\ 0 \\ 1 \end{bmatrix} \qquad \boldsymbol{M}_3 = \begin{bmatrix} 0 & 0 & 0 \\ 0 & 0 & 0 \\ 0 & 0 & 1 \end{bmatrix}$$

$$\theta_{ab} = \begin{bmatrix} 0 & 0 & 0 \\ 0 & 0 & 0 \\ 0 & 0 & 0 \end{bmatrix} \qquad \boldsymbol{\sigma}^{+} = \begin{bmatrix} 0 & 0 & 0 \\ 0 & 0 & 0 \\ 0 & 0 & 0 \end{bmatrix}$$

Example-5: Pure shear

$$\boldsymbol{\sigma} = \begin{bmatrix} 1 & 0 & 0 \\ 0 & -0.5 & 0 \\ 0 & 0 & -0.5 \end{bmatrix} \qquad \sigma_a = \begin{bmatrix} -0.5 \\ -0.5 \\ 1 \end{bmatrix} \qquad d_a = \begin{bmatrix} 0 \\ 0 \\ 1 \end{bmatrix}$$

$$\boldsymbol{n}_1 = \begin{bmatrix} 0 \\ 1 \\ 0 \end{bmatrix} \qquad \boldsymbol{M}_1 = \begin{bmatrix} 0 & 0 & 0 \\ 0 & 1 & 0 \\ 0 & 0 & 0 \end{bmatrix}$$

$$\boldsymbol{n}_2 = \begin{bmatrix} 0 \\ 0 \\ 1 \end{bmatrix} \qquad \boldsymbol{M}_2 = \begin{bmatrix} 0 & 0 & 0 \\ 0 & 0 & 0 \\ 0 & 0 & 1 \end{bmatrix}$$

$$\boldsymbol{n}_3 = \begin{bmatrix} 1 \\ 0 \\ 0 \end{bmatrix} \qquad \boldsymbol{M}_3 = \begin{bmatrix} 1 & 0 & 0 \\ 0 & 0 & 0 \\ 0 & 0 & 0 \end{bmatrix}$$

$$\theta_{ab} = \begin{bmatrix} 0 & 0 & 0.33 \\ 0 & 0 & 0.33 \\ 0.33 & 0.33 & 0.5 \end{bmatrix} \qquad \boldsymbol{\sigma}^{+} = \begin{bmatrix} 1 & 0 & 0 \\ 0 & 0 & 0 \\ 0 & 0 & 0 \end{bmatrix}$$

Example-6: Pure shear

$$\boldsymbol{\sigma} = \begin{bmatrix} 0 & 1 & 0 \\ 1 & 0 & 0 \\ 0 & 0 & 0 \end{bmatrix} \qquad \sigma_a = \begin{bmatrix} -1 \\ 0 \\ 1 \end{bmatrix} \qquad d_a = \begin{bmatrix} 0 \\ 0 \\ 1 \end{bmatrix}$$

$$\boldsymbol{n}_1 = \begin{bmatrix} -0.707 \\ 0.707 \\ 0 \end{bmatrix} \qquad \boldsymbol{M}_1 = \begin{bmatrix} 0.5 & -0.5 & 0 \\ -0.5 & 0.5 & 0 \\ 0 & 0 & 0 \end{bmatrix}$$

$$\boldsymbol{n}_2 = \begin{bmatrix} 0 \\ 0 \\ 1 \end{bmatrix} \qquad \boldsymbol{M}_2 = \begin{bmatrix} 0 & 0 & 0 \\ 0 & 0 & 0 \\ 0 & 0 & 1 \end{bmatrix}$$

$$\boldsymbol{n}_3 = \begin{bmatrix} 0.707 \\ 0.707 \\ 0 \end{bmatrix} \qquad \boldsymbol{M}_3 = \begin{bmatrix} 0.5 & 0.5 & 0 \\ 0.5 & 0.5 & 0 \\ 0 & 0 & 0 \end{bmatrix}$$

$$\theta_{ab} = \begin{bmatrix} 0 & 0 & 0.25 \\ 0 & 0 & 0.5 \\ 0.25 & 0.5 & 0.5 \end{bmatrix} \qquad \boldsymbol{\sigma}^{+} = \begin{bmatrix} 0.5 & 0.5 & 0 \\ 0.5 & 0.5 & 0 \\ 0 & 0 & 0 \end{bmatrix}$$

4.2.2 Equation of State

The Mie-Gruneisen equation of state [77] is used to calculate pressure,

$$p_{eos} = \frac{K_0 \eta \left(1 - \frac{\Gamma}{2}\eta\right)}{(1 - s\eta)^2} + \Gamma \rho_0 C_v \left(T - T_0\right) \tag{4.31}$$

where, K_0 denotes bulk modulus, v denotes specific volume, Γ denotes Gruneisen parameter, s denotes slope of $U_s - U_p$ line and subscript 0 denotes reference state. For small strain formulation, the parameter η is given by,

$$\eta = 1 - \frac{v}{v_0} = 1 - (1 + \mathrm{tr}\,(\varepsilon)) = -\mathrm{tr}\,(\varepsilon) \tag{4.32}$$

The pressure is used to calculate the component of stress coming from equation of state as follows:

$$\boldsymbol{\sigma}_{eos} = -p_{eos}\boldsymbol{I} \tag{4.33}$$

which is then used to calculate the total stress as follows:

$$\boldsymbol{\sigma}_{tot} = \boldsymbol{\sigma}_{eos} + \boldsymbol{\sigma}_{cpl} \tag{4.34}$$

Here the subscript *cpl* denotes coupling term, which is the part of stress tensor not accounted by the equation of state and is calculated by differentiating the coupling part of strain energy density by strain [73]. The coupling strain energy is calculated by subtracting p-v energy from the total strain energy.

$$\begin{aligned}
\boldsymbol{\sigma}_{cpl} &= \frac{\partial \psi_{cpl}}{\partial \boldsymbol{\varepsilon}} \\
&= \frac{\partial}{\partial \boldsymbol{\varepsilon}} \left[\frac{1}{2} \boldsymbol{\varepsilon} : \mathbb{C} : \boldsymbol{\varepsilon} - \frac{1}{2} K_0 \delta^2 \right] \\
&= \mathbb{C} : \boldsymbol{\varepsilon} - \frac{\partial}{\partial \boldsymbol{\varepsilon}} \left[\frac{1}{2} K_0 \delta^2 \right] \\
&= \mathbb{C} : \boldsymbol{\varepsilon} - K_0 \frac{\partial}{\partial \boldsymbol{m}\varepsilon} \left[\frac{1}{2} \delta^2 \right] \\
&= \mathbb{C} : \boldsymbol{\varepsilon} - K_0 \delta \frac{\partial \delta}{\partial \boldsymbol{\varepsilon}} \\
&= \mathbb{C} : \boldsymbol{\varepsilon} - K_0 \delta \boldsymbol{I}
\end{aligned} \tag{4.35}$$

The total stress calculated is then split into a positive part and a negative part as required by the damage model. The positive part is given by,

$$\boldsymbol{\sigma}^+ = \boldsymbol{\sigma}^+_{eos} + \mathbb{P}^+ : \boldsymbol{\sigma}_{cpl} \tag{4.36}$$

while the negative part is given by,

$$\boldsymbol{\sigma}^- = \boldsymbol{\sigma} - \boldsymbol{\sigma}^+ = \boldsymbol{\sigma}^-_{eos} + \left(\boldsymbol{\sigma}_{cpl} - \mathbb{P}^+ : \boldsymbol{\sigma}_{cpl} \right) \tag{4.37}$$

The calculation of strain energy density is based on energy from equation of state and the coupling part. The energy from equation of state is calculated from p-v energy while the coupling part is calculated using mechanical strain energy relation. Thus, the positive part of strain energy density is given as,

$$a^+ = \begin{cases} \int_1^{\frac{v}{v_0}} p_{eos} \; d\left(\dfrac{v}{v_0} \right) + \dfrac{1}{2} \left(\mathbb{P}^+ : \boldsymbol{\sigma}_{cpl} \right) : \boldsymbol{\varepsilon} & \text{if } \dfrac{v}{v_0} \geq 1 \\ \dfrac{1}{2} \left(\mathbb{P}^+ : \boldsymbol{\sigma}_{cpl} \right) : \boldsymbol{\varepsilon} & \text{if } \dfrac{v}{v_0} < 1 \end{cases} \tag{4.38}$$

while the negative part is given as,

$$a^{-} = \begin{cases} \frac{1}{2}\left(\boldsymbol{\sigma}_{cpl} - \mathbb{P}^{+} : \boldsymbol{\sigma}_{cpl}\right) : \boldsymbol{\varepsilon} & \text{if } \frac{v}{v_0} \geq 1 \\ \int_1^{\frac{v}{v_0}} p_{eos}\, d\left(\frac{v}{v_0}\right) + \frac{1}{2}\left(\boldsymbol{\sigma}_{cpl} - \mathbb{P}^{+} : \boldsymbol{\sigma}_{cpl}\right) : \boldsymbol{\varepsilon} & \text{if } \frac{v}{v_0} < 1 \end{cases} \tag{4.39}$$

The p-v part of strain energy can be simplified using pressure equation 4.31 as,

$$\int_1^{\frac{v}{v_0}} p_{eos}\, d\left(\frac{v}{v_0}\right) = \int_1^{\frac{v}{v_0}} \left[\frac{K_0\eta\left(1-\frac{\Gamma}{2}\eta\right)}{(1-s\eta)^2} + \Gamma\rho_0 C_v\left(T-T_0\right)\right] d\left(\frac{v}{v_0}\right) \tag{4.40}$$

$$= \int_1^{\frac{v}{v_0}} \left[\frac{K_0\eta\left(1-\frac{\Gamma}{2}\eta\right)}{(1-s\eta)^2}\right] d\left(\frac{v}{v_0}\right) + \int_1^{\frac{v}{v_0}} \Gamma\rho_0 C_v\left(T-T_0\right) d\left(\frac{v}{v_0}\right) \tag{4.41}$$

where the second integral term is given as,

$$\int_1^{\frac{v}{v_0}} \Gamma\rho_0 C_v\left(T-T_0\right) d\left(\frac{v}{v_0}\right) = \Gamma\rho_0 C_v\left(T-T_0\right)\left(\frac{v}{v_0}-1\right) \tag{4.42}$$

while the first integral term is calculated by parts as,

$$\int_1^{\frac{v}{v_0}} \left[\frac{K_0\eta\left(1-\frac{\Gamma}{2}\eta\right)}{(1-s\eta)^2}\right] d\left(\frac{v}{v_0}\right) = \frac{A}{s - s^2\left(1-\frac{v}{v_0}\right)} - \frac{B\log\left[1-s\left(1-\frac{v}{v_0}\right)\right]}{s} + C\left(1-\frac{v}{v_0}\right) - \frac{A}{s} \tag{4.43}$$

where A, B and C are coefficients of integration by parts defined as,

$$A = K_0 \left[\Gamma \left(\frac{1}{2s^2} + \frac{1}{2} - \frac{1}{s} \right) - 1 \right]$$
$$B = K_0 \left[\Gamma \left(\frac{1}{s} - \frac{1}{2} \right) + 1 \right]$$
$$C = -\frac{K_0 \Gamma}{2s^2}$$

Spurious oscillations are introduced in stress values at the wave front in dynamic computation due to numerical artifact [78]. To reduce these, artificial viscosity term is added in the stress calculation in terms of pressure, which is given as [78],

$$p_{av} = \rho L_{\mathrm{e}} \left(C_0 L_{\mathrm{e}} \left(\mathrm{tr}(D) \right)^2 - C_1 c \left(\mathrm{tr}(D) \right) \right) \tag{4.44}$$

where ρ is density of material, L_{e} is the element size, c is the sound speed and $\mathrm{tr}(D)$ denotes the trace of the strain rate tensor. Here, C_0 and C_1 are method parameters.

Validation of equation of state

A cube of unit length is compressed at various specific volumes and resulting pressure from simulation is compared with experimental values from literature [37], [79]–[83] to verify the implementation of Mie-Gruneisen equation of state in MOOSE framework. Figure 4.3 shows the implementation is reasonable.

4.3 Results

4.3.1 Simulation setup

Impact simulations are run on a domain shown in figure 4.4. The slab of HMX is sandwiched between two layers of Sylgard layer to allow lateral expansion of HMX and accelerate damage behavior. The top and bottom boundaries of Sylgard are set to be periodic while right boundary is fixed in X-direction. The impact of 100 m/s is applied on left boundary as displacement boundary condition. An initial crack of length 100 μm is introduced in HMX at an orientation angle of 45^o from horizontal.

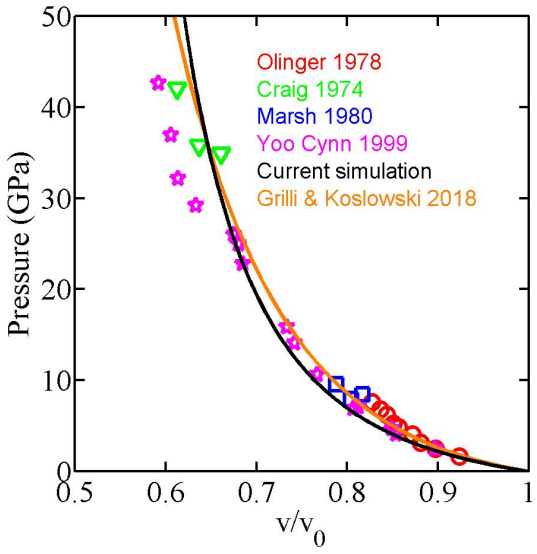

Figure 4.3. Mie-Gruneisen equation of state verification

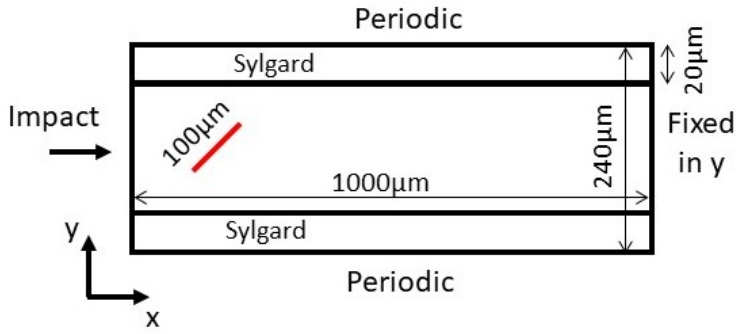

Figure 4.4. HMX-Sylgard domain for high velocity impact

Material properties

The HMX is considered to be anisotropic elastic material with stiffness tensor coefficients as given in table 4.1. Other constants used are detailed in table 2.1. The HMX is oriented in such a way that the impact is applied in (100) direction. The cleavage plane is oriented in the direction of (0,1,1) with respect to the orientation of HMX [73]. The value of penalty parameter $\beta = 10$ is used in this simulation. Equation of state is used to calculate pressure that is dependent on temperature. Coupling term is incorporated as explained in section 4.2. The material constants used in equation of state are given in table 4.2.

Table 4.1. Elastic constants of HMX [84]

Coefficient	Value [GPa]
C_{11}	25.1
C_{12}	9.7
C_{13}	12.8
C_{15}	-1.3
C_{22}	22.3
C_{23}	11.8
C_{25}	4.6
C_{33}	21.8
C_{35}	1.4
C_{44}	9.7
C_{46}	3.18
C_{55}	11.036
C_{66}	8.66

Table 4.2. Equation of state coefficients for HMX [84]

Property	HMX
Gruneisen parameter, Γ	0.7
Slope of $U_s - U_p$ line	2.29
Viscosity parameter, C_0	0.1
Viscosity parameter, C_1	1.0
Sound speed, s [km/s]	2.77
Reference temperature T_0 [K]	300.0

4.3.2 Impact on HMX-Sylgard

Figure 4.5 shows the volumetric stress while figure 4.6 shows deviatoric stress in the HMX-Sylgard domain at an impact velocity of 100 m/s. The damaged region, $c > 0.9$, is denoted in white. Only the left half of the domain (500μm) is shown in the figures as the wave has not reached the right half and it remains in the zero stress state. The wave reaches the right side of domain around 300 ns. During compression, the horizontal plane in the middle is expected to have the maximum tensile stress in the vertical direction due to presence of Sylgard on top and bottom of HMX. The periodic boundary conditions are imposed on the top boundary of top layer of sylgard and bottom boundary of bottom layer of sylgard. Thus, the crack is expected to propagate in the horizontal direction for $\beta = 0$. In

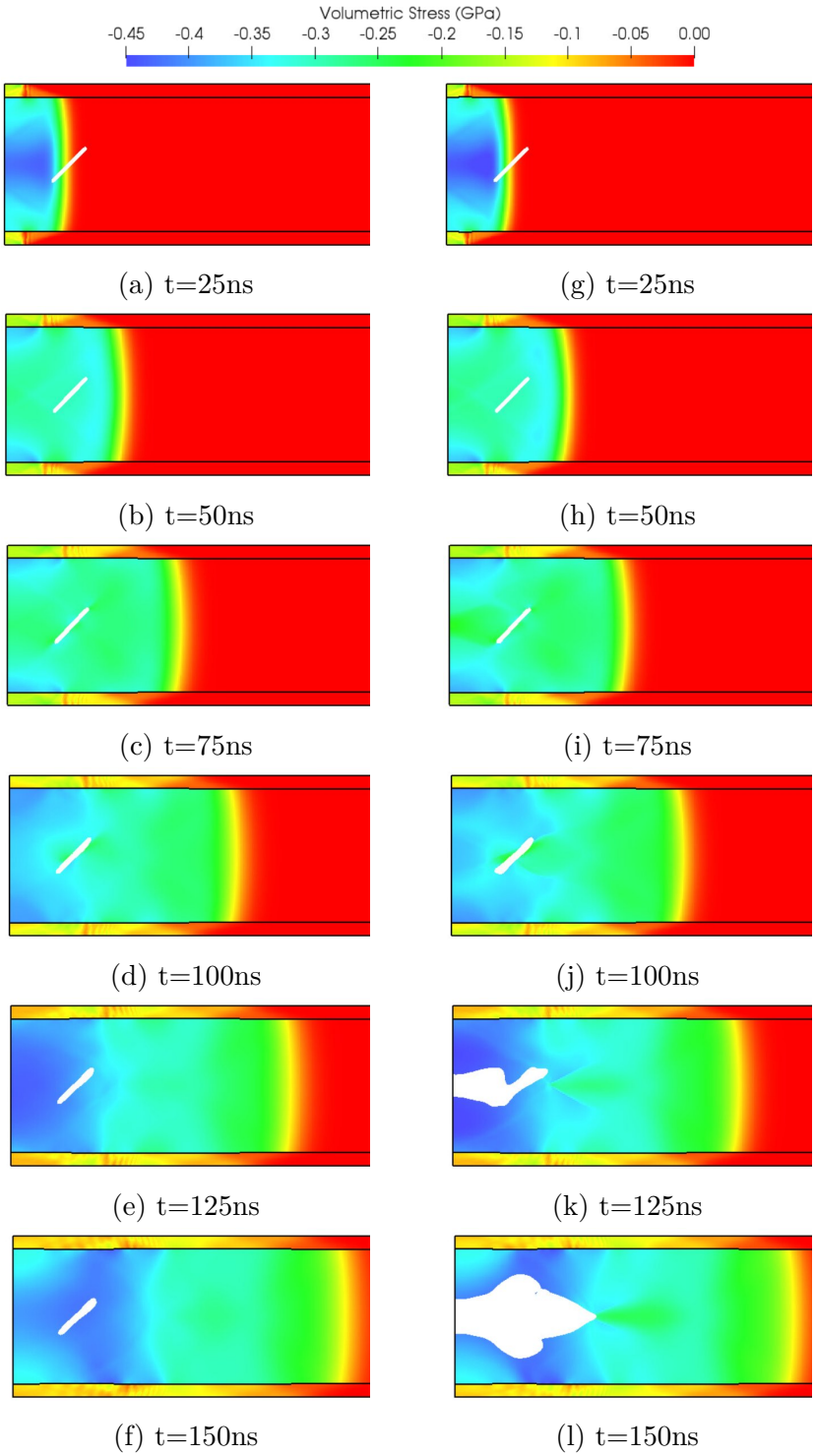

Figure 4.5. Volumetric stress in HMX-Sylgard under impact at 100 m/s, (a-f) without equation of state, and (g-l) with equation of state

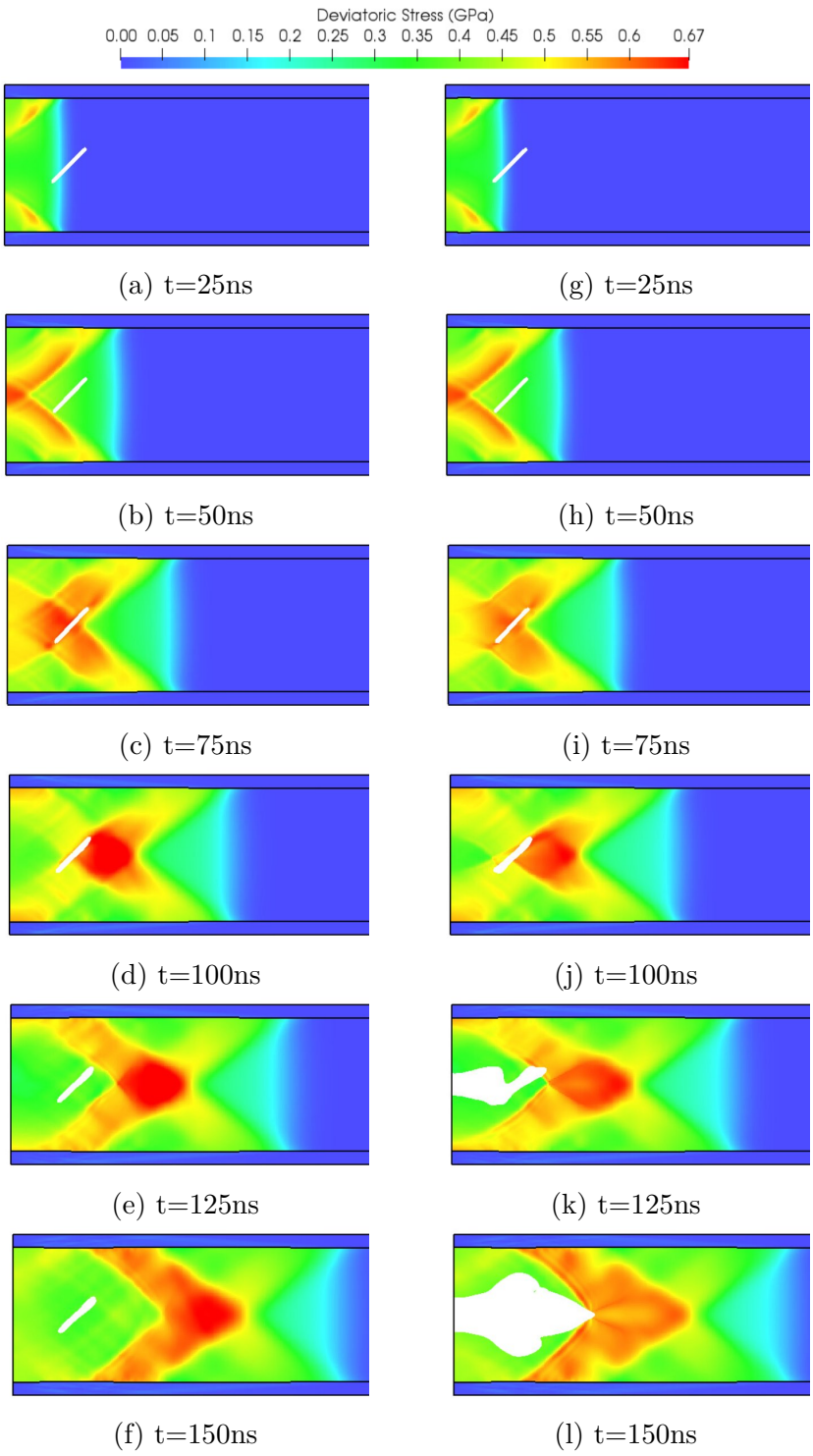

Figure 4.6. Deviatoric stress in HMX-Sylgard under impact at 100 m/s, (a-f) without equation of state, and (g-l) with equation of state

this case, the value of $\beta = 10$ is used and, the results show that this value is not enough to show crack propagation along weak cleavage plane. New simulations with $\beta = 0$ are needed for complete comparison.

The crack propagation begins around 100 ns when the equation of state is considered while crack propagation takes place around 300 ns without the equation of state. Figure 4.7 shows the volumetric stress while figure 4.8 shows the deviatoric stress in the HMX-Sylgard domain at an impact velocity of 100 m/s when the equation of state is not considered. The white region denotes phase field value, $c > 0.9$. The crack propagation starts earlier in time

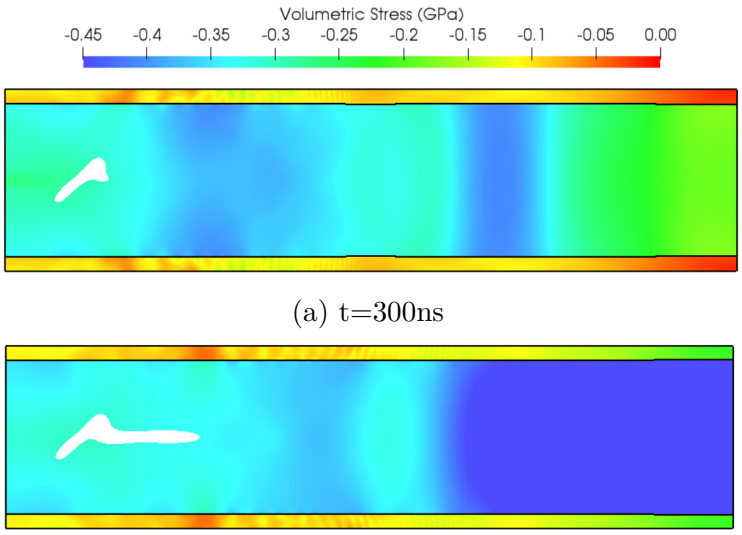

(a) t=300ns

(b) t=400ns

Figure 4.7. Volumetric stress in HMX-Sylgard under impact velocity of 100 m/s without equation of state

with the equation of state as seen in figures 4.5 and 4.6. Also, a wider crack is produced with equation of state.

The positive part of strain energy density contributes to the damage as given in Equation 2.11. With consideration of equation of state the positive part of strain energy density is calculated using the Equation 4.38. In this case, due to compression loading, only the positive projection of coupling stress would contribute to damage. The coupling stress is calculated by removing linear volumetric component of total stress as given in equation 4.35. The coupling stress is equivalent to deviatoric stress in case of isotropic material and can be

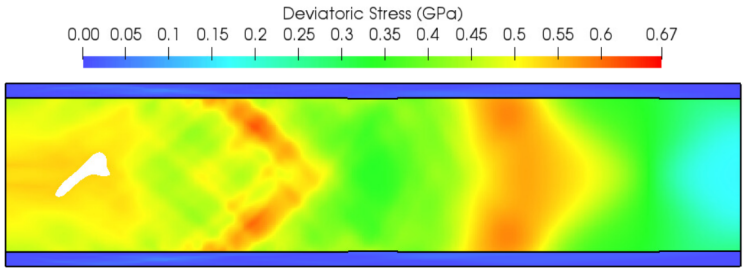

(a) t=300ns

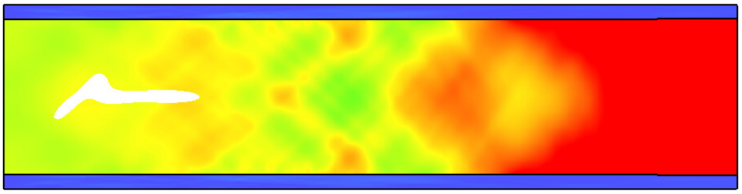

(b) t=400ns

Figure 4.8. Deviatoric stress in HMX-Sylgard under impact velocity of 100 m/s without equation of state

considered equivalent for the analysis. The deviatoric stress in HMX is as high as 0.62 GPa with the equation of state while it is as high as 0.67 GPa without the equation of state. In the compression state, in case of negative values of components of coupling stress, the lower magnitude of individual components of the coupling stress is expected to produce lower value of deviatoric stress. Lower the magnitude of individual negative components of the coupling stress, it can be expected to have more number of positive eigenvalues in the decomposition and thus, more number of non-zero components in the positive projection matrix of coupling stress. Thus, using Equation 4.38 would give more contribution to damage. A complete quantitative analysis is difficult for the given complex stress state and further investigation is needed.

From figure 4.5, it can be seen that the pressure is higher in HMX when the equation of state is considered. The pressure in HMX reaches as high as 0.4 GPa without equation of state but it reaches up to 0.45 GPa with equation of state. Thus, the HMX with equation of state would expand more in vertical direction and displace the HMX-Sylgard interface more than HMX without equation of state. Thus, this behavior is expected to render higher positive strain in vertical direction and, consequently, higher positive part of strain energy

density. Due to involvement of forth order tensors, it is difficult to quantitatively compare the individual energy contributions and further quantitative investigation is needed.

The pressure calculation without considering equation of state comes from the bulk elastic response of material which is given by $p = K_0\eta$ where K_0 is the bulk modulus while η is the volumetric strain. When compared with Equation 4.31, the first term in pressure calculation from equation of state non-linearly depends on η as well as slope of $U_s - U_p$ curve and sound speed. The pressure also depends on the temperature as given by second term in Equation 4.31. Figure 4.9 shows the comparison between pressure with and without consideration of equation of state. Pressure is calculated in a HMX block of 2 nm loaded with 100 m/s in

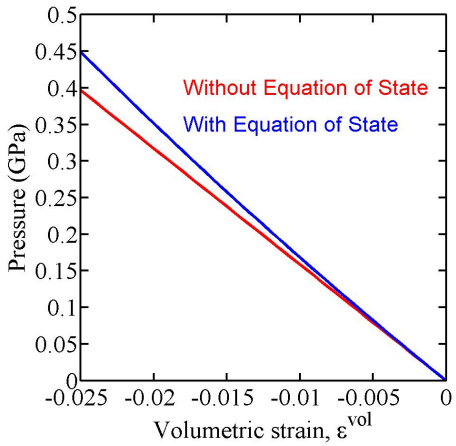

Figure 4.9. Comparison of pressure with and without equation of state in an HMX block under impact of 100 m/s

X-direction while the strain in Y and Z direction is constrained to zero.

The temperature rise in the HMX slab after 400 ns is shown in figure 4.10. This temper-

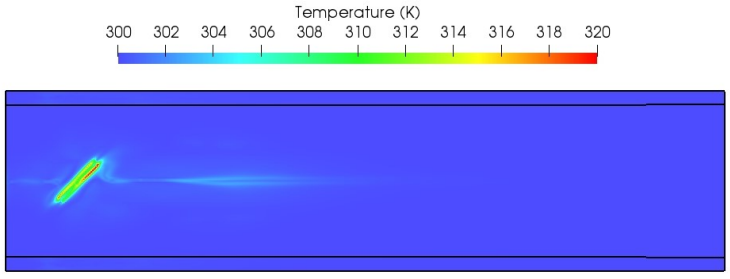

Figure 4.10. Temperature rise in the HMX slab under impact of 100 m/s

ature rise is contributed by only frictional heating at crack.

Heating due to shock and molecular jetting

When considering the equation of state, the temperature rise due to shock needs to be considered. The temperature rise due to shock is incorporated using the term $\Delta T = \beta_v \boldsymbol{\sigma}_v : \boldsymbol{\varepsilon}_v + \rho T \frac{\partial^2 \Psi}{\partial T \partial \varepsilon} : \dot{\boldsymbol{\varepsilon}}$ [84]. Here, $\beta_v = 0.4$ is the proportion of viscous dissipation converted into heat energy. The MD simulations have shown molecular jetting inside a crack in HMX under impact at velocities between 0.5 to 2.5 km/s. The jet of molecules impacting opposite crack surface contributes to the temperature rise as well [85]. The effect of shock is incorporated in the heat generation equation but the effect of molecular jetting is difficult to consider in continuum mechanics simulations with phase field crack. To understand the effect of molecular jetting and possible incorporation of additional heat generation term, a domain equivalent to MD simulations is chosen, as shown in figure 4.11.

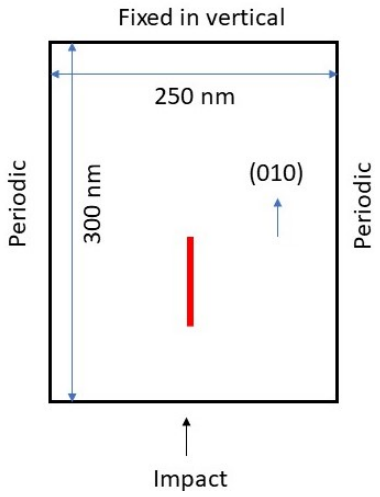

Figure 4.11. HMX block for high velocity impact

The MD results are available for a crack with normal in (100) at five impact velocities, 0.5, 1, 1.5, 2 and 2.5 km/s. The results are also available at impact velocity of 2 km/s for crack orientations (010) and $(\bar{1}10)$. The initial crack with normal in (100) direction is shown in figure 4.11 with a red vertical line. In the preliminary simulations, the domain shown in figure 4.11 is impacted with velocities from 0.5 to 2.5 km/s. The contours of pressure and

temperature rise in the domain at t=20ps are shown in figure 4.12. The temperature and

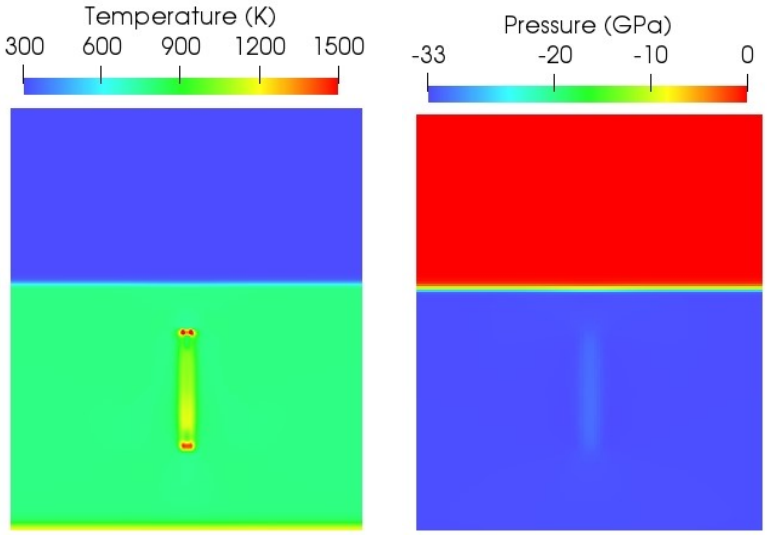

(a) Temperature (b) Pressure

Figure 4.12. Temperature and pressure in HMX under impact at 2.5 km/s at t=20ps

pressure along a line from bottom boundary to top boundary is shown in figure 4.13. The

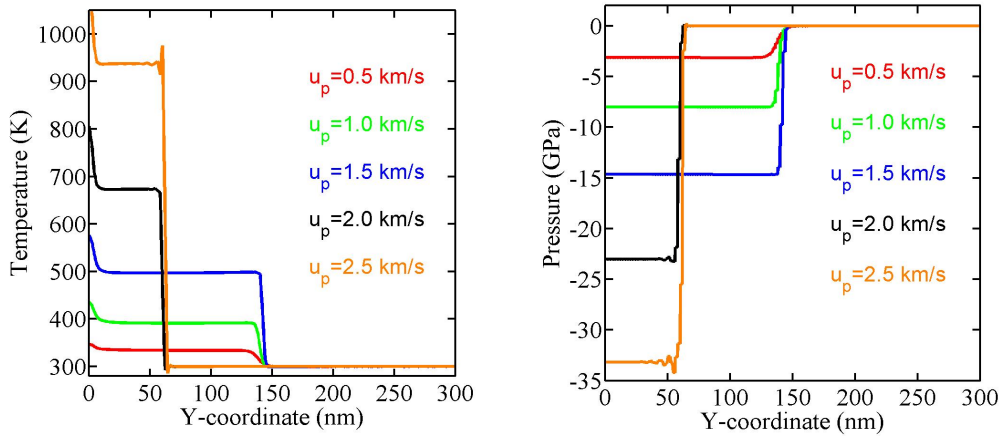

(a) Temperature profile (b) Pressure profile

Figure 4.13. Temperature and pressure in HMX under shock impact along vertical direction

temperature and pressure profile is shown when the wave in the system reaches the top of the crack. The jump in the temperature and pressure across the shock observed in simulations

differs by approximately 10% from the results of molecular dynamic simulations [85] which is shown in figure 4.14.

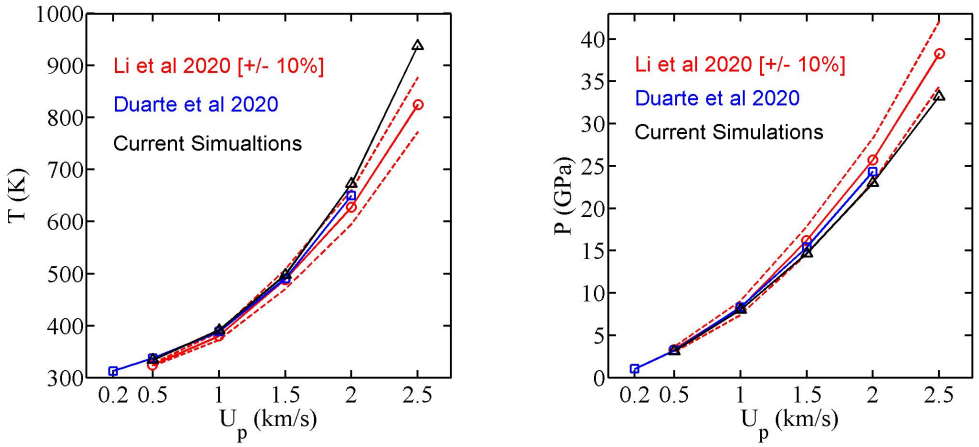

(a) Temperature jump across shock (b) Pressure jump across shock

Figure 4.14. Comparison of jump in temperature and pressure across shock with molecular dynamic simulations

The maximum temperature rise is found at the top crack tip and the time variation is shown in figure 4.15. The highest temperature temperature found in finite element simula-

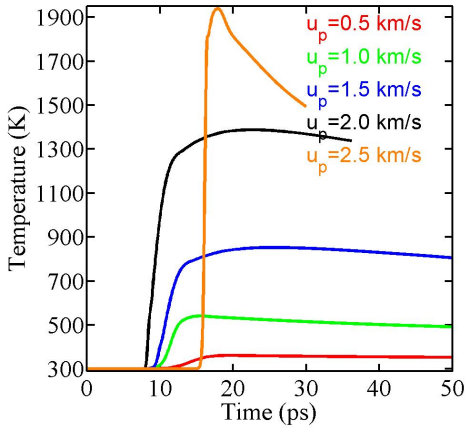

Figure 4.15. Time evolution of temperature in the domain where highest temperature is located

tions is compared with the same from molecular dynamic simulations and the comparison is shown in figure 4.16. The highest temperature from the finite element simulations is observed

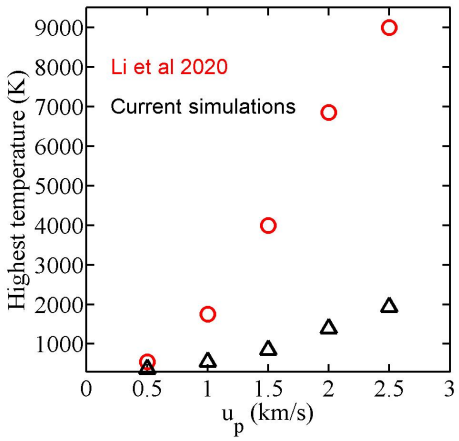

Figure 4.16. Comparison of highest temperature in FE and MD simulations

to be approximately 190 K lesser as compared to MD simulations at an impact velocity of 0.5 km/s while the it is approximately 7060 K lesser than MD simulations at an impact velocity of 2.5 km/s. This is a limitation of the phase field damage model in a continuum finite element framework. Heating source due to molecular jetting could be considered as a term that depends on the impact velocity.

4.4 Conclusions

The anisotropic nature of energetic materials adds to the complexity of the crack propagation. The cleavage planes exist due to weak bonds between atoms in the crystal lattice. Crack propagation is preferred along the weakest cleavage plane. Thus, a penalty is introduced on the cleavage planes other than the weakest. The penalty parameter is an artificially introduced in the formulation and is, thus, variable, depending on the material and domain.

The pressure in the domain non-linearly depends on the temperature and this effect is captured by using Mie-Gruneisen equation of state. At low impact velocities, the effect of equation of state is negligible. However, at high impact velocities, it has to be considered. Mie-Gruneisen equation of state is implemented in small strain formulation and is coupled with anisotropic damage model. Simulations of HMX under impact velocity of 100 m/s suggests that the equation of state could have large impact on the shape and direction of crack propagation. The temperature rise due to friction at crack surfaces is found to be

underestimated in FE simulations as compared to MD simulations which show heating due to impact of molecular jet inside cracks. The temperature rise due to shock is implemented. The temperature rise due to molecular jetting could be implemented using a term that depends on the impact velocity.

5. Summary

The hot-spot formation in PBX microstructure is investigated considering dynamic crack propagation and corresponding frictional heat generation in order to assess safety of PBXs while manufacturing, handling or transport when PBXs can be subjected to low velocity impacts or vibrations. The only heating mechanism considered in this research is the friction at crack surfaces. The focus of this research is on HMX as energetic material and Sylgard or HTPB as polymeric binder. Analysing microstructure behavior can be very complex and, thus, simplified system of EM particle embedded in polymeric binder is analyzed in some cases.

The response of single HMX particle inside HTPB and Sylgard binders is studied with simulations, and compared with experiments. The effect of the mechanical properties of the binder, the adhesive properties of interface, and the surface quality of the EM particle is considered on fracture and temperature rise. The results show that the HMX particles inside Sylgard are more likely to damage than HTPB. A qualitative comparison of the crack patterns and surface debonding in tension and compression indicates that the surface energy of the HTPB-HMX interface may be $G_c^{\mathrm{i}} \geq 30$ J/m^2. While the tensile simulations show debonding and crack growth in the interior of the particle, compression simulations show extensive damage in the particle and limited amount of debonding. Comparison of the simulations with the experiments suggests $G_c^{\mathrm{i}} \leq 10$ J/m^2 for HMX-Sylgard interface. Initial cracks intersecting the particle/binder interface are likely to propagate as compared to the cracks in the interior. Quantitative results suggests that binders with lower stiffness are less sensitive to crack propagation under non-shock conditions.

The effect of particle-particle distance, relative location and size is investigated in a representative PBX microstructure under of a periodic excitation with 210.5 kHz frequency and 4μm amplitude. Larger particles in the microstructure are found to be damaged earlier. Maximum local temperature increase of 21 K after 27.5 μs is found over an area with radius 8 μm is observed. Further investigation is done on a simplified system of two HMX particles inside Sygard binder in an expectation to get better understanding. The two particles are considered in two configurations: (i) shielded where the large particle shields the smaller

particle, and (ii) parallel where the two particles in parallel position to the incident wave. The shielded configuration shows no damage in the small particle for any initial damage while the parallel configuration shows completely damaged smaller particle with an initial interfacial crack. Thus, the shielded configuration shows negligible temperature rise compared to the parallel configuration. The large particles show interfacial cracks growing in the interior and debonding starts near the loading boundary which later propagates to the sides. Heating rate as high as 15×10^3 K/s is observed in the large particle and 33.75×10^3 K/s in the small particle which are in the same order of magnitude as experiments. This work supports experimentally obtained results that friction at cracks and delamination sites are important sources of heating in these composite materials. Furthermore, delamination is also found to contribute to an increase in compressive stress at neighboring particles supplying a gain in the fictional heating source. This suggest that binder adhesion is key to mitigate heating in PBXs under periodical excitation.

Anisotropic material properties of constituent materials show effect on the damage evolution and corresponding frictional heating in the material. When impact velocities increase, effect of temperature dependence on pressure needs to be taken into account. Model with anisotropic fracture and Mie-Gruneisen equation of state in small strain formulation is used to simulate HMX under impact velocity of 100 m/s. Simulations of HMX slab sandwiched between Sylgard layers showed considerable difference in the damage behavior with and without equation of state. The simulations suggests that the equation of state could affect the crack propagation time and the width of the crack. Temperature rise due to shock is implemented and is in accordance with MD results. The effect of molecular jetting is difficult to capture in continuum simulations and could be incorporated by using a term depending on impact velocity.

REFERENCES

[1] J. Akhavan, *The Chemistry of Explosives*. The Royal Society of Chemistry, 2004.

[2] B. Asay, *Shock wave science and technology reference library. Volume 5, Non-shock initiation of explosives*, ser. Shock wave science and technology reference library ; v. 5. Heidelberg ; New York: Springer, 2010.

[3] J. Field, G. Swallowe, and S. Heavens, "Ignition mechanisms of explosives during mechanical deformation," *Proceedings of the Royal Society A*, vol. 382, no. 1782, pp. 231–244, 1982.

[4] J. Field, N. Bourne, S. Palmer, and S. Walley, "Hot-spot ignition mechanisms for explosives and propellants," *Philosophical Transactions of Royal Society of London A*, vol. 339, pp. 269–283, 1992.

[5] J. Dienes, "Frictional hot-spots and propellant sensitivity," *Materials Research Society Symposia Proceedings*, vol. 24, 1984.

[6] J. Dienes, Q. Zuo, and J. Kershner, "Impact initiation of explosives and propellants via statistical crack mechanics," *Journal of the Mechanics and Physics of Solids*, vol. 54, pp. 1237–1275, 2006.

[7] A. Dandekar, Z. Roberts, S. Paulson, W. Chen, S. Son, and M. Koslowski, "The effect of the particle surface and binder properties on the response of polymer bonded explosives at low impact velocities," *Computational Materials Science*, vol. 166, pp. 170–178, 2019.

[8] R. Austin, N. Barton, J. Reaugh, and L. Fried, "Direct numerical simulation of shear localization and decomposition reactions in shock-loaded HMX crystal," *Journal of Applied Physics*, vol. 117, no. 18, 2015.

[9] P. Rae, S. Palmer, H. Goldrein, J. Field, and A. Lewis, "Quasi-static studies of the deformation and failure of PBX 9501," *Proceedings of the Royal Society of London A: Mathematical, Physical and Engineering Sciences*, vol. 458, no. 2025, pp. 2227–2242, 2002.

[10] P. Rae, H. Goldrein, S. Palmer, J. Field, and A. Lewis, "Quasistatic studies of the deformation and failure of β-HMX based polymer bonded explosives," *Proceedings of the Royal Society A: Mathematical, Physical and Engineering Sciences*, vol. 458, pp. 743–762, 2002.

[11] N. Parab, Z. Roberts, M. Harr, J. Mares, A. Casey, I. Gunduz, M. Hudspeth, B. Claus, T. Sun, K. Fezzaa, S. Son, and W. Chen, "High speed X-ray phase contrast imaging of energetic composites under dynamic compression," *Applied Physics Letters*, vol. 109, no. 13, 2016.

[12] M. Harr, "Visualization and mechanical response of damage mechanisms in HMX based energetic composites," Master's thesis, Purdue University, 2017.

[13] H. Arora, E. Tarleton, J. Mayer, M. Charalmbides, and D. Lewis, "Modelling the damage and deformation process in a plastic bonded explosive microstructure under tension using the finite element method," *Computational Materials Science*, vol. 110, pp. 91–101, 2015.

[14] R. Gee, A. Maiti, S. Bastea, and L. Fried, "Molecular Dynamics Investigation of Adhesion between TATB Surfaces and Amorphous Fluoropolymers," *Macromolecules*, vol. 40, no. 9, pp. 3422–3428, 2007.

[15] H. Tan, C. Liu, Y. Huang, and P. Geubelle, "The cohesive law for the particle/matrix interfaces in high explosives," *Journal of the Mechanics and Physics of Solids*, vol. 53, no. 8, pp. 1892–1917, 2005.

[16] D. Walters, D. Luscher, J. Yeager, and B. Patterson, "Cohesive finite element modeling of the delamination of HTPB binder and HMX crystals under tensile loading," *International Journal of Mechanical Sciences*, vol. 140, pp. 151–162, 2018.

[17] C. Liu, J. Yeager, and K. Ramos, "Bonding energy of sylgard on fused quartz: An experimental investigation," eng, *Philosophical Magazine*, vol. 28, no. 1, pp. 1–21, 2015.

[18] A. Gent and B. Park, "Failure processes in elastomers at or near a rigid spherical inclusion," *Journal of Materials Science*, vol. 19, no. 6, pp. 1947–1956, 1984.

[19] B. Tanasoiu, J. Palsdottir, N. Parab, M. Harr, Z. Roberts, J. Mares, E. Gunduz, T. Sun, K. Fezzaa, S. Son, W. Chen, and M. Koslowski, "Adhesive energy between sylgard and inclusions: Experiments and model calibration," in *Proceedings of the American Society for Composites: Thirty-Second Technical Conference*, Purdue University, West Lafayette, Indiana, Oct. 2017.

[20] B. Tanasoiu and M. Koslowski, "A parametric study of the dynamic failure of energetic composites," *Journal of Applied Physics*, vol. 122, no. 12, 2017.

[21] A. Barua, Y. Horie, and M. Zhou, "Energy localization in HMX-Estane polymer-bonded explosives during impact loading," *Journal of Applied Physics*, vol. 111, 2012.

[22] N. Grilli, C. Duarte, and M. Koslowski, "Dynamic fracture and hot-spot modeling in energetic composites," *Journal of Applied Physics*, vol. 123, no. 6, 2018.

[23] G. Francfort and J. Marigo, "Revisiting brittle fracture as an energy minimization problem," *Journal of Mechanics and Physics of Solids*, vol. 46, no. 8, pp. 1319–1342, 1998.

[24] A. Griffith, "The phenomena of rupture and flow in solids," *Philosophical Transactions of the Royal Society of London A: Mathematical, Physical and Engineering Sciences*, vol. 221, no. 582-593, pp. 163–198, 1921.

[25] S. Palmer and J. Field, "The deformation and fracture of β-HMX," *Proceedings of the Royal Society A*, vol. 383, no. 1785, pp. 399–407, 1982.

[26] H. Gallagher, J. Miller, D. Sheen, J. Sherwood, and R. Vrcelj, "Mechanical properties of β-HMX," *Chemistry Central Journal*, vol. 9, no. 1, pp. 1–15, 2015.

[27] E. Jaramillo, T. Sewell, and A. Strachan, "Atomic-level view of inelastic deformation in a shock loaded molecular crystal," *Physical Review B*, vol. 76, no. 6, 2007.

[28] M. Cawkwell, K. Ramos, D. Hooks, and T. Sewell, "Homogeneous dislocation nucleation in cyclotrimethylene trinitramine under shock loading," *Journal of Applied Physics*, vol. 107, no. 6, 2010.

[29] T. Zhou, S. Zybin, Y. Liu, F. Huang, and W. Goddard, "Anisotropic shock sensitivity for β-octahydro-1,3,5,7-tetranitro-1,3,5,7-tetrazocine energetic material under compressive-shear loading from reaxFF-lg reactive dynamics simulations," *Journal of Applied Physics*, vol. 111, no. 12, 2012.

[30] H. Amor, J. Marigo, and C. Maurini, "Regularized formulation of the variational brittle fracture with unilateral contact: Numerical experiments," *Journal of the Mechanics and Physics of Solids*, vol. 57, no. 8, pp. 1209–1229, 2009.

[31] M. Borden, C. Verhoosel, M. Scott, T. Hughes, and C. Landis, "A phase-field description of dynamic brittle fracture," *Computer Methods in Applied Mechanics and Engineering*, vol. 217-220, pp. 77–95, 2012.

[32] C. Miehe, F. Welschinger, and M. Hofacker, "Thermodynamically consistent phase-field models of fracture: Variational principles and multi-field FE implementations," *International Journal for Numerical Methods in Engineering*, vol. 83, pp. 1273–1311, 2010.

[33] P. Chakraborty, Y. Zhang, and M. Tonks, "Multi-scale modeling of microstructure dependent intergranular brittle fracture using a quantitative phase-field based method," *Computational Materials Science*, vol. 113, pp. 38–52, 2016.

[34] Y. Xie, O. Kravchenko, R. Pipes, and M. Koslowski, "Phase field modeling of damage in glassy polymers," *Journal of the Mechanics and Physics of Solids*, vol. 93, pp. 182–197, 2016.

[35] C. Miehe, L. Schanzel, and H. Ulmer, "Phase field modeling of fracture in multi-physics problems. Part I. Balance of crack surface and failure criteria for brittle crack propagation in thermo-elastic solids," *Computer methods in applied mechanics and engineering*, vol. 294, pp. 449–485, 2015.

[36] M. Website, *Multiphysics Object Oriented Simulation Environment framework*, https://mooseframework.org/, Idaho National Lab, 2018.

[37] N. Grilli and M. Koslowski, "The effect of crystal orientation on shock loading of single crystal energetic materials," *Computational Materials Science*, vol. 155, pp. 235–245, 2018.

[38] J. Vial, D. Picart, P. Bailly, and F. Delvare, "Numerical and experimental study of the plasticity of HMX during a reverse edge-on impact test," *Modelling and Simulation in Materials Science and Engineering*, vol. 21, no. 4, 2013.

[39] C. Duarte, N. Grilli, and M. Koslowski, "Effect of initial damage variability on hot-spot nucleation in energetic materials," *Journal of Applied Physics*, vol. 124, no. 2, 2018.

[40] G. Camacho and M. Ortiz, "Computational modelling of impact damage in brittle materials," *International Journal of Solids and Structures*, vol. 33, no. 20-22, pp. 2899–2938, 1996.

[41] A. Atkins, C. Lee, and R. Caddell, "Time-temperature dependent fracture toughness of PMMA," *Journal of Materials Science*, vol. 10, pp. 1381–1393, 1975.

[42] C. Zimmermann, W. Klemm, and K. Schonert, "Dynamic energy release rate and fracture heat in polymethylmethacrylate (PMMA) and a high-strength steel," *Engineering Fracture Mechanics*, vol. 20, no. 5-6, pp. 777–782, 1984.

[43] B. Banerjee and D. Adams, "Micromechanics-based prediction of thermoelastic properties of high energy materials," 2012.

[44] O. Johnson, "HMX as a military explosive," US Naval Ordnance Laboratory, Tech. Rep., 1956.

[45] Y. Long, Y. Liu, F. Nie, and J. Chen, "A method to calculate the thermal conductivity of HMX under high pressure," *Philosophical Magazine*, vol. 92, no. 8, pp. 1023–1045, 2012.

[46] L. Koshigoe, R. Shoemaker, and R. Taylor, "Specific heat of HMX," *AIAA Journal*, vol. 22, no. 11, pp. 1600–1601, 1984.

[47] I. Johnston, D. McCluskey, C. Tan, and M. Tracey, "Mechanical characterization of bulk sylgard 184 for microfluidics and microengineering," *Journal of Micromechanics and Microengineering*, vol. 24, 2014.

[48] F. Reinert and W. Luthy, "Thermo-optically driven adaptive mirror based on thermal expansion: Preparation and resolution," *Optics Express*, vol. 13, no. 26, 2005.

[49] H. Kugler, R. Stacer, and C. Steimle, "Direct Measurement of Poisson's Ratio in Elastomers," *Rubber Chemistry and Technology*, vol. 63, no. 4, pp. 473–487, 1990.

[50] M. Kohga, "Dynamic mechanical properties of hydroxyl-terminated polybutadiene containing polytetrahydrofuran as a plasticizer," *Journal of the Society of Rheology, Japan*, vol. 40, no. 4, pp. 185–193, 2012.

[51] R. Thomas, A. Boudenne, L. Ibos, Y. Candau, and S. Thomas, "Thermophysical properties of CTBN and HTPB liquid rubber modified epoxy blends," *Journal of Applied Polymer Science*, vol. 116, pp. 3232–3241, 2010.

[52] F. Chaves and J. Gois, "Research on the specific heat capacity of PBX formulations based on RDX," *Journal of Aerospace Technology and Management*, vol. 8, no. 3, pp. 352–356, 2016.

[53] T. D. C. Company, *Technical data sheet: Sylgard 184 silicone elastomer*, 2017.

[54] J. Mares, J. Miller, N. Sharp, D. Moore, D. Adams, L. Groven, J. Rhoads, and S. Son, "Thermal and mechanical response of PBX 9501 under contact excitation," *Journal of Applied Physics*, vol. 113, no. 8, 2013.

[55] M. Chen, S. You, K. Suslick, and D. Dlott, "Hot spots in energetic materials generated by infrared and ultrasound, detected by thermal imaging microscopy," *Review of Scientific Instruments*, vol. 85, no. 2, 2014.

[56] S. You, M. Chen, D. Dlott, and K. Suslick, "Ultrasonic hammer produces hot spots in solids," *Nature Communications*, vol. 6, 2015.

[57] C. Duarte, R. Kohler, and M. Koslowski, "Dynamic fracture and frictional heating due to periodic excitation in energetic materials," *Journal of Applied Physics*, vol. 124, no. 16, 2018.

[58] Z. Roberts, A. Casey, I. Gunduz, J. Rhoads, and S. Son, "The effects of crystal proximity and crystal-binder adhesion on the thermal responses of ultrasonically-excited composite energetic materials," *Journal of Applied Physics*, vol. 122, no. 24, 2017.

[59] Z. Roberts, J. Wickham, C. Sorensen, T. Manship, I. Gunduz, S. Son, and J. Rhoads, "Mesoscale observations of the thermal decomposition of energetic composites under ultrasonic excitation," *Journal of Applied Physics*, vol. 125, no. 21, 2019.

[60] H. Czerski, M. Greenaway, W. Proud, and J. Field, "β-δ phase transition during drop-weight impact on cyclotetramethylene-tetranitroamine," *Journal of Applied Physics*, vol. 96, no. 8, pp. 4131–4134, 2004.

[61] J. Kimura and N. Kubota, "Thermal decomposition process of hmx," *Propellants, Explosives, Pyrotechnics*, vol. 5, no. 1, pp. 1–8, 1980.

[62] N. Newmark, "A method of computation for structural dynamics," *Journal of the Engineering Mechanics Division*, 1959.

[63] D. Williamson, C. Siviour, W. Proud, S. Palmer, R. Govier, K. Ellis, P. Blackwell, and C. Leppard, "Temperaturetime response of a polymer bonded explosive in compression (EDC37)," *Journal of Physics D: Applied Physics*, vol. 41, no. 8, 2008.

[64] G. Parker, E. Heatwole, M. Holmes, B. Asay, P. Dickson, and J. McAfee, "Deflagration-to-detonation transition in hot hmx and hmx-based polymer-bonded explosives," eng, *Combustion and flame*, vol. 215, no. C, pp. 295–308, 2020, ISSN: 0010-2180.

[65] K. Graff, *Wave Motion in Elastic Solids*, eng, ser. Dover Books on Physics. Newburyport: Dover Publications, 2012, ISBN: 0-486-66745-6.

[66] J. Summerscales, *Microstructural Characterisation of Fibre-Reinforced Composites*, eng, ser. Woodhead Publishing Series in Composites Science and Engineering. Burlington: Elsevier Science, 1998, ISBN: 1-85573-240-8.

[67] *Dynamic Methods for Damage Detection in Structures*, eng, 1st ed. 2008., ser. CISM International Centre for Mechanical Sciences, Courses and Lectures. 2008, ISBN: 3-211-78776-3.

[68] X. Wang, "The study on longitudinal wave and transverse wave propagation behavior in frp composite material," eng, in *Proceedings of 2011 International Conference on Electronic and Mechanical Engineering and Information Technology*, vol. 9, IEEE, 2011, pp. 4455–4458, ISBN: 9781612840871.

[69] R. Lakes, *Viscoelastic materials*, eng. Cambridge ; New York: Cambridge University Press, 2009, ISBN: 1-107-45978-8.

[70] E. Madsen, G. Frank, M. Hobson, S. Lin-Gibson, T. Hall, J. Jiang, and T. Stiles, "Instrument for determining the complex shear modulus of soft-tissue-like materials from 10 to 300 hz," *Physics in Medicine and Biology*, vol. 53, no. 19, pp. 5313–5342, Aug. 2008. DOI: 10.1088/0031-9155/53/19/004. [Online]. Available: https://doi.org/10.1088%5C%2F0031-9155%5C%2F53%5C%2F19%5C%2F004.

[71] A. Barua and M. Zhou, "A Lagrangian framework for analyzing microstructural level response of polymer-bonded explosives," *Modelling and Simulation in Materials Science and Engineering*, vol. 19, 2011.

[72] J. M. Zaug, R. A. Austin, M. R. Armstrong, J. C. Crowhurst, N. Goldman, L. Ferranti, C. K. Saw, R. A. Swan, R. Gross, and L. E. Fried, "Ultrafast dynamic response of single-crystal β-HMX (octahydro-1,3,5,7-tetranitro-1,3,5,7-tetrazocine)," *Journal of Applied Physics*, vol. 123, no. 20, 2018. DOI: 10.1063/1.5029923.

[73] N. Grilli and M. Koslowski, "The effect of crystal anisotropy and plastic response on the dynamic fracture of energetic materials," eng, *Journal of applied physics*, vol. 126, no. 15, p. 155 101, 2019, ISSN: 1089-7550.

[74] J. Clayton and J. Knap, "Phase field modeling of directional fracture in anisotropic polycrystals," eng, *Computational materials science*, vol. 98, pp. 158–169, 2015, ISSN: 0927-0256.

[75] T. T. Nguyen, J. Réthoré, and M.-C. Baietto, "Phase field modelling of anisotropic crack propagation," eng, *European journal of mechanics, A, Solids*, vol. 65, pp. 279–288, 2017, ISSN: 0997-7538.

[76] C. Miehe and M. Lambrecht, "Algorithms for computation of stresses and elasticity moduli in terms of seth-hill's family of generalized strain tensors," eng, *Communications in numerical methods in engineering*, vol. 17, no. 5, pp. 337–353, 2001, ISSN: 1069-8299.

[77] M. L. Wilkins, *Computer Simulation of Dynamic Phenomena*, eng, ser. Scientific Computation. Berlin/Heidelberg: Springer Berlin Heidelberg, 1999, ISBN: 9783642083150.

[78] L. Maheo, G. Rio, and V. Grolleau, "On the use of some numerical damping methods of spurious oscillations in the case of elastic wave propagation," eng, *Mechanics research communications*, vol. 38, no. 2, pp. 81–88, 2011, ISSN: 0093-6413.

[79] B. Craig, "Data from shock initiation experiments," Technical Report, Tech. Rep., 1974.

[80] S. P. Marsh, "LASL Shock Hugoniot Data," University of California Press, Tech. Rep., 1980.

[81] B. Olinger, B. Roof, and H. H. Cady, "The linear and volume compression of β-HMX and RDX," 1978.

[82] C.-S. Yoo and H. Cynn, "Equation of state, phase transition, decomposition of β-HMX (octahydro-1,3,5,7-tetranitro-1,3,5,7-tetrazocine) at high pressures," *The Journal of Chemical Physics*, vol. 111, no. 22, pp. 10 229–10 235, 1999. DOI: 10.1063/1.480341. [Online]. Available: https://doi.org/10.1063/1.480341.

[83] R. Menikoff and T. Sewell, "Constituent properties of HMX needed for mesoscale simulations," *Combustion Theory and Modelling*, vol. 6, pp. 103–125, 2002.

[84] C. Duarte, C. Li, B. Hamilton, A. Strachan, and K. M, "Continuum and molecular dynamics simulations of pore collapse in shocked β-hmx single crystals," *Journal of Applied Physics, under review*, 2020.

[85] C. Li, B. W. Hamilton, and A. Strachan, "Hotspot formation due to shock-induced pore collapse in 1,3,5,7-tetranitro-1,3,5,7-tetrazoctane (HMX): Role of pore shape and shock strength in collapse mechanism and temperature," *Journal of Applied Physics*, vol. 127, no. 17, 2020, ISSN: 0021-8979.

A. ACINTERFACECLEAVAGEFRACTURE

Header file: ACInterfaceCleavageFracture.h

```
/// Considers cleavage plane anisotropy in the crack propagation
#pragma once
#include "ACInterface.h"

class ACInterfaceCleavageFracture : public ACInterface
{
public:
  static InputParameters validParams();

  ACInterfaceCleavageFracture(const InputParameters & parameters);

protected:
  virtual Real computeQpResidual();
  virtual Real computeQpJacobian();

  /// term with beta penalty
  Real betaNablaPsi();

  /// penalty for damage on planes not normal to the weak
  /// (favoured) cleavage plane (Clayton & Knap, 2015)
  const Real _beta_penalty;

  /// Plane normal to the weak cleavage plane:
  /// M in (Clayton & Knap, 2015)
  const RealVectorValue _cleavage_plane_normal;
};
```

Code file: ACInterfaceCleavageFracture.C

```
/// Considers cleavage plane anisotropy in the crack propagation
#include "ACInterfaceCleavageFracture.h"
registerMooseObject("PhaseFieldApp", ACInterfaceCleavageFracture);

InputParameters
ACInterfaceCleavageFracture::validParams()
{
  InputParameters params = ACInterface::validParams();
  params.addClassDescription("Gradient energy Allen-Cahn Kernel where "
        crack propagation along weak cleavage plane is preferred");
  params.addRequiredParam<Real>("beta_penalty", "penalty to penalize "
        "fracture on planes not normal to one cleavage plane normal "
```

```
        "which is normal to weak cleavage plane. Setting beta=0 "
        "results in isotropic damage.");
  params.addRequiredParam<RealVectorValue>("cleavage_plane_normal",
        "Normal to the weak cleavage plane");
  return params;
}

ACInterfaceCleavageFracture::ACInterfaceCleavageFracture
(const InputParameters & parameters)
  : ACInterface(parameters),
    _beta_penalty(getParam<Real>("beta_penalty")),
    _cleavage_plane_normal(getParam<RealVectorValue>
        ("cleavage_plane_normal"))
{
}

Real
ACInterfaceCleavageFracture::betaNablaPsi()
{
  return _beta_penalty * _L[_qp] * _kappa[_qp] * (_grad_u[_qp] *
    _cleavage_plane_normal) * (_grad_test[_i][_qp] *
    _cleavage_plane_normal);
}

Real
ACInterfaceCleavageFracture::computeQpResidual()
{
  return (1 + _beta_penalty) * _grad_u[_qp] * kappaNablaLPsi() -
    betaNablaPsi();
}

Real
ACInterfaceCleavageFracture::computeQpJacobian()
{
  /// dsum is the derivative \f$ \frac\partial{\partial \eta}
  /// \left( \nabla (L\psi) \right) \f$
  RealGradient dsum = (_dkappadop[_qp] * _L[_qp] + _kappa[_qp] *
    _dLdop[_qp]) * _phi[_j][_qp] * _grad_test[_i][_qp];

  /// compute the derivative of the gradient of the mobility
  if (_variable_L)
  {
    RealGradient dgradL = _grad_phi[_j][_qp] * _dLdop[_qp] +
        _grad_u[_qp] * _phi[_j][_qp] * _d2Ldop2[_qp];
```

```
    for (unsigned int i = 0; i < _n_args; ++i)
      dgradL += (*_gradarg[i])[_qp] * _phi[_j][_qp] *
        (*_d2Ldargdop[i])[_qp];

    dsum += (_kappa[_qp] * dgradL + _dkappadop[_qp] *
        _phi[_j][_qp] * gradL()) * _test[_i][_qp];
  }

  return (1 + _beta_penalty) * _grad_phi[_j][_qp] * kappaNablaLPsi() +
    _grad_u[_qp] * dsum - _beta_penalty * _L[_qp] * _kappa[_qp] *
    (_grad_u[_qp] * _cleavage_plane_normal) * (_grad_phi[_j][_qp] *
    _cleavage_plane_normal);
}
```

```
%   Function definition to calculate inner product of matrices
function Splus = innerProduct(P,S)
Splus = zeros(3,3);
for i=1:3
    for j=1:3
        for k=1:3
            for l=1:3
                Splus(i,j) = Splus(i,j) + P(i,j,k,l)*S(k,l);
            end
        end
    end
end
end

%   Function definition to calculate outer product of matrices
function C = outerProduct(A,B)
C = zeros(3,3,3,3);
for i = 1:3
    for j = 1:3
        for k = 1:3
            for l = 1:3
                C(i,j,k,l) = A(i,j) * B(k,l);
            end
        end
    end
end
end

%   Function definition to calculate G tensor
function G = additionG(Ma,Mb)
Gab = zeros(3,3,3,3);
for i = 1:3
    for j = 1:3
        for k = 1:3
            for l = 1:3
                Gab(i,j,k,l) = Ma(i,k)*Mb(j,l) + Ma(i,l)*Mb(j,k);
            end
        end
    end
end
Gba = zeros(3,3,3,3);
for i = 1:3
    for j = 1:3
```

```
        for k = 1:3
            for l = 1:3
                Gba(i,j,k,l) = Mb(i,k)*Ma(j,l) + Mb(i,l)*Ma(j,k);
            end
        end
    end
end
G = Gab + Gba;
end

% Input matrix
S = [-1 0 0; 0 -1 0; 0 0 0];

% Eigen decomposition
[N,D] = eig(S);
s = zeros(3,1);
d = zeros(3,1);
M = cell(3);
for a=1:3
    s(a) = D(a,a);
    if s(a)>0
        d(a) = 1;
    end
    M{a} = N(:,a)*N(:,a)';
end

theta = zeros(3);
for a=1:3
    for b=1:3
        if s(a)~=s(b)
            theta(a,b) = 0.5 * (d(a)*s(a)-d(b)*s(b)) / (s(a)-s(b));
        else
            theta(a,b) = 0.25 * (d(a)+d(b));
        end
    end
end

P = zeros(3,3,3,3);
for a=1:3
    P = P + d(a) * outerProduct(M{a},M{a});
end

for a=1:3
    for b=1:3
```

```
        if b~=a
            G = additionG(M{a},M{b});
            P = P + theta(a,b) * G;
        end
    end
end

Splus = innerProduct(P,S);
```

VITA

Akshay Dandekar received his Bachelor of Technology degree (with Honors) in Aerospace Engineering with minor in Mechanical Engineering from Indian Institute of Technology Bombay in Mumbai, India in August 2014. He joined graduate school at University of Illinois at Urbana-Champaign and graduated with Master of Science degree in Aerospace Engineering in December 2015. After time spent as Methods Engineer in a manufacturing company in aerospace sector, he started PhD in Mechanical Engineering at Purdue University in August 2016 under the guidance of Dr. Marisol Koslowski. His research focuses on understanding hot-spot formation in polymer bonded explosives due to fracture and frictional heating under non-shock stimulus using phase field damage model.